7-7-2020

Numerical investigation of the flow characteristics in a two-pass channel with a sharp 180° turn

Damanpreet Singh
University of Windsor

Recommended Citation

Singh, Damanpreet, "Numerical investigation of the flow characteristics in a two-pass channel with a sharp 180° turn" (2020). *Electronic Theses and Dissertations*. 8397.
https://scholar.uwindsor.ca/etd/8397

Numerical investigation of the flow characteristics in a two-pass channel with a sharp 180° turn

By

Damanpreet Singh

A Thesis
Submitted to the Faculty of Graduate Studies
through the Department of Mechanical, Automotive and Materials Engineering
in Partial Fulfillment of the Requirements for
the Degree of Master of Applied Science
at the University of Windsor

Windsor, Ontario, Canada

2020

Numerical Investigation of the flow characteristics in a two-pass channel with a sharp 180° turn

by

Damanpreet Singh

APPROVED BY:

T. Bolisetti

Department of Civil and Environmental Engineering

R. Barron
Department of Mechanical, Automotive and Materials Engineering

R. Balachandar, Co-Advisor
Department of Civil and Environmental Engineering

V. Roussinova, Co-Advisor
Department of Mechanical, Automotive and Materials Engineering

April 22, 2020

DECLARATION OF ORIGINALITY

I hereby certify that I am the sole author of this thesis and that no part of this thesis has been published or submitted for publication.

I certify that, to the best of my knowledge, my thesis does not infringe upon anyone's copyright nor violate any proprietary rights and that any ideas, techniques, quotations, or any other material from the work of other people included in my thesis, published or otherwise, are fully acknowledged in accordance with the standard referencing practices. Furthermore, to the extent that I have included copyrighted material that surpasses the bounds of fair dealing within the meaning of the Canada Copyright Act, I certify that I have obtained a written permission from the copyright owner(s) to include such material(s) in my thesis and have included copies of such copyright clearances to my appendix.

I declare that this is a true copy of my thesis, including any final revisions, as approved by my thesis committee and the Graduate Studies office, and that this thesis has not been submitted for a higher degree to any other University or Institution.

ABSTRACT

Two-pass flow channels with a square or rectangular cross-section are used in many thermo-fluid systems such as air-conditioners, heat exchangers, cooling passages of gas turbine blades, etc. As the flow passes through these channels, it becomes highly three-dimensional. This complexity is due to the Dean-type secondary motion, flow separation and impingement in the turn. Our approach is to first investigate the turbulent flow in a pressure-driven straight square duct at a high Reynolds number (Re = 40,000) to reach flow conditions which are representative of fully developed turbulence. Numerical simulations are carried out to investigate the nature of the secondary flow in a square duct through velocity and vorticity fields. The results are validated with the DNS study of Pirozzoli *et al.* (2018). Following this validation, another square duct simulation at a higher Reynolds number (Re = 50,000) is carried out as the numerical strategy for the two-pass channel requires a fully developed turbulence inlet condition. This is used as the approach flow condition at the inlet of the two-pass channel. The results of this two-pass channel simulation (Re = 50,000) before the turn, in the turn and after the turn are validated by comparing it with the PIV data of Schabacker *et al.*, (1998b). The influence of the bend clearance on the turbulence parameters of the flow, the three-dimensionality of the flow and the complexity of Dean-type secondary motion, flow separation and flow recirculation is examined. The turbulence structures within the flow are identified using a vortex identification criterion, namely Q-criterion. These structures reveal the complexity of turbulence in the flow field of two-pass channel, mainly the recirculation region. The comparison of Q-criterion with two different bend clearances is carried out to study the influence of the bend clearance on the turbulent structures formed in the two-pass channel.

DEDICATION

This work is dedicated to my mother.

I couldn't be where I am today without you.

ACKNOWLEDGEMENTS

First and foremost, I would like to thank my advisors, Dr. Ram Balachandar and Dr. Vesselina Roussinova, for giving me the opportunity to perform research at Computational Fluid Dynamics Lab and for providing me with continuous guidance and support in my studies and research. I would also like to acknowledge my committee members Dr. Ronald Barron and Dr. Tirupati Bolisetti for their advice on my research.

This research is made possible by the facilities of the Shared Hierarchical Academic Research Computing Network (SHARCNET: www.sharcnet.ca) and Compute Canada.

I would also like to thank Dr. Abishek Sridhar, Subhadip Das, Nimesh Virani and Vivek Joshi for sharing their knowledge with me during my study. I would also like to extend my appreciation for tremendous support of present and past members at the Computational Fluid Dynamics Lab including Maziar Mosavati, Dr. Kohei Fukuda, Shu Chen, Nam Kang, Yuanming Yu, Saikrishna Muppavarapu and Corey Klinkhamer.

A special thanks to all the faculty and staff members of the Department of Mechanical, Automotive and Materials Engineering and the Faculty of Graduate Studies.

TABLE OF CONTENTS

LIST OF TABLES

LIST OF FIGURES

NOMENCLATURE

U, V, W	instantaneous velocities in x, y and z directions respectively
$\bar{U}, \bar{V}, \bar{W}$	mean velocities in x, y and z directions respectively
u', v', w'	fluctuating velocities in x, y and z directions respectively
$p,\ \bar{p},\ p'$	instantaneous, mean and fluctuating pressure
x, y, z	cartesian coordinates
$\overline{u_i'u_j'}$	Reynolds stresses
Re_τ	friction Reynolds number
y^+	dimensionless wall distance
P_{ij}	production tensor
ϕ_{ij}^*	pressure-strain tensor
ε_{ij}	dissipation rate tensor
D_{ij}^t	turbulent diffusion tensor
k	turbulent kinetic energy
P	turbulent kinetic energy production
n_i, n_j, n_k	unit vectors representing the wall-normal direction in i, j and k directions respectively
a_{ij}	anisotropy tensor
S_{ij}	strain rate tensor
W_{ij}	rotation rate tensor
L	turbulent length scale

C	turn clearance
D_h	hydraulic diameter of the square duct and the two-pass channel
h	half -width of the duct
U_b	bulk velocity
$proj$	projected distance in the bend =
	$\frac{\sqrt{x^2+z^2}}{S}\lvert\cos\alpha\rvert$ for $\alpha \leq 45°$ and $\alpha > 135°$
	$\frac{\sqrt{x^2+z^2}}{S}\lvert\sin\alpha\rvert$ for $45° < \alpha \leq 135°$
α	section angle in the bend
S	section length in the bend at 90° section, $S/D_h = 1$
d_v^*	viscous length scale
u_τ^*	friction velocity
τ_w^*	surface averaged wall shear stress

Greek

δ_{ij}	Kronecker delta
ρ	fluid density
μ	dynamic viscosity of the fluid
α	blending function
ε	turbulent dissipation rate
ν	kinematic viscosity of the fluid
∇	del operator represented by Nabla symbol
ω_m	system rotation vector
τ	turbulent time scale

ABBREVIATIONS

CFD	Computational Fluid Dynamics
DNS	Direct Numerical Simulation
EBM	Elliptic Blending Model
EB-RSM	Elliptic Blending Reynolds Stress Model
HWA	Hot Wire Anemometry
LDV	Laser Doppler Velocimetry
PIV	Particle Image Velocimetry
RSM	Reynolds Stress Model
WB	Wall Bisector

CHAPTER 1: INTRODUCTION

1.1 Overview of the flow in a two-pass channel with a sharp 180° turn

Two-pass channels with a square/rectangular cross-section are commonly used in various types of thermal equipment. An important flow phenomenon of this sharp 180° bend is the formation of the Dean-type secondary motion. The imbalance between the pressure gradient and the centrifugal force acting on the fluid results in the secondary flow. A pressure gradient is developed across the bend section with a higher pressure near the outer surface. This pressure imbalance acts on the fluid and displaces it from the outer wall to the inner wall. On the other hand, the turning of this high momentum fluid produces centrifugal force that drives the flow outwards. As a result, a secondary flow field with two counter-rotating vortices known as Dean vortices develops in the bends of stationary channels.

1.1.1 The concept of Dean vortices

When Reynolds number is low enough in a curved channel flows, the flow is laminar. On the other hand, when the Reynolds number is high, the flow in a curved channel becomes unstable due to centrifugal instabilities. In this condition, the secondary flows subsequently develop which eventually form into pairs of counter-rotating vortices. This flow is referred to as Dean vortex flow (*Dean, 1927*), and the accompanying pairs of streamwise-oriented vortices are referred to as Dean vortices, as shown in Fig. 1-1.

Vortices which develop from centrifugal instabilities are present in a variety of practical applications. Near the concave surfaces of turbine blades, centrifugal instabilities result in the formation of Taylor-Görtler vortices. Within curved cooling passages inside turbine blades, and within curved ducts and pipes used in components such as heat exchangers, vortices may again be present as a result of centrifugal instabilities imposed on the flow. The resulting periodic regions of high and low speed flow in the spanwise direction forms into pairs of counter-rotating streamwise vortices. Circulation magnitudes of the vortices increase with more intense curvature. Such vortices are important since they may cause significant alterations to boundary layer structure and wall heat transfer distributions. Additionally, these vortices also have an important effect on the transition from laminar to turbulent flow.

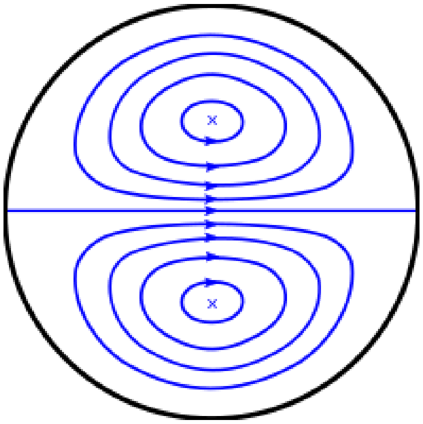

Fig 1-1: Schematic of a pair of Dean vortices formed in two-pass channel (figure from *Kalpakli, 2014*)

1.2 Applications of the two-pass channel

Some of the typical industrial applications include cooling of advanced gas turbine blades and heating of the gas used for thermal sprays. Modern gas turbine blades are subjected to a very high inlet temperature. The increase in the gas entry temperature improves the thermodynamic efficiency of the modern gas turbine engines with subsequent reduction in their specific fuel consumption. This also helps in an increase in the performance of the gas turbines. So, in order to maintain the temperature below the acceptable limits, effective cooling is applied to the turbine components that are exposed to the hot steam.

The gas turbine blades are cooled both internally and externally, as depicted in Fig 1-2. One of the common cooling technologies involves three major internal cooling zones of the turbine blade with strategic film cooling of the leading edge, pressure and suction surfaces, as well as the blade tip region. The leading edge is cooled by jet impingement with film cooling, the middle portion is cooled by serpentine rib-roughened passages with local film cooling, and the trailing edge is cooled by pin fins with trailing edge ejection. Film cooling is also known as external cooling, in which internal coolant air is ejected out through discrete holes to provide a coolant film to protect the outside surface of the blade from hot combustion gases, as shown in Figure 1-2(a). Internal cooling is achieved by means of forced convection by passing the coolant through several enhanced serpentine passages inside the blades and extracting the heat from the outside of the blades, as shown in Figure 1-2(b). Jet impingement cooling, rib turbulators, dimples and pin-fin cooling are used to augment the internal cooling. Thus, the engine cooling system must be designed to ensure that the maximum blade surface temperatures and temperature gradients during operation are compatible with the allowable blade thermal stress for the life of the design. Two-pass channels are also used for heating the gas in thermal spray applications. For a thermal spray, the gas must be quickly heated at temperatures around 900K.

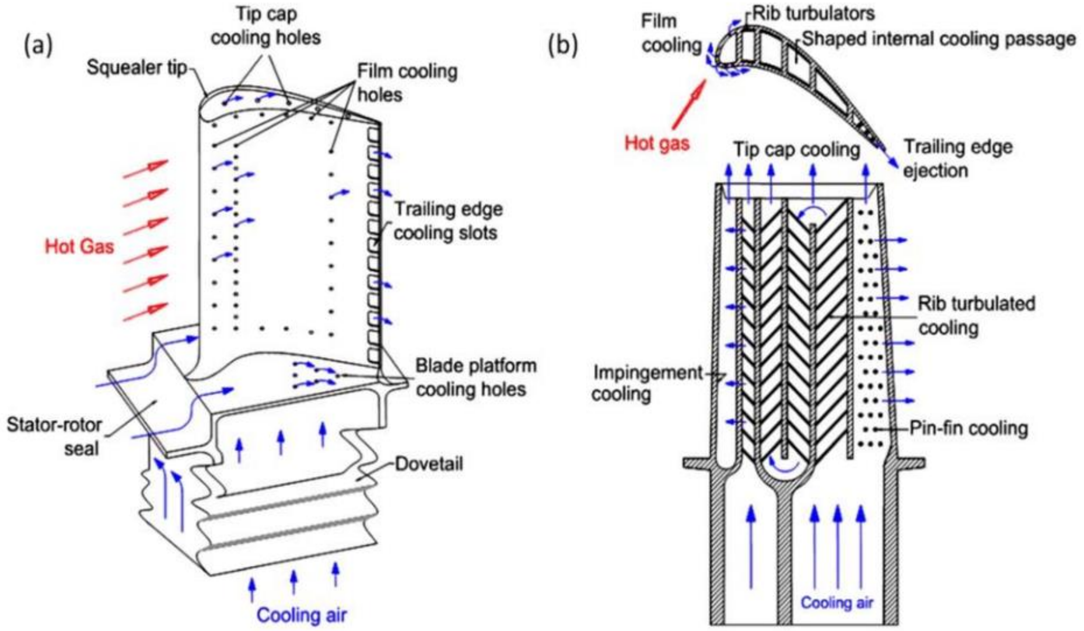

Fig 1-2: Gas turbine blade cooling schematic: (a) film cooling (b) internal cooling (figure from Han *et. al.*, 2012)

1.3 Heat transfer in the two-pass channel

The secondary flow and flow separation at the tip of the divider plate influence the heat transfer in the bend. As the flow progresses through the bend of a smooth passage, the presence of the secondary flow causes higher heat transfer on the top and bottom walls as well as on the outer wall. This is attributed to the higher turbulence of the flow and flow impingement which increases the transport of cold fluid from the bulk towards the walls. Downstream of the bend, higher turbulence and mixing due to the flow separation and reattachment on the divider plate leads to an additional increase of the heat transfer.

Common passive features such as ribs are implemented in gas turbine blades design to increase the heat transfer, as they are easy to manufacture. The ribs augment the boundary layer and cause repeating flow pattern within the passage, which leads to a high turbulence level in the core flow. In the passages, where oblique ribs are mounted in the straight sections, the ribs create a secondary flow, which interacts with the curvature inducing secondary flow in the bend. This leads to a very complex flow field in the turning region.

1.4 Motivation of the study

Over the past decade, forced convection heat transfer in two-pass channels with a sharp turn under the stationary condition has been a major area of interest. While most of the works are experimental, a few recent studies have used Computational Fluid Dynamics (CFD) to model these flows and predict the heat transfer on the blades. Despite the importance of the flow characteristics, many of these studies have concentrated their discussion on the heat transfer aspect, and only a few have provided information on the velocity field and flow structures in the channels. As the flow passes through these channels, the complexity of the Dean-type secondary motion and flow separation in the turn are not well understood. Moreover, there is no conclusive evidence of the influence of the bend clearance on the turbulence parameters of the flow as well as the three-dimensional and symmetric nature of the flow. So, numerical simulations can be used as a tool to investigate the velocity and vorticity fields of the flow as well as to test different geometries. In view of the above, this study aims at a comprehensive investigation of the flow characteristics in a two-pass channel with a sharp 180° turn under a stationary condition. The numerical strategy is divided into 2 parts.

1.4.1 Square duct simulation

The first step is to investigate the turbulent flow in a pressure-driven straight duct with a square cross-section at Reynolds number of 40,000 to reach flow conditions which are representative of fully developed turbulence. The Reynolds number is defined based on the hydraulic diameter (D_h) and bulk velocity (U_b) of the square duct. 3-D steady state simulation of the flow in the square duct is modeled using Reynolds stress turbulence model. The mean velocity and vorticity fields are analyzed at different stream-wise locations of the duct for the fully developed turbulent flow condition. The results from the simulation are validated and compared with the Direct Numerical Simulation (DNS) study of *Pirozzoli et al., (2018)*.

1.4.2 Two-pass channel simulation

The successful numerical strategy for the flow in two-pass channel requires a fully developed inlet condition, which is the second step in this numerical approach. For this purpose, 3-D unsteady simulation using Reynolds stress turbulence model is carried out for investigating the Dean-type secondary motion, flow separation, flow recirculation and three-dimensional nature of the flow. The simulation results are validated and compared with the Particle Image Velocimetry (PIV) experiments carried out by *Schabacker et al., (1998b)*.

1.5 Objectives of the study

The square duct simulation is carried out with the following objectives:

- To analyze the vorticity contours and the secondary flow caused by the redistribution of the momentum in the square duct.
- To observe the flow properties at different locations in the stream-wise direction to obtain the conclusive evidence of the fully developed turbulent flow condition in a square duct. This will serve as an approach flow condition for the inlet of the two-pass channel.

The two-pass channel simulation is carried out with the following objectives:

- To investigate the flow characteristics (mean flow and turbulence parameters) before the bend, in the bend and after the bend.
- To understand the influence of the bend clearance on the turbulence parameters of the flow and the complexity of Dean-type secondary motion, flow separation and flow recirculation.
- To analyze the three-dimensional nature of the flow with different bend clearance.
- To identify the turbulent structures in the flow field of two-pass channel, mainly in the recirculation region and examine the influence of the bend clearance on the turbulent structures formed in the two-pass channel.

CHAPTER 2: LITERATURE REVIEW

This chapter presents the experimental and numerical studies that have been carried out to analyze the flow characteristics in the two-pass channel. Some pioneering studies of flows in the ducts with complex cross-sections are also highlighted. Overall, a summary of the relevant literature pertaining to the studies of square duct and the two-pass channel is discussed.

2.1 Literature related to the square duct

Internal flows within straight ducts with non-circular cross-section are common in many engineering applications, such as water draining, ventilation systems and heat exchangers. A major characteristic of these types of flows is the appearance of secondary flows, first observed by *Prandtl (1927)* and *Nikuradse (1930)*, who proposed the existence of these secondary flows in the cross-stream planes to explain the deviations of the streamwise velocity near the corners. *Nikuradse (1930)* was the first one who measured axial velocity distribution for fully developed turbulent flow in straight ducts of rectangular and triangular cross section. He discovered that the "isovels", i.e. contours of constant velocity, were unreasonably distorted towards the corners. *Prandtl (1927)* postulated that this isovel distortion was caused by transverse or secondary velocities bringing high momentum fluid from the center of the duct towards the corners. In order to preserve continuity, a low momentum fluid flows from the corner region along the walls and back to the duct center. He reasoned that the secondary flows were due to large turbulent fluctuations along the isovel lines that result in centrifugal forces causing flow towards the corners. Therefore, the topology of the secondary motions in a square duct flow consists of eight counter-rotating vortices, bringing high momentum fluid from the core towards the corners *(Prandtl, 1927)*.

Secondary flows are associated with the presence of non-zero streamwise vorticity as referred by *Bradshaw (1964)*, which in turn may arise because of skewing of existing spanwise vorticity as in the case of duct bends. This gives rise to the Prandtl's secondary motions of the first kind. Secondary flows also arise because of Reynolds stress gradients in the presence of a non-circular cross-section. These are referred to as the Prandtl's secondary motions of the second kind. Modelling secondary flows is a challenging task for turbulence models, as the classical models based on the isotropic eddy viscosity assumption cannot generate self-sustained secondary motions in straight ducts (*Mani et al., 2013*). Quantitative measurements of secondary motions in ducts date back to the studies of *Hoagland (1960)*; *Brundrett & Baines (1964)*; *Gessner & Jones (1965)*. *Hoagland (1960)* first attempted to shed light on the mechanisms of vorticity generation and on the effect of Reynolds number variation. Whereas these studies agree that secondary motions are generated from gradients of the Reynolds stresses, *Brundrett & Baines (1964)* reported that the convection of mean streamwise vorticity provides an important contribution to the overall vorticity balance. *Gessner & Jones (1965)* reported convection to be at least one order of magnitude less than the other balanced terms in the mean vorticity equation. The mean streamwise vorticity (ω_x) equation is written as follows:

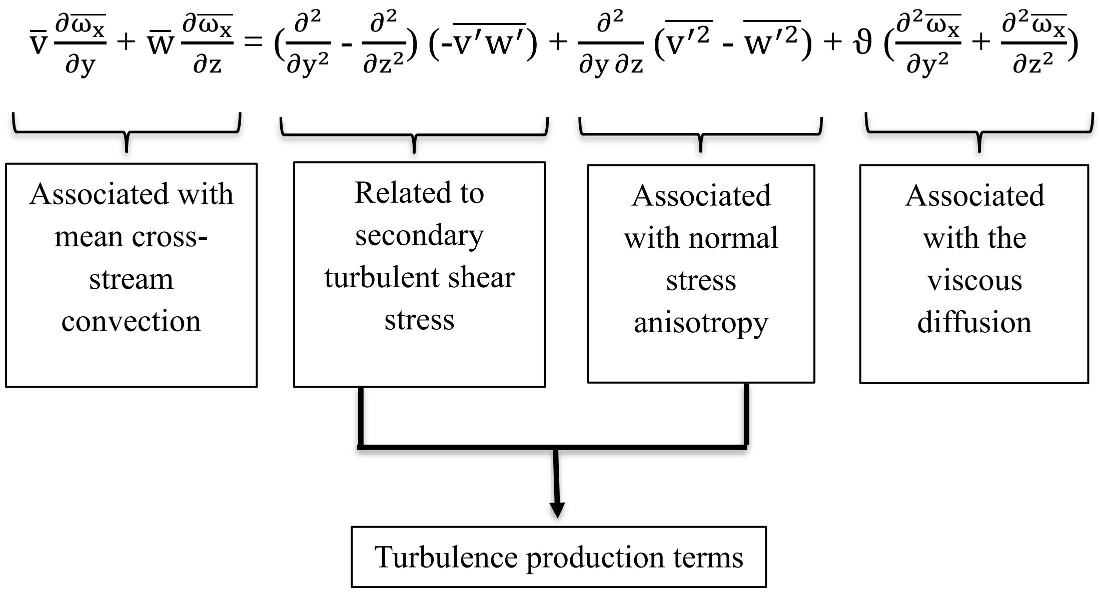

$$\bar{v}\frac{\partial\overline{\omega_x}}{\partial y} + \bar{w}\frac{\partial\overline{\omega_x}}{\partial z} = \left(\frac{\partial^2}{\partial y^2} - \frac{\partial^2}{\partial z^2}\right)\left(-\overline{v'w'}\right) + \frac{\partial^2}{\partial y\,\partial z}\left(\overline{v'^2} - \overline{w'^2}\right) + \vartheta\left(\frac{\partial^2\overline{\omega_x}}{\partial y^2} + \frac{\partial^2\overline{\omega_x}}{\partial z^2}\right)$$

Fig 2-1: Mean streamwise vorticity equation.

Brundrett & Baines (1964) further argued that secondary eddies should not be affected by the Reynolds number, whereas *Gessner & Jones (1965)* found that their intensity decreases with the increasing Reynolds number. Consistent with the latter statement, *Launder & Ying (1972)* argued that the typical velocity scale of the secondary motions is the friction velocity, rather than the bulk velocity. *Demuren & Rodi (1984)* pointed out that the reasons for these contrasting conclusions of experimental studies regarding the Reynolds number dependence of secondary flows are likely due to incomplete flow development or inaccuracy of measurements.

Due to these shortcomings of the experimental studies, the researchers performed Direct numerical simulation (DNS) of the duct flow. It is believed that DNS may be a valuable tool to shed light on the nature of the secondary motions, as it allows one to accurately evaluate all the quantities which may be responsible for their occurrence and sustainment. The first DNS of incompressible square duct flow was carried out by *Gavrilakis (1992)* at bulk Reynolds number of 4410. The findings of this study were also consistent with the statement that in the streamwise vorticity equation, the gradients of Reynolds stresses are approximately balanced by the viscous diffusion, whereas convection is less important. *Vinuesa et al., (2014)* carried out DNS of duct flow in square and rectangular channels at $Re_\tau = 180–300$, with special attention to establishing the effect of the channel aspect ratio. *Zhang et al., (2015)* carried out DNS of square duct flow up to $Re_\tau=600$. They observed a continuous trend in the position of the vortex centres, which move towards the wall bisectors as the Reynolds number increases. *Pirozzoli et al., (2018)* developed a novel DNS database covering the Reynolds number up to $Re_\tau \approx 1000$ ($Re_D \approx 40000$), the highest reached so far. They stated that the turbulent intensity of the secondary motions is mostly unaffected by the Reynolds number variation and they do not have a large influence on the bulk flow properties. So, due to the inconclusive outcome of these studies, a complete understanding of the secondary motion has not been achieved from the fundamental viewpoint. This work is focussed to obtain the fully developed turbulent flow condition including both the primary and the secondary flow properties in a square duct. The results are validated with the DNS study of square duct conducted by *Pirozzoli et al., (2018)*. Furthermore, the numerical strategy for the two-pass channel requires a fully developed turbulence inlet condition.

2.2 Literature related to the two-pass channel.

Many researchers have conducted research on the flow and heat transfer in two-pass channels from the perspective of gas turbine blade cooling. Detailed data on heat transfer in the two-pass channels is essential for a critical design of thermal equipment used under a severe thermal condition. In response to such demand, several studies were conducted on forced convection heat transfer in two-pass channels with a sharp turn under the stationary condition.

The typical studies on the heat transfer characteristics in such channels are presented by *Metzger & Sahm (1986),* where the overall heat transfer characteristics in two-pass smooth rectangular channels were studied by varying the divider location and the turn clearance at different geometries. *Metzger & Sahm (1986)* used the Hot Wire Anemometry (HWA) technique with air as the testing fluid and all testing was carried out at steady state conditions. *Metzger & Sahm (1986)* measured Nusselt numbers for forced convection within and around two-pass smooth channel of rectangular cross-section. *Son et al., (2002)* carried out experiments using PIV to correlate the high Reynolds number turbulent flow and wall heat transfer characteristics in a two-pass square channel with smooth and ribbed walls. They reported that flow impingement is the primary factor for the two-pass square channel heat transfer enhancement rather than the flow turbulence level itself. The characteristics of the secondary flow, for example, vortex’s shape, strength, rotating-direction and positions, are closely correlated with the wall heat transfer enhancements for both smooth and ribbed wall two-pass square channels.

Ekkad et al., (2000); *Ekkad & Han (1997)*; *Han et al., (1988)*; *Murata & Mochizuki (2004)* investigated the influence of the ribs attached on the channel walls. It was observed that the rib angle, rib orientation, and the sharp 180° turn significantly affected the local heat/mass transfer distributions. The combined effects of these parameters increased or decreased the heat/mass transfer coefficients after the sharp 180° turns. The detailed heat transfer coefficient in the two-pass square channel was reported using liquid crystal technique by *Ekkad & Han (1997)*. *Park & Lau (1998)* also investigated the sharp-turning flows in a two-pass square channel using the naphthalene mass transfer technique for a relatively low-Reynolds number of 5500. *Rau et al, (1998)* investigated the effect of ribs on heat transfer enhancement and flow distribution in a straight channel. They presented that the secondary flows, which were generated by the ribs, have effect on the local heat transfer enhancement at the lateral walls. *Astarita & Cardone (2000)* presented the local heat transfer coefficients in smooth two pass channels with different aspect ratios and constant turn clearance. Heat transfer measurements were performed by means of the heated-thin-foil technique, which practically corresponds to a constant heat flux boundary condition, and by using infrared (IR) thermography. The fluid used during the test was air and the Reynolds number was varied between 16,000 and 60,000.

Chyu (1991) investigated the heat transfer distributions for flow in two and three-pass channels with 180° sharp turns using analogous naphthalene mass transfer technique. *Chyu (1991)* found that the overall heat transfer for the three-pass channel was higher than the two-pass channel by 15% and was independent of the Reynolds number.

He also mentioned that the heat transfer at the first turn has already reached the thermally developed (periodic) condition. *Hirota et al., (1999)* presented heat/mass transfer characteristics for turbulent flow in rectangular cross-sectioned two-pass channel with a sharp 180° turn. They used naphthalene sublimation method for their experiments with three different turn clearances. *Gallo & Astarita (2010)* carried out PIV experiments to obtain visualization and measurements of mean and secondary flow field in a square channel with a sharp turn.

Investigation of the fluid dynamics inside the 180° turning critical regions of coolant passages is necessary to properly understand the convection heat transfer since the two (heat transfer and fluid dynamics) are closely correlated as heat and momentum transfer phenomena. Although the detailed study of flow characteristics is important for a better understanding of the complex heat transfer mechanism in these channels, only few results are found in open literature because of considerable difficulties in measuring them with high accuracy. *Nakayama et al., (2006)* measured flow characteristics in stationary two pass channel with a sharp 180° turn using LDV (Laser Doppler Velocimetry) for a Reynolds number of 35,000. The main features of the flow such as flow separation, recirculation and secondary flow were presented at a Reynolds number of 35,000. According to his study, the velocity data on the channel walls reveals that the wall-normal velocity mainly dominates the heat transfer in the channel. *Saha & Acharya (2013)* presented a comparative numerical study of turbulent flow in a two-pass channel with different bend geometries. They found that the bend geometry can have a significant effect on the overall heat performance of a two-pass channel. The study used a finite volume solver using Reynolds Averaged Navier-Stokes (RANS) based two equations realizable k-ϵ model with enhanced wall treatment.

Previous experiments to define the flow characteristics and to provide data for CFD evaluation have the LDV measurements in stationary two-pass channels by *Iacovides et al., (1998)* and *S.C. Cheah et al, (1994)*. According to their studies, in the stationary case, a three-dimensional separation bubble is formed along the inner wall, causing the generation of high-turbulence levels. Along the outer side, opposite to the separation bubble, turbulence levels are suppressed due to streamwise flow acceleration. *Liou & Chen (1999)* performed LDV measurements of the developing flow through a smooth duct with a 180° straight corner turn.

Studies by *Schabacker et al., (1998)* report mean and fluctuating velocity fields measured in two-pass square smooth and ribbed channel using stereoscopic PIV system. They showed the influences of the turn and the ribs on the overall flow characteristics. *Liou et al, (2000)* and *Liou & Chen (1999)* made a series of experimental studies on the velocity distributions in a 180° sharp turning duct using LDV; their attention was directed to the influence of the divider wall thickness. They reported the thickness effect of the flow divider on the flows in a two-pass smooth square channel with a 180° sharp turn at a free stream Reynolds number of 12,000. *Eggels et al., (1994)* reported on turbulent channel flow measurement using the PIV technique. The accuracy of PIV measurements for turbulent channel flows was compared with pointwise measurement techniques with much higher spatial resolution that is time resolved. The PIV technique also improved the spatial resolution near the channel wall region. *Jang et al, (2001)* reported the computational results of the flow and heat transfer in two-pass channel for Reynolds number of 30,000. Especially, they studied the effect of the angled rib (60° inclined from the flow axis) on the channel surface heat transfer.

Among the investigations on heat transfer characteristics conducted to date, the researchers made a series of experiments to make clear the effect of channel geometry on the heat transfer using the naphthalene sublimation method (*Hirota et al., 2002, 1999, 1997; Syuhada et al., 2001*). Though it is of fundamental interest and of practical importance to make clear the influence of the turn clearance on the flow characteristics in two-pass channels with a 180° sharp turn, very few discussions have been mentioned on this issue. In view of the above summary, this study aims at a comprehensive investigation of the influence of the turn clearance on the flow characteristics in a two-pass channel.

The effect of the bend on the heat transfer in smooth and ribbed stationary passages has been experimentally studied by *Ekkad & Han (1997)*; *Han et al., (1988)*; *J.C. Han, P. Zhang, (1991)* and *Metzger & Sahm (1986)*. Their studies collectively indicate that the secondary flows and flow separation at the tip of the divider plate influence the heat transfer in the bend. For the design of gas turbine blades, a detailed knowledge of the physical phenomena in the passage is necessary. The CFD simulations can provide a better understanding of this phenomena. This is especially important for the complicated heat transfer patterns in the turning region of stationary coolant passages.

In summary, many studies have been conducted on the flow and heat transfer in two-pass channels with a 180° turn. Despite the importance of the flow characteristics, many of these studies have concentrated their discussion on the heat transfer aspect, and only a few have provided information on the velocity fields and flow structures in the channels. So, numerical simulations can be used as a tool to investigate the flow characteristics in these types of channels. Therefore, in this research, the computational investigations are performed to understand the influence of the bend clearance on the turbulence parameters of the flow and the complexity of Dean-type secondary motion and the three-dimensional nature of the flow. Furthermore, the flow characteristics before the bend, in the bend and after the bend are quantitatively and qualitatively validated with *Schabacker et al., (1998)*.

CHAPTER 3: METHODOLOGY

This chapter discusses the methodology adopted for the study of highly turbulent three-dimensional flow in the pressure-driven square ducts and the two-pass channels with a sharp 180° bend. It covers the various turbulence modelling approaches relevant to this thesis. The present simulations are done using the anisotropic RANS model i.e. Reynolds Stress Model (RSM). These simulations are carried out using the commercial code STAR-CCM+ solver. This solver uses the finite volume approach to discretize the governing Navier-Stokes equations. This code is well suited in handling complicated flow problems (*Jesudhas et al., 2018*), as well as complex geometries (*Nasif et al., 2014*). The complete formulation for RSM is presented based on the equations from STAR-CCM+ User Guide.

3.1 Overview

The advantage of using RSM is having access to shear stresses that are not available from the two-equation RANS-based closure models like k-ϵ and k-ω. These shear stresses will aid in the understanding of how the clearance of the bend will affect the flow properties, particularly in the recirculation region of the separation bubble. In this research, the RSM turbulence model has been successfully applied in simulating the turbulent flow in a pressure-driven square duct at high Reynolds number (Re = 40,000) to reach the flow conditions which are representative of fully developed turbulence. The results from the simulation are validated and compared with the DNS study available in the literature *Pirozzoli et al., (2018)*. After validation, another square duct simulation at higher

Reynolds number (Re = 50,000) is carried out because the numerical strategy for the two-pass channel requires a fully developed turbulent inlet condition. The RSM turbulence model available in the Star-CCM+ is applied to the two-pass channel with a sharp 180° bend and the results of this simulation (Re = 50,000) before the turn, in the turn and after the turn are validated by comparing it with the PIV data provided by the *Schabacker et al., (1998).*

3.2 Turbulence Modelling Approaches

Modelling turbulence is the subject of ongoing intensive research over the last 50 years. The complexity of modelling turbulence arises from the different scales of the flow that must be resolved.

3.2.1 Reynolds-Averaged Navier-Stokes turbulence model

All CFD studies are based on the fundamental equations of continuity, momentum, and energy. For this study, the fluid domain is considered isothermal and incompressible, so the energy equation is ignored. The conservation of mass and momentum yields the governing equations for the flow of an incompressible fluid:

Continuity Equation:

$$\frac{\partial}{\partial x_j}\left(u_j\right) = 0 \tag{3.1}$$

Momentum Equation:

$$\frac{\partial(u_i)}{\partial t} + \frac{\partial}{\partial x_j}\left(u_i u_j\right) = \frac{\partial}{\partial x_j}\left[-p\delta_{ij} + \mu\left(\frac{\partial u_i}{\partial x_j} + \frac{\partial u_j}{\partial x_i}\right) - \frac{2}{3}\mu\frac{\partial u_k}{\partial x_k}\delta_{ij}\right] \tag{3.2}$$

The momentum equation (3.2) is developed by applying Newton's second law of motion to a three-dimensional fluid particle and is referred to as the Navier-Stokes (N-S) equations. These equations form a close set of four equations with four unknowns (component velocities u_1, u_2, u_3, and pressure, p). A full 3-D analytical solution to these nonlinear equations exist, but exact solutions are available for a variety of flows with simplifying assumptions. For turbulent flows, the instantaneous velocity and pressure variables are comprised of a time-averaged mean and a fluctuation (known as Reynolds decomposition):

$$u_i = \bar{u}_i + u'_i \tag{3.3}$$

$$p = \bar{p} + p' \tag{3.4}$$

Inserting the instantaneous velocities and pressures into the N-S equations and time averaging yields a set of Reynolds-Averaged Navier-Stokes (RANS) equations:

$$\frac{\partial \bar{u}_i}{\partial x_j} = 0 \tag{3.5}$$

$$\frac{\partial(\rho\bar{u}_i)}{\partial t} + \frac{\partial}{\partial x_j}\left(\rho\bar{u}_i\bar{u}_j\right) = \frac{\partial}{\partial x_j}\left[-\bar{p}\delta_{ij} + \mu\left(\frac{\partial\bar{u}_i}{\partial x_j} + \frac{\partial\bar{u}_j}{\partial x_i}\right) - \rho\overline{u'_i u'_j}\right] \qquad (3.6)$$

The momentum equation (3.6) has an additional six unknown terms representing the convective momentum due to the velocity fluctuations. The other terms, $-\rho\overline{u'_i u'_j}$, are called the turbulent stresses and without the density, $\overline{u'_i u'_j}$, they are referred to as the turbulent kinematic stresses or Reynolds stresses. The main goal in turbulence modeling is to develop a suitable closure method to predict the Reynolds stresses. Different types of turbulence closure methods have been developed, each with its own set of physics, advantages, disadvantages, and applicability for certain types of flows. *Versteeg and Malalasekera (1995)* provides a good summary of the most popular methods.

In summary, the Reynolds-Averaged Navier-Stokes (RANS) model:

- solves the time averaged Navier-Stokes equations.
- resolves the mean quantities and models the turbulence quantities, leading to moderate computational cost.

3.3 Reynolds Stress Turbulence Model

In this research, the Reynolds Stress Model (RSM), also referred to as the Reynolds Stress Transport (RST) model, was selected for turbulence closure because:

- It can potentially predict complex flows more accurately than eddy viscosity models.
- The transport equations for the Reynolds stresses account for the effects of turbulence anisotropy and streamline curvature.
- RSM computes the components of the specific Reynolds stress tensor to provide closure to the RANS equations.

RST models, also known as second-moment closure models, directly calculate the components of the specific Reynolds stress tensor by solving their governing transport equations. The starting point for the development of an RST model is generally the exact differential transport equation for the Reynolds stresses, which is derived by multiplying the instantaneous Navier-Stokes equations by a fluctuating property and Reynolds averaging their product. In the resulting equations, the transient, convective and molecular diffusion terms do not require modeling. The terms remaining to be modeled are the turbulent diffusion term, the dissipation term and, perhaps the greatest challenge, the pressure-strain term.

The application of the RSM closure method for the computational investigation of this two-pass channel problem is a more advanced technique than one or two-equation turbulence models, often complex and computationally expensive. In addition to the six extra equations needed to solve for the Reynolds stress components, an additional model equation is needed for the turbulent dissipation, ϵ. The boundary conditions for the additional equations are a major source of cost and complexity. The RSM modeling strategy originated from *Launder et al., (1975)* and variations of the transport equations have been developed over the years. Star-CCM+ offers a choice of four different Reynolds stress transport models: a linear pressure strain, quadratic pressure strain, two-layer linear pressure strain and elliptic blending.

To model the pressure strain term, the following approaches are implemented in Simcenter STAR-CCM+:

- Linear pressure strain
- Quadratic pressure strain

The Linear pressure strain model can be used with a high y^+wall treatment, but it is also available with a two-layer formulation, which makes it applicable right down to the wall.

The Quadratic pressure strain model and the Elliptic Blending Model (EBM), are based on the most recent and precise formulation of the pressure strain term. Thus, they are likely to be the models of choice. In most of the cases, the EBM being preferred as it also contains specific treatments for all y^+ meshes. The Quadratic pressure strain model can only be used with a high y^+ wall treatment (that is, using wall functions) without resolving the viscous-affected near-wall region.

For this research, the Elliptic Blending Model was selected for stability and because it allows for a hybrid y^+ wall treatment for both coarse and fine meshes.

3.3.1 Elliptic Blending Reynolds Stress Model (EB-RSM)

The Elliptic Blending RST model of *Manceau & Hanjalić (2002)* is based on a near-wall formulation of the quasi-linear quadratic pressure strain term. The blending function is used to blend the viscous sub-layer with the log-layer formulation of the pressure strain term. This approach requires the solution of an elliptic equation for the blending parameter α.

Their model has gone through several improvements over the years. The version of the model implemented in STAR-CCM+ was revised by *Lardeau & Manceau (2016)*. The transport equations for the Reynolds stresses $\overline{u_i' u_j'}$ takes the following form:

$$\frac{D\overline{u_i' u_j'}}{Dt} = P_{ij} + \phi_{ij}^* - \varepsilon_{ij} + D_{ij}^t + \frac{\partial}{\partial x_k}\left(\nu \frac{\partial \overline{u_i' u_j'}}{\partial x_k}\right) \qquad (3.7)$$

In CFD computations with the Reynolds stress transport equations, the production term can be retained in the exact form. To obtain a solvable form of (3.7), we need models for the turbulent diffusion, the dissipation rate and the pressure strain correlation terms on the right-hand side. In the near-wall region, the no-slip boundary condition and the incompressibility of the fluid impose the limiting behavior of the fluctuating quantities, and the Reynolds stresses. So, the reproduction of the limiting wall behavior of $\phi_{ij}^* - \varepsilon_{ij}$ and, consequently of the Reynolds stresses is the only way to ensure a correct prediction of the wall-induced anisotropies in general configurations. Therefore, this is the main idea followed in the derivation of the elliptic blending model.

The production term is as follows:

$$P_{ij} = -\left(\overline{u_i' u_k'}\frac{\partial \bar{u}_j}{\partial x_k} + \overline{u_j' u_k'}\frac{\partial \bar{u}_i}{\partial x_k}\right) \tag{3.8}$$

The EB-RSM is based on the blending of the near-wall and inhomogeneous models for the pressure strain and dissipation term:

$$\phi_{ij}^* - \varepsilon_{ij} = (1 - \alpha^3)\left(\phi_{ij}^w - \varepsilon_{ij}^w\right) + \alpha^3\left(\phi_{ij}^h - \varepsilon_{ij}^h\right) \tag{3.9}$$

where, the blending parameter α is solution of the elliptic equation

$$\alpha - L^2\nabla^2\alpha = 1 \tag{3.10}$$

with the length-scale L defined as

$$\mathrm{L} = C_l \max\left(\frac{k^{\frac{3}{2}}}{\varepsilon}, C_\eta \frac{\nu^{\frac{3}{4}}}{\varepsilon^{\frac{1}{4}}}\right) \tag{3.11}$$

An important property of this model is that it does not require the computation of an expensive wall distance. Indeed, the wall-normal direction can be computed directly from the elliptic-blending parameter, using

$$n_k = \frac{\partial\alpha/\partial x_k}{\sqrt{\frac{\partial\alpha}{\partial x_l}\frac{\partial\alpha}{\partial x_l}}} \tag{3.12}$$

In the outer region, the quasi-linear version is used for the pressure strain

$$\phi_{ij}^h = -\left(C_1 + C_1^*\frac{P}{\varepsilon}\right)\varepsilon a_{ij} + \left(C_3 - C_3^*\sqrt{a_{kl}\, a_{kl}}\right)k S_{ij} + C_4 k\left(a_{ik}S_{jk} + a_{jk}S_{ik} - \frac{2}{3}a_{lm}S_{lm}\delta_{ij}\right) + C_5 k\left(a_{ik}W_{jk} + a_{jk}W_{ik}\right) \tag{3.13}$$

And in the near-wall layer

$$\phi_{ij}^{w} = -5\frac{\varepsilon}{k}\left[\overline{u_i'u_k'}n_j n_k + \overline{u_j'u_k'}n_i n_k - \frac{1}{2}\,\overline{u_k'u_l'}n_k n_l\left(n_i n_j + \delta_{ij}\right)\right] \tag{3.14}$$

For the dissipation rate tensor, we use

$$\varepsilon_{ij}^{w} = \frac{\overline{u_i'u_j'}}{k}\varepsilon\,; \quad \varepsilon_{ij}^{h} = \frac{2}{3}\varepsilon\delta_{ij} \tag{3.15}$$

where ε is the solution of the equation

$$\frac{D\varepsilon}{Dt} = \frac{1}{\tau}\left(C_{\varepsilon_1}P - C_{\varepsilon_2}\varepsilon\right) + D_{\varepsilon}^{t} + \frac{\partial}{\partial x_k}\left(\nu\,\frac{\partial\varepsilon}{\partial x_k}\right) \tag{3.16}$$

The turbulent time scale τ is defined as

$$\tau = \max\left(\frac{k}{\varepsilon}, C_t\sqrt{\frac{\nu}{\varepsilon}}\right) \tag{3.17}$$

The following definitions are also used throughout the model

$$P = \frac{1}{2}P_{ii}; \qquad a_{ij} = \frac{\overline{u_i'u_j'}}{k} - \frac{2}{3}\delta_{ij}$$

$$S_{ij} = \frac{1}{2}\left(\frac{\partial\bar{u}_i}{\partial x_j} + \frac{\partial\bar{u}_j}{\partial x_i}\right); \qquad W_{ij} = \frac{1}{2}\left(\frac{\partial\bar{u}_i}{\partial x_j} - \frac{\partial\bar{u}_j}{\partial x_i}\right) + \epsilon_{mji}\omega_m \tag{3.18}$$

The turbulent diffusion terms D_{ij}^{t} *and* D_{ε}^{t} are modelled with the assumption that the rate of transport of Reynolds stresses by diffusion is proportional to the gradients of Reynolds stresses. Commercial CFD codes often favour the simplest form:

$$D_{ij}^{t} = \frac{\partial}{\partial x_m}\left(\frac{\nu_t}{\sigma_k}\frac{\partial\overline{u_i'u_j'}}{\partial x_m}\right) = div\left(\frac{\nu_t}{\sigma_k}grad\left(\overline{u_i'u_j'}\right)\right) \tag{3.19}$$

$$D_{\varepsilon}^{t} = \frac{\partial}{\partial x_m}\left(\frac{\nu_t}{\sigma_\varepsilon}\frac{\partial\varepsilon}{\partial x_m}\right) = div\left(\frac{\nu_t}{\sigma_\varepsilon}grad\varepsilon\right) \tag{3.20}$$

This assumption is based on the generalized gradient diffusion hypothesis while in this EB-RSM model, a more robust simple gradient diffusion hypothesis is used where the turbulent eddy-viscosity ν_t is defined as

$$\nu_t = \left[(1-\alpha^3)\overline{u_i' u_j'}n_i n_j + \alpha^3 k\right] C_\mu \tau \tag{3.21}$$

Values for the constants and coefficients used for the EB-RSM equations are listed in Table 3-1.

C_{ε_1}	C_{ε_2}	σ_k	σ_ε	C_μ	C_t	C_l	C_η	C_1	C_1^*	C_3	C_3^*	C_4	C_5
1.44	1.83	1.0	1.15	0.07	6	0.133	80	1.7	0.9	0.8	0.65	0.625	0.2

Table 3-1: Constants used for the EB-RSM equations

The pressure strain interactions constitute one of the most important and difficult terms to model accurately. Their effect on the Reynolds stresses is caused by two distinct physical processes: (*i*) a ‘slow’ process that reduces anisotropy of the turbulent eddies due to their mutual interactions; and (*ii*) a ‘rapid’ process due to interactions between turbulent fluctuations and the mean flow strain that produces the eddies such that the anisotropic production of turbulent eddies is opposed. The overall effect of both the processes is to redistribute energy amongst the normal Reynolds stresses ($i = j$) so as to make them more isotropic and to reduce the Reynolds shear stresses ($i \neq j$).

3.4 Numerical Method

In this research, both steady and unsteady incompressible flow simulations are performed. The segregated solver of Star-CCM+ is used which solves the flow equations (one for each velocity component and one for pressure) in a second-order accuracy scheme. The under-relaxation factors are set to 0.5 for velocity and 0.2 for pressure. The solver description is in reference to a momentum interpolation method for non-staggered grids proposed by *Rhie & Chow, (1983)*. For implicit unsteady simulations, the results of the steady simulations are used as initial conditions.

A second-order temporal discretization scheme is used with a 0.001 second time step. An adjustable time step scheme is used by using the CFL time step control model. The minimum time step is set at 0.0001 second. The Target Mean CFL number and the Target Maximum CFL number used are 1.0 and 2.0 respectively.

The stopping criterion is set by using the New Monitor Criterion in the implicit unsteady solver. The monitors for all the equations are created and the minimum convergence limit is set at 1.0E-8 for each monitor. This means that at every time step, the residuals of each monitor will converge at least to 1.0E-8 and then move to the next time step in order to maintain the numerical stability and prevent the solution from diverging.

In each simulation, the time averaged quantities are measured after 10 flow through cycles. The convective Courant number is kept between 1 and 2, especially near the bend region, to maintain numerical stability. For all the simulations, the values of the residuals, inlet mass flow rate and outlet mass flow are monitored for the convergence criteria to be satisfied.

3.5 Computational domain of the square duct

Figure 3-1 shows a schematic diagram of the geometry of the square duct. The flow path in the downstream leg of the square duct has a cross-section of 0.1x0.1 m^2 with a corresponding hydraulic diameter D_h = 0.1 m and a length of 10 D_h. A 3-D, steady and incompressible flow numerical simulation is performed at a Reynolds number of 40,000 with the recycling boundary conditions from the outlet to inlet. Water is used as the working fluid. This simulation is primarily focused on achieving the fully developed turbulent flow condition for both the mean flow and the turbulence parameters. The results from the simulation were validated and compared with the DNS study of the square duct (*Pirozzoli et al., 2018*).

After validation, another square duct simulation is performed on the same geometry but at a higher Reynolds number of 50,000. Now, air is used as the working fluid. It is carried out to meet the fully developed turbulence inlet condition in the numerical strategy for the two-pass channel, which is the second step in this numerical approach.

The origin of the co-ordinate system is set at the center of the inlet of the square duct. In this Cartesian system, *x* is defined as positive in the stream-wise direction of the flow, *y* is defined positive vertically upwards in the horizontal straight duct, and *z* is defined as positive in the span-wise direction of the flow.

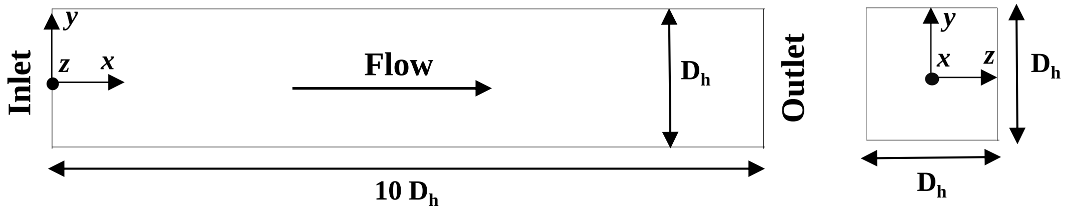

Fig 3-1: Schematic of the square duct.

3.6 Computational domain of the two-pass channel.

Figure 3-2 and Figure 3-3 present a schematic diagram of the geometry of the two-pass channel. The geometry of the channels is essentially the same with the aspect ratio of the channel cross section as 1, and two different turn clearances are tested under a Reynolds number of 50,000.

The model of the coolant passage usually consists of two square ducts which are connected by a sharp 180° bend with a rectangular end wall. Here, air is chosen as the working medium. The flow path in the downstream and upstream leg of the channel has a cross-section of 0.1x0.1 m^2 with a corresponding hydraulic diameter $D_h = 0.1$ m. The flow path in the upstream and downstream legs of the channel has a length of $8D_h$ and $19D_h$ respectively. The thickness of the divider plate is $0.1D_h$. In the straight-corner turn, the clearance between the tip of the divider plate and the end wall is equal to D_h. This case of turn clearance equal to the channel width is a standard turn geometry that has been commonly studied.

By changing the length of the divider wall, the turn clearance "*C*" is set at D_h or $0.5D_h$. The distance between the channel entrance (inlet) and the end wall is $9D_h$ for both the turn clearances; thus, the distance between the channel entrance (inlet) and the divider-wall tip changes from 0.8m (i.e. $8D_h$) to 0.85m (i.e. $8.5D_h$), depending on *C*.

The origin of the co-ordinate system is set on the bottom wall at the turn entrance/exit plane. In this Cartesian (*x*,*y*,*z*) system, *x* is defined as positive in the stream-wise direction of the flow downstream of the bend exit, *y* is defined positive vertically upwards in the horizontal test section orientation, and *z* is defined as positive in the span-wise direction of the flow.

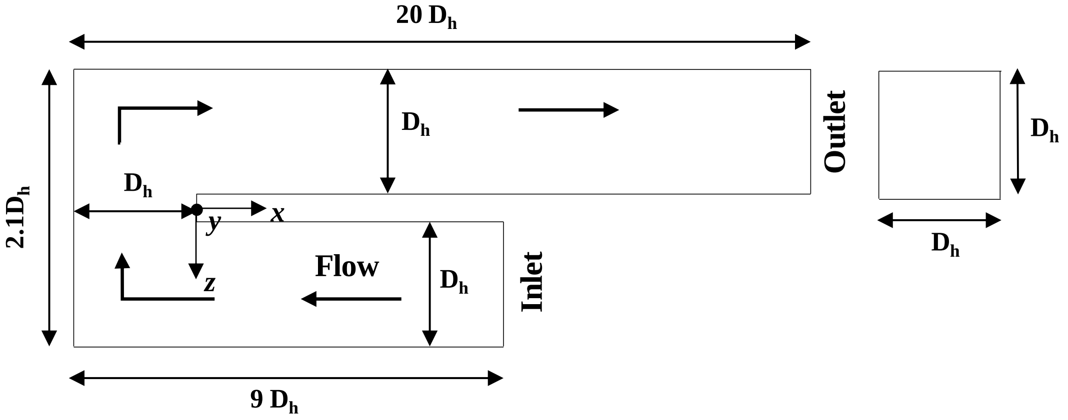

Fig 3-2: Schematic of the two-pass channel with D_h as bend clearance.

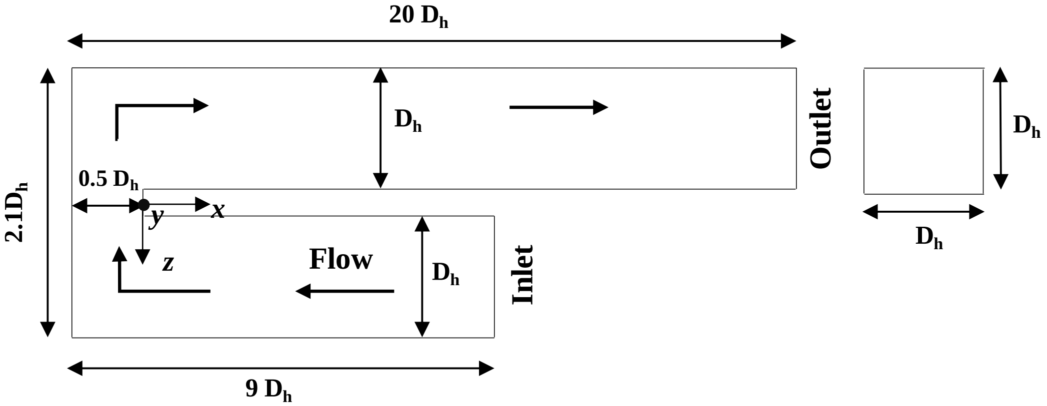

Fig 3-3: Schematic of the two-pass channel with $0.5D_h$ as bend clearance.

So, this chapter summarizes that in providing a solution to the RANS equations, RSM provides direct computation of the Reynolds shear stress components, as opposed to the eddy viscosity approach used in k-ϵ and k-ω turbulence models. The different RSM strategies available in the STAR-CCM+ are discussed and the EB-RSM is applied for the turbulence closure in both the square duct and the two-pass channel simulations to produce an accurate and stable solution. The numerical method and the solver settings used in the simulations are delineated in this chapter. The computational domains indicating the schematic of the duct and the two-pass channel (with different bend clearances) are also covered in this methodology. The next section will now progress towards the validation of the results. Moreover, the interesting physical results obtained from this research will also be discussed.

CHAPTER 4: CFD VALIDATION, RESULTS & DISCUSSION

This chapter presents the validation and analysis of the computational results for the square duct and the two-pass channel. The discussion starts with the analysis of the grid independence study to establish validation of the numerical procedure. The validation of mean flow and turbulence parameters, for both the square duct and the two-pass channel are discussed in this chapter. As outlined in the preceding chapter, the focus of the discussion of the straight pressure-driven square duct simulation is to establish the flow conditions representative of the fully developed turbulent flow. Once the flow in the outlet of the straight duct satisfies the fully developed turbulent conditions, the present numerical strategy applies this as an inlet flow condition for the two-pass channel simulations. Furthermore, the results from the unsteady two-pass channel simulation at Reynolds number of 50,000 are verified against the experimental results of *Schabacker et al., (1998)* in three stages: before the bend, in the bend and after the bend. This chapter also examines the effect of the bend clearance on the flow and turbulence characteristics in the two-pass channel. Moreover, the influence of the bend clearance is analyzed by comparing the mean flow and turbulence properties in the impinging and recirculation zones.

4.1 Steady state square duct simulation

A steady state simulation is performed at a Reynolds number of 40,000 in a straight duct to obtain the fully developed turbulent flow by recycling the boundary conditions from outlet to inlet.

4.1.1 Grid Independence Study

The grid independence study is carried out with three different hexahedral mesh configurations; with a total of $2x10^6$ cells, $4x10^6$ cells and $8x10^6$ cells respectively. The trimmer mesh available in STAR-CCM+ provides a robust and efficient method by producing a high-quality grid for both simple and complex mesh generation problems. It provides a hexahedral mesh. The refinement of the mesh is based upon the surface mesh size and other user-defined refinement controls.

Figures 4-1(a) and (b) depict the logarithmic law of the wall at the wall bisector at two stream-wise locations of at $x/D_h = 2$ and 6 respectively. As expected, the stream-wise mean velocity profiles for different mesh configurations with $2x10^6$, $4x10^6$ and $8x10^6$ cells obey the logarithmic law of the wall. Figures 4-2 and 4-3 show profiles of $\bar{V}$ and τ_w for all mesh configurations. Figures 4-2(a) and (b) depict profiles of $\bar{V}$ near the side wall at $z/D_h = -0.75$ for two different stream-wise locations at $x/D_h = 2$ and 6. In both the cases, the mesh with $2 \text{ x } 10^6$ cells deviates from the other mesh configurations. The wall shear stress (τ_w) is presented in Figures 4-3 for all mesh configurations. After careful observation of the variations of $\bar{U}$, $\bar{V}$ and τ_w distributions at the selected locations for different mesh configurations, it was decided that the intermediate mesh with $4 \text{ x } 10^6$ cells is the best compromise for the accuracy of the results.

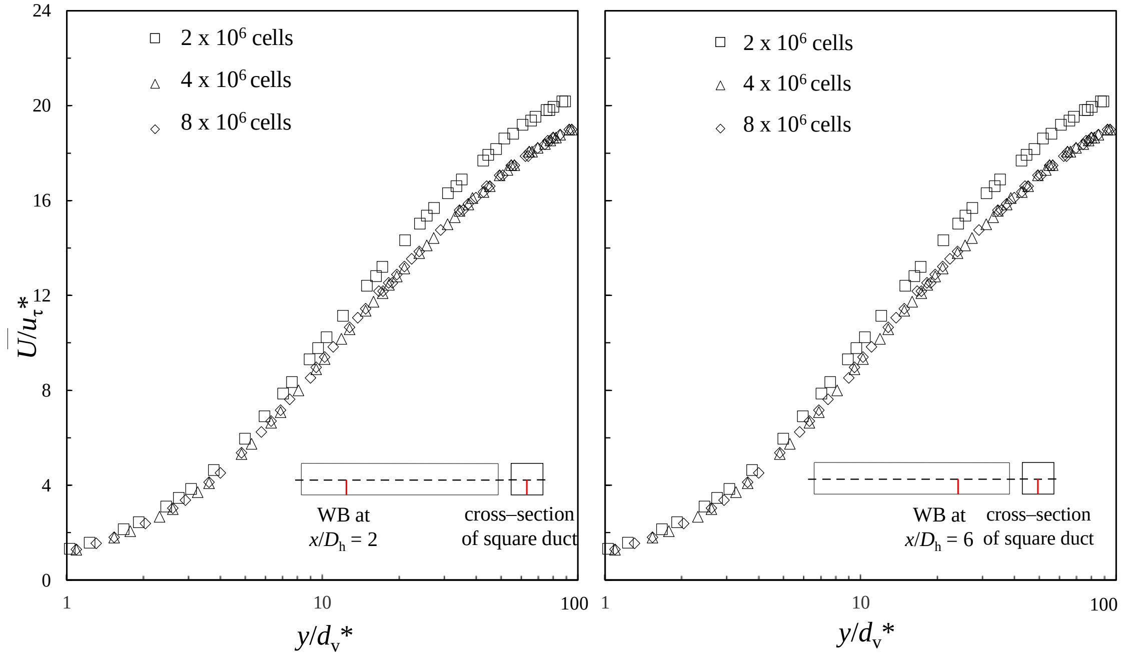

(a) **(b)**

Fig 4-1: Comparison of different meshes of square duct for profiles of mean velocity, $\overline{U}$, for different square duct meshes at wall bisector (WB) at (a) $x/D_h = 2$ and (b) $x/D_h = 6$. Schematic represents the position of the respective profiles.

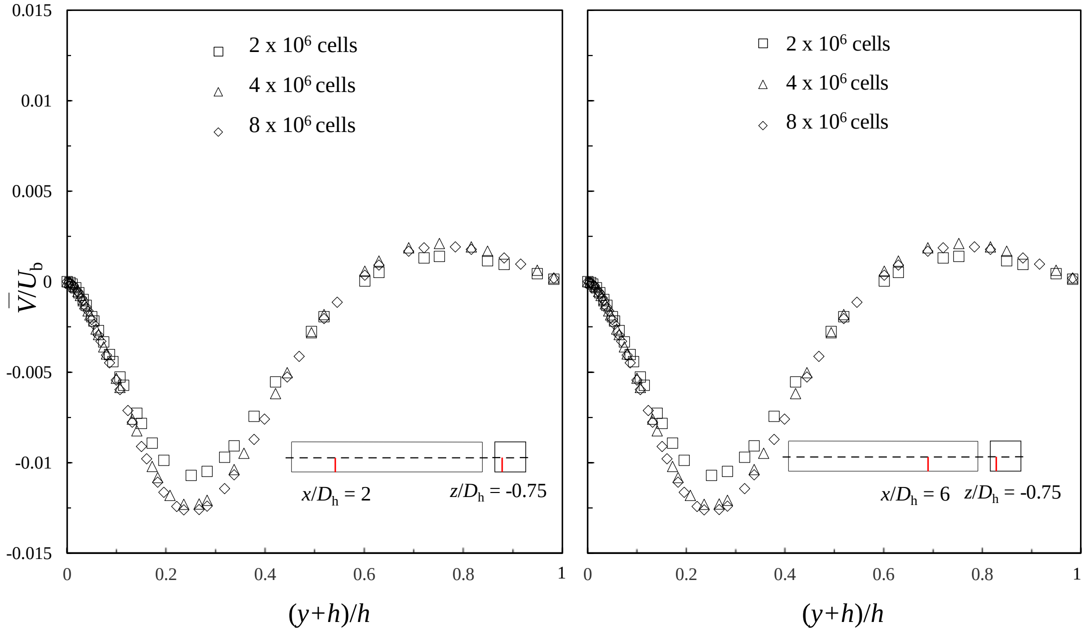

(a) **(b)**

Fig 4-2: Profiles of cross-stream velocity, $\overline{V}$, at z/D_h = -0.75 for different square duct meshes located at (a) x/D_h = 2 and (b) x/D_h = 6.

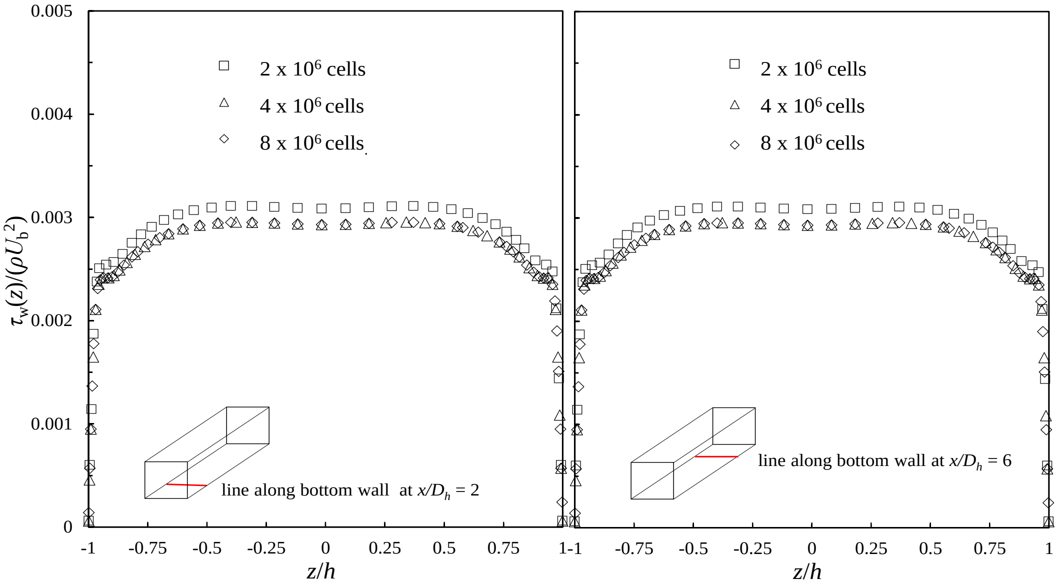

(a) **(b)**

Fig 4-3: Normalized wall shear stress along the bottom wall for different square duct meshes at (a) x/D_h = 2, and (b) x/D_h = 6.

4.1.2 Validation of fully developed turbulent flow in a straight square duct

The validation procedure adopted in this study is based on the American Institute of Aeronautics and Astronautics (AIAA) guidelines for verification and validation of CFD simulations. These guidelines encourage a ‘building block’ approach to validation. The CFD solver must be validated for several subsystem cases representing sub-physics for which the data is available. The RSM model has been extensively validated for flows with anisotropic turbulence and streamline curvature (*Lardeau & Manceau, 2016*;

Manceau & Hanjalić, 2002). Hence, the present validation procedure will focus on the validation of the square duct simulation for fully developed turbulent flow.

4.1.2.1 Profiles of the mean and cross stream velocity at different locations.

Figure 4-4 depicts variation of the inner scaling of the mean stream-wise velocity $\overline{U}/u_{\tau}^{*}$ as a function of y/d_{v}^{*} plotted on the logarithmic scale. Here, $d_{v}^{*} = {}^{\nu}/_{u_{\tau}^{*}}$ and $u_{\tau}^{*} = \sqrt{\tau_{w}^{*}/\rho}$, where d_{v}^{*} represents the viscous length scale, u_{τ}^{*} is the friction velocity and τ_{w}^{*} is the surface averaged wall shear stress. Figure 4-4 represents the validation of the law of the wall in this square duct. Profiles of the mean velocity considered at three different wall bisectors show existence of the logarithmic region. Figure 4-4 establishes that in turbulent duct flow there is no 'edge' of the boundary layer, so the outer flow region is the entire flow between the inner flow region and the centerline. The DNS results of Pirozzoli *et al*., (2018) are plotted with the results of the present simulation. It is evident that the velocity profiles in the half width of the duct predicted by the RSM simulation at different locations agrees well with the DNS results.

Figures 4-5 and 4-6 depict the variation of the normalized mean cross stream velocity $\overline{V}/U_{b}$ as a function of the dimensionless length defined as $(y+h)/h$. Similar to the previous case, the profiles of the mean cross stream velocity are considered at three different wall bisectors. Figure 4-5 depicts the profiles closer to the wall at z/D_h = -0.75 and Figure 4-6 depicts the profiles closer to the center of the duct at z/D_h = -0.25. The gradients of the cross stream velocity $\partial\overline{V}/\partial y$ are negative closer to the wall of the duct while they are positive near the center due to the redistribution of the momentum from the core flow in the center towards the corners of the square duct. The DNS results of Pirozzoli *et al*., (2018) are compared with the results of the present RSM simulation. Even though the quality trend of the present simulation is good, there are minor discrepancies in the velocity gradients captured by the RSM simulation as compared to the DNS since the RSM is carried out as a steady state simulation. So, the time averaging is not involved in this case.

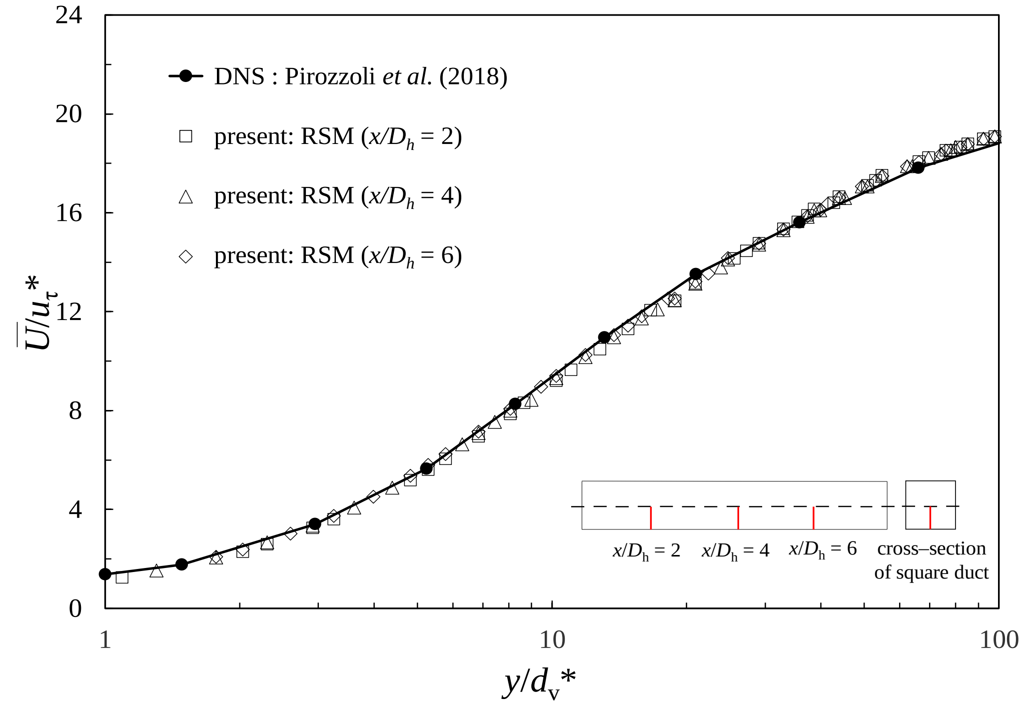

Fig 4-4: Profiles of mean stream-wise velocity along the wall bisector (WB) at $x/D_h = 2$ (squares), $x/D_h = 4$ (triangles), $x/D_h = 6$ (diamonds), and Pirozzoli *et al.* (2018) (solid line circles). Schematic represents the position of the respective profiles.

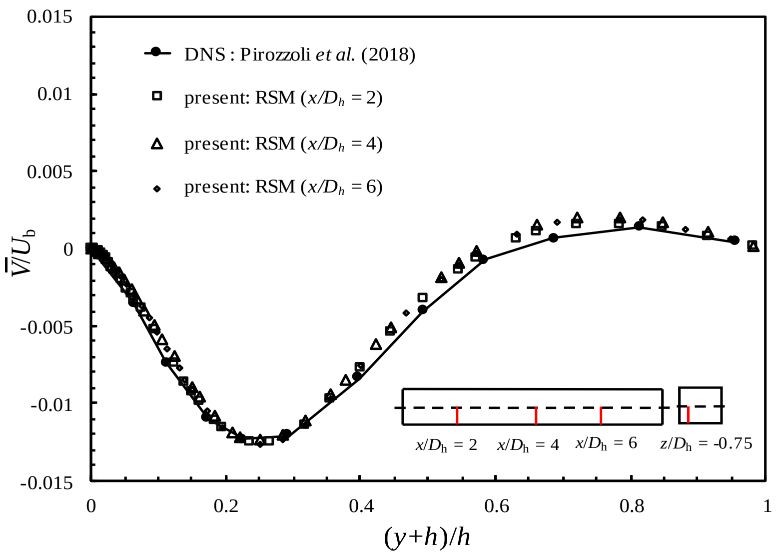

Fig 4-5: Profiles of cross stream velocity at z/D_h = -0.75 for x/D_h = 2 (squares), x/D_h = 4 (triangles), x/D_h = 6 (diamonds), Pirozzoli *et al.* (2018) (solid line circles). Schematic represents the position of the respective profiles.

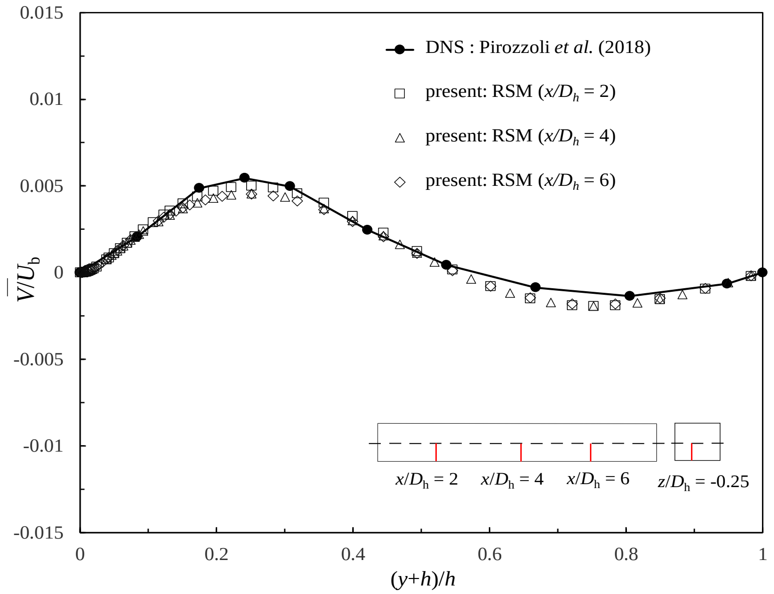

Fig 4-6: Profiles of cross stream velocity at z/D_h = -0.25 for x/D_h = 2 (squares), x/D_h = 4 (triangles), x/D_h = 6 (diamonds), Pirozzoli *et al.* (2018) (solid line circles). Schematic of the duct shows the position of respective profiles.

4.1.2.2 Profiles of local wall shear stress at different locations.

Figure 4-7 shows the variation of the normalized wall shear stress $\tau_w(z)/(\rho U_b^2)$ as a function of z/h. The profiles are considered at three stream-wise locations at *x/D*$_h$ = *2, 4* and *6*. The distribution of the local wall shear stress presents the effect of the secondary motions on the stream-wise velocity field. The behavior observed in the RSM simulation is very similar to what was found in the DNS results of Pirozzoli *et al*., (2018). The maximum values of the wall friction are attained midway between the corner of the duct and the wall bisector. This trend is also qualitatively very similar to the shape as observed in the streamwise velocity profiles.

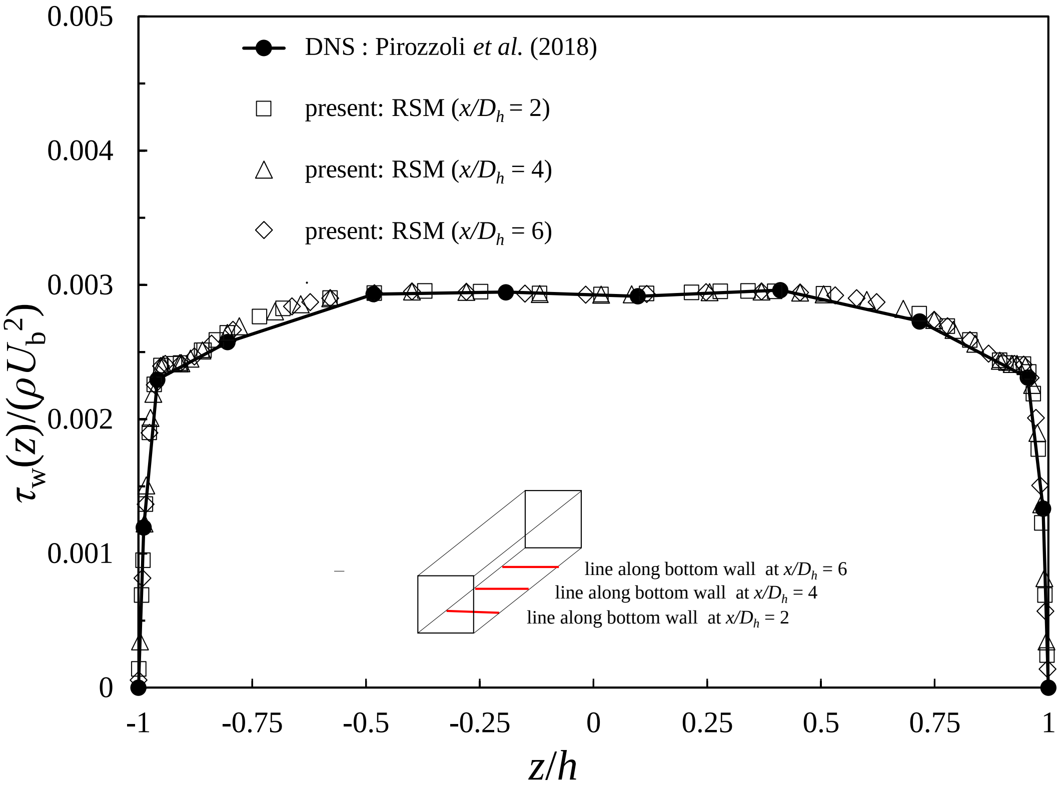

Fig 4-7: Profiles of local wall shear stress along the bottom wall normalized with respect to the bulk dynamic pressure along the bottom wall at x/D_h = 2 (squares), x/D_h = 4 (triangles), x/D_h = 6 (diamonds), Pirozzoli *et al.* (2018) (solid line circles). Schematic represents the position of the respective profiles.

4.1.2.3 Contours of mean velocities and vorticity at different locations.

The steady state RSM simulation is carried out to achieve the fully developed turbulent flow conditions. Contours of velocity and vorticity in the square duct are presented at three different planes in the streamwise direction at x/D_h = 2, 4 and 6.

Figures 4-8(a) and 4-8(b) show contours of the mean stream-wise velocity and the mean cross stream velocity. In Figure 4-8(a), velocity contours protrude towards the corners under the action of the secondary flow. The secondary flows at this Reynolds number are capable of transferring energy from the center to the corners and thus pushing the high velocity zone toward the corner. On the other hand, the layer thickens towards the wall bisector. So, the distortions of the streamwise velocity isolines are observed. Figure 4-8(b) shows the formation of eddies from the corners of the duct due to the imbalance of the momentum between the core and corners of the duct. In both the figures, the contours of $\bar{u}$ and $\bar{v}$ are symmetrical with their distributions averaged over the four quadrants. The similarity of the contours at the different planes of the duct serves as a visual evidence of the fully developed turbulent flow condition.

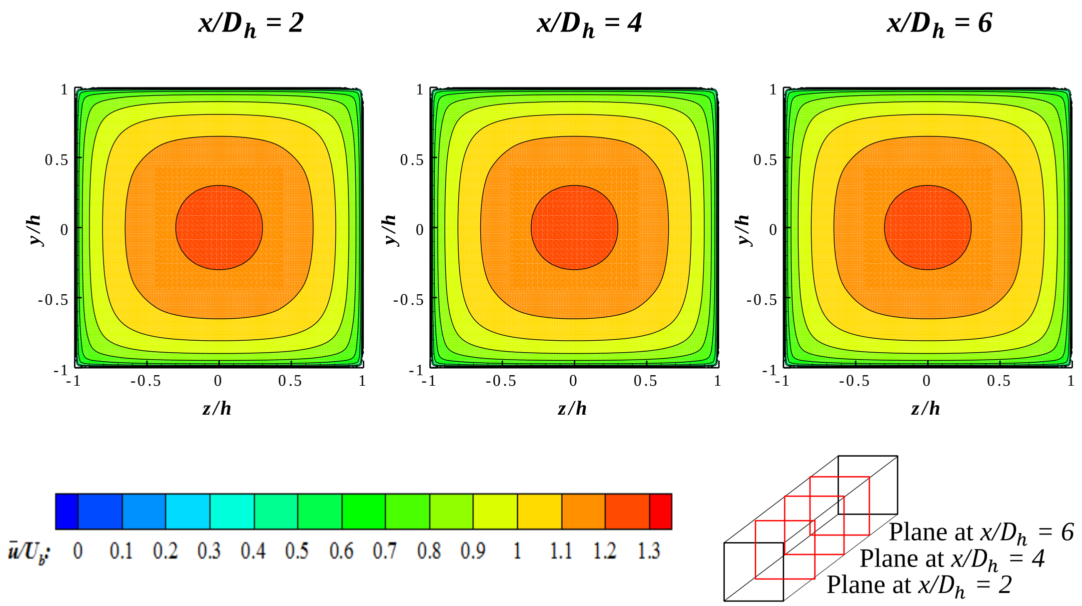

Fig 4-8(a): Contour levels are shown for 0≤ $\overline{U}/U_b$ ≤1.3, in intervals of 0.1 at y-z planes at x/D_h = 2, 4 and 6. Schematic represents the position of the respective profiles.

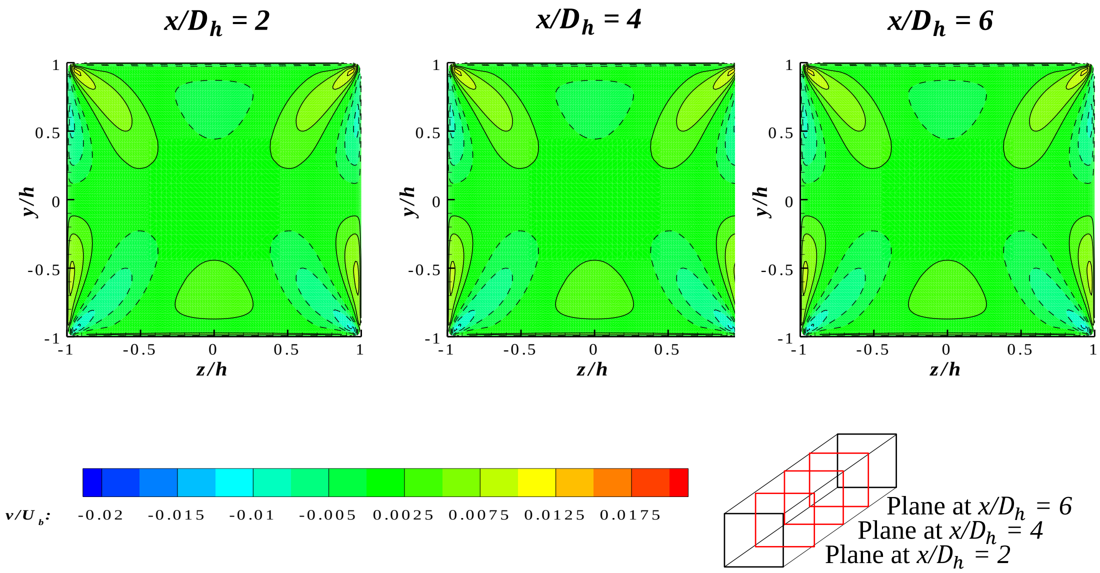

Fig 4-8(b): Contour levels are shown for -0.02 ≤ $\bar{V}/U_b$ ≤ 0.02, in intervals of 0.0025 at y-z planes at x/D_h = 2, 4 and 6. Dashed lines denote negative values. Schematic represents the position of the respective profiles.

Figure 4-9 depicts the structure of the secondary motions in a square duct. The contour levels are shown for the normalized mean streamwise vorticity defined as $\overline{\omega_x}$ = $(\partial\overline{V}/\partial z - \partial\overline{W}/\partial y)$. The secondary motions consist of eight counter rotating eddies originating from the corners of the square duct that are triangular in shape and symmetrical in nature. The primary effect of these eddies is to redistribute the excess momentum from the core towards the corners of the square duct. At the corners of the duct, the momentum is less than the average momentum because of the concurrent friction exerted by the two adjacent walls. The similarity of the contours is observed at three different planes at x/D_h = 2, 4 and 6 which suggests that on average the flow is approaching the fully developed state.

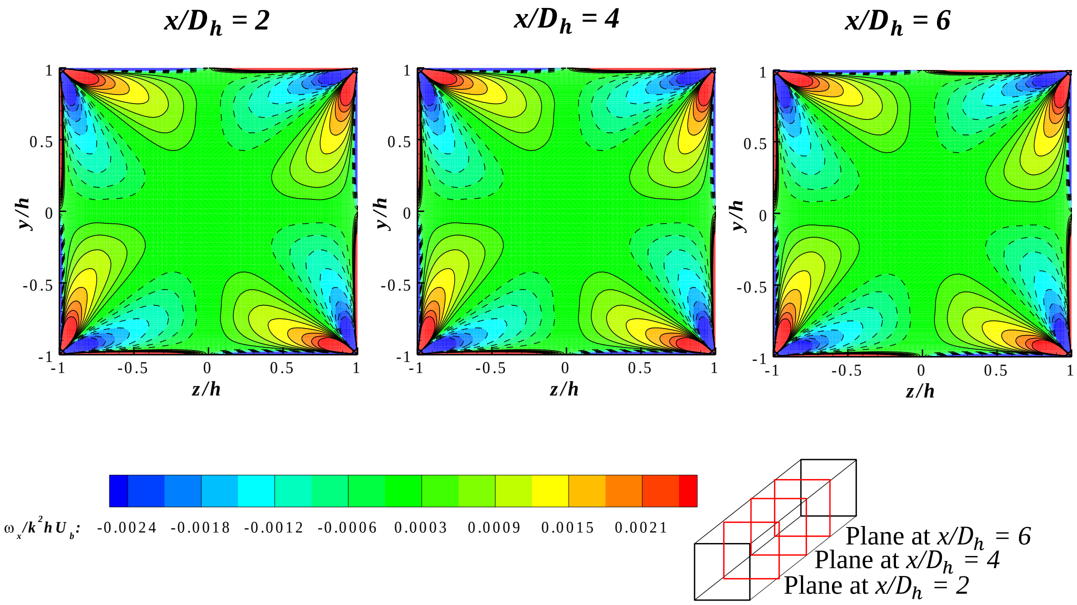

Fig 4-9: Contour levels are shown for -0.0024 $\leq \overline{\omega_x}/(k^2 h U_b) \leq$ 0.0024, in intervals of 0.0003 with k^2 = 49.373/h^2, at y-z planes at x/D_h = 2, 4 and 6. Dashed lines denote negative values. Schematic represents the position of the respective profiles.

4.1.2.4 Square duct simulation at higher Reynolds number (Re = 50,000)

Furthermore, after the validation of the results of this square duct simulation at Re = 40,000, another square duct simulation at higher Reynolds number (Re = 50,000) is carried out and simultaneously the results are validated with the DNS data of *Pirozzoli et al., (2018)* and the previous square duct simulation at Re = 40,000. Figure 4-10 represents that the profiles of mean stream-wise velocity ($\overline{U}$), mean cross stream velocity ($\overline{V}$) and local wall shear stress (τ_w) at x/D_h = 4 are in good agreement with the DNS data of *Pirozzoli et al., (2018)* and overlap the previous square duct simulation at Re = 40,000. This suggests that the fluid properties are mostly unaffected by the variation at higher Reynolds number. *Pirozzoli et al., (2018)* also stated that the turbulent intensity of the secondary motions is mostly unaffected by the Reynolds number variation and they do not have a large influence on the bulk flow properties. As the numerical strategy for the two-pass channel requires a fully developed turbulent inlet condition, the mean velocities, turbulent dissipation rate and the Reynolds stresses from this square duct simulation at Re = 50,000 are mapped at the inlet of the two-pass channel.

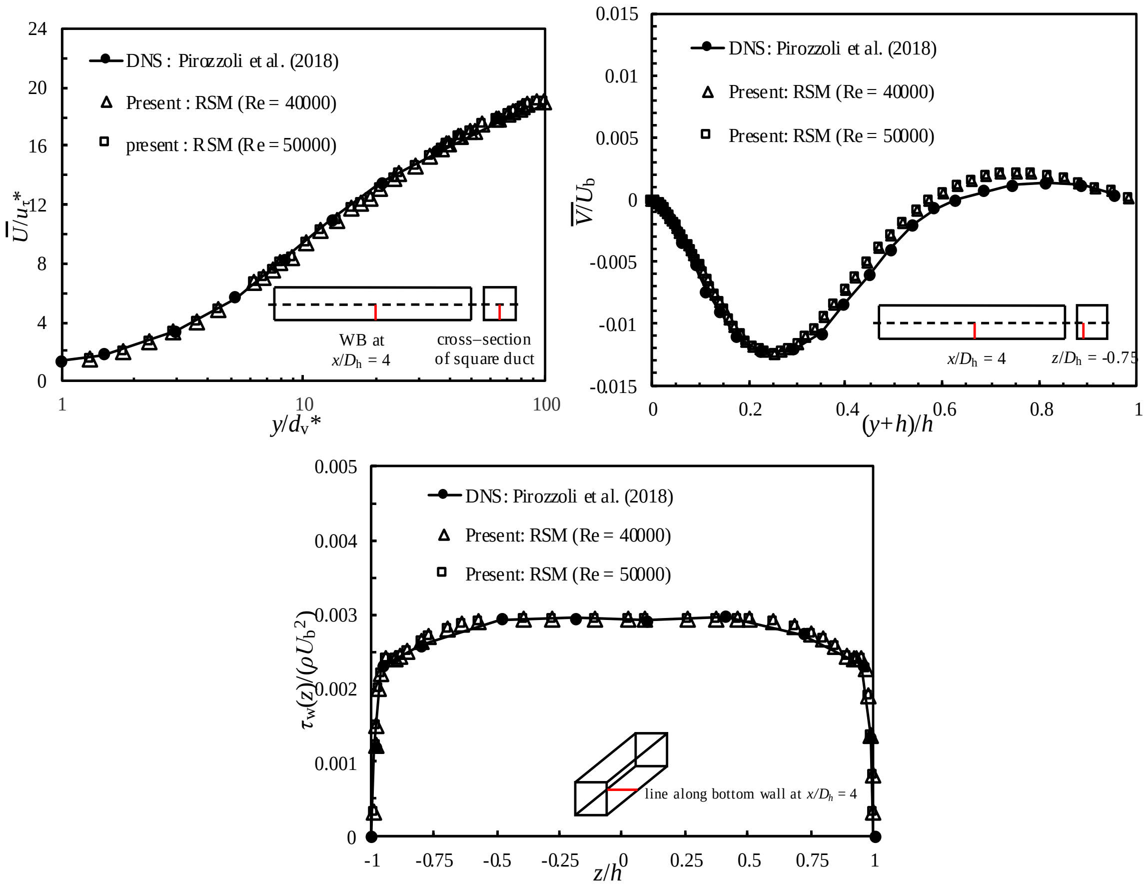

Fig 4-10: Profiles of mean stream-wise velocity ($\overline{U}$), mean cross stream velocity ($\overline{V}$) and local wall shear stress (τ_w) at x/D_h = 4 for *Pirozzoli et al. (2018)* (solid line circles), RSM at Re = 40,000 (triangles) and RSM at Re = 50,000 (squares). Schematic represents the position of the respective profiles.

4.2 Two-pass channel simulation

This simulation is performed at a Reynolds number of 50,000. It is conducted in the transient state and aimed at the investigation of the mean flow and turbulence properties, and understanding the flow behavior before the bend, in the bend and after the bend.

4.2.1. Grid Independence study

(a) Before the bend

The grid independence study is carried out with 4 different hexahedral mesh configurations, with 2×10^6, 4×10^6, 8×10^6 and 11×10^6 cells. The trimmer mesh feature in STAR-CCM+ is used for the generation of these meshes. Figures 4-11(a) and 4-11(b) depict comparison of the mean flow ($\overline{U}, \overline{V}$ and $\overline{W}$) and turbulence (*u', v'*, *w'* and *k*) parameters extracted before the bend at x/D_h = 0.5 for all mesh configurations. It is noted that the mesh with 2×10^6 cells consistently deviates from the other three configurations. Subsequently, the results of the meshes with 4 x 10^6 cells, 8 x 10^6 cells and 11 x 10^6 cells provide an excellent collapse for the mean flow and turbulence parameters, measured at the same locations before the bend.

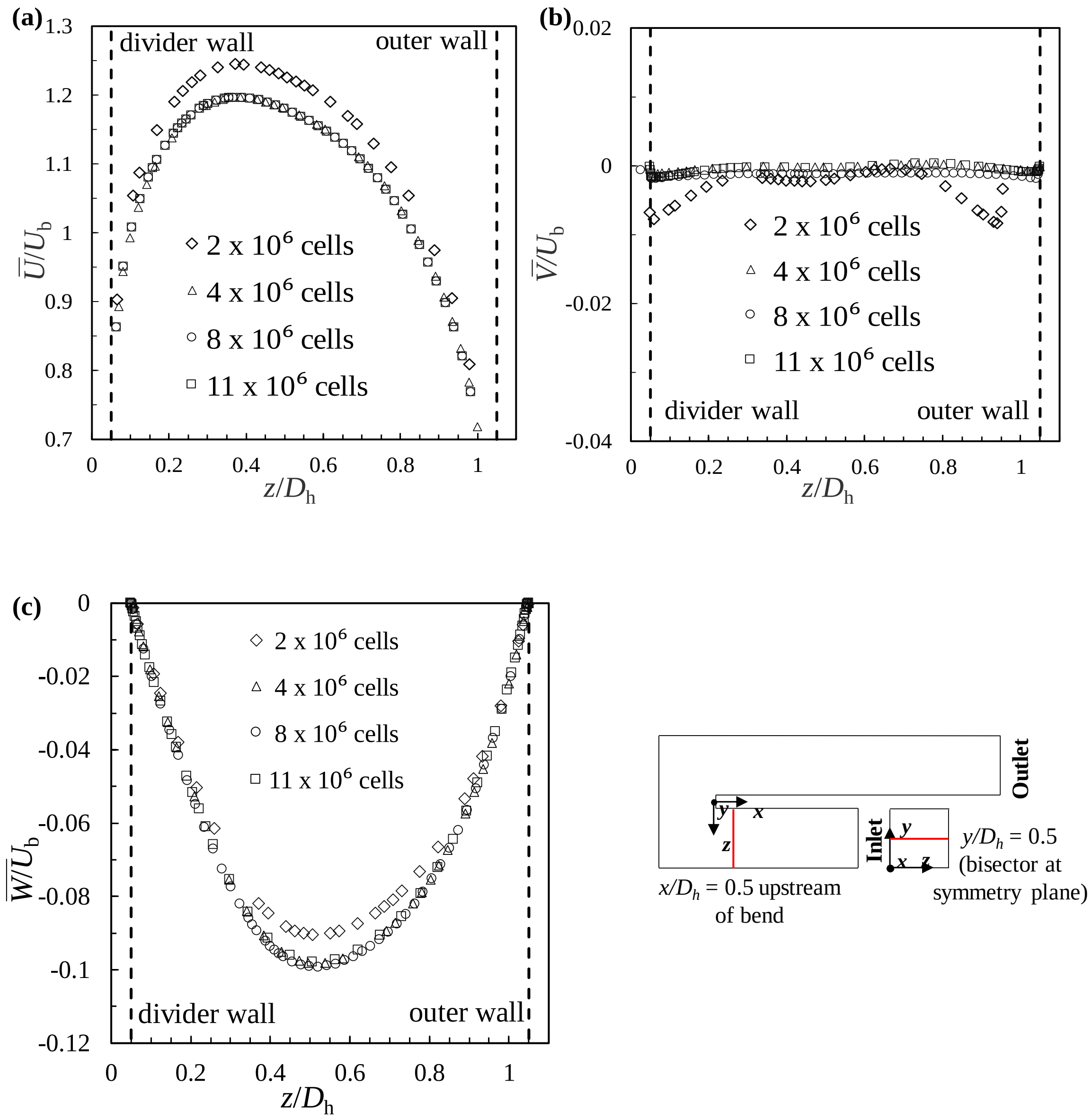

Fig 4-11(a): Comparison of different meshes of two-pass channel for profiles of mean flow properties ($\overline{U}, \overline{V}$ and $\overline{W}$) at bisector along the symmetry plane (at y/D_h = 0.5) at x/D_h = 0.5 upstream of the bend. Schematic represents the position of the respective profiles.

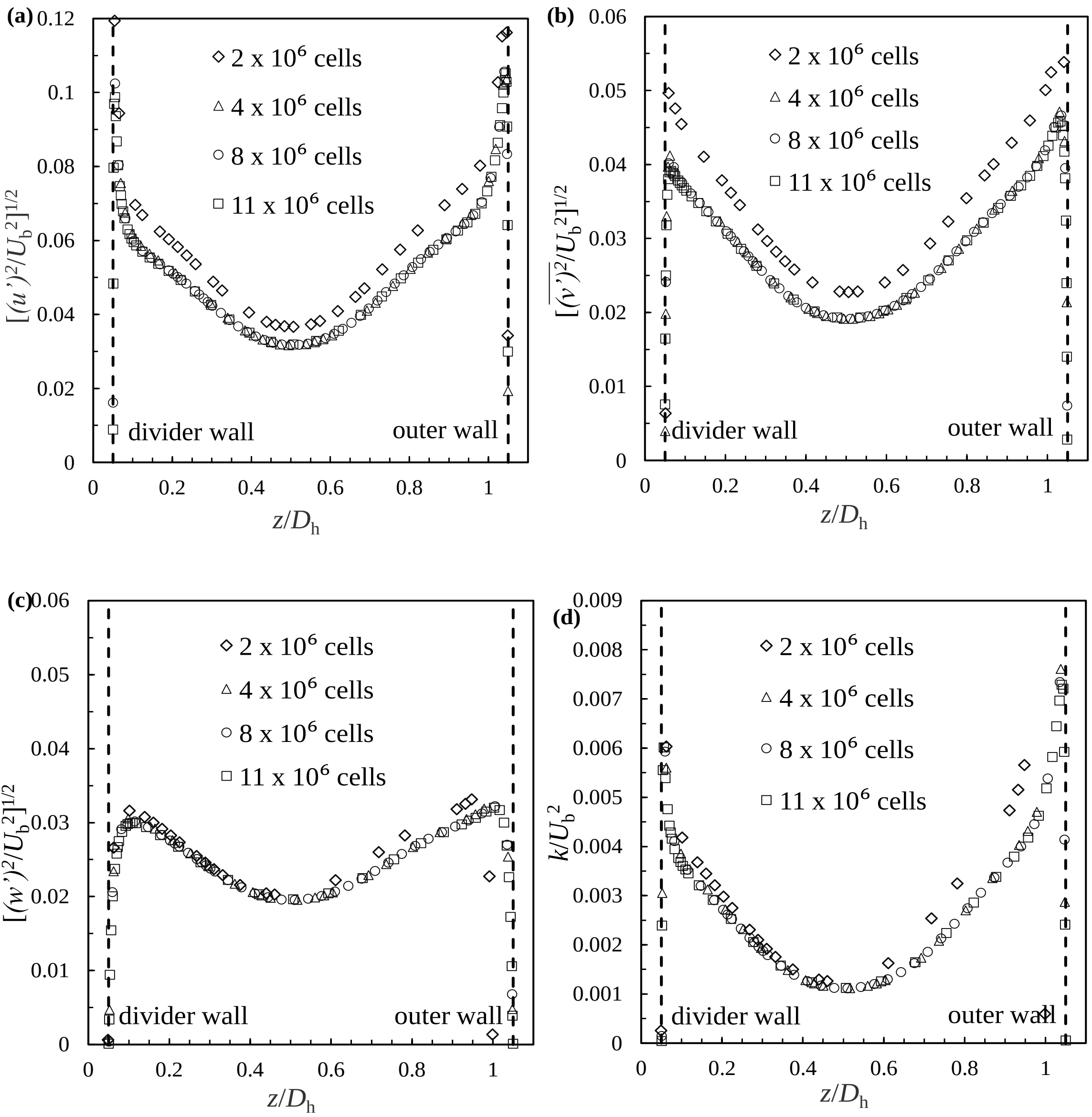

Fig 4-11(b): Comparison of different meshes of two-pass channel for profiles of turbulence parameters (*u', v', w' and k*). The profiles are shown at the same position as in Fig 4-11.

(b) In the bend and after the bend

Figures 4-12(a), (b), (c) and (d) present the comparison of the mean velocity ($\overline{U}$), stream-wise fluctuating velocity (u') and wall shear stress (τ_w) for all the mesh configurations. The meshes are checked and compared at different critical locations in the two-pass channel such as 90-degree plane in the bend, and at x/D_h = 0.25, 1.60 and 10 after the bend. At all these locations, the mesh with 2×10^6 cells consistently deviate from the other three configurations suggesting that the numerical solution is grid dependent. The results of the mesh configuration with 4 x 10^6 cells is aligned with 8 x 10^6 cells and 11 x 10^6 cells while the meshes with 8 x 10^6 cells and 11 x 10^6 cells provide an excellent collapse for the mean and turbulent velocities, as well as the wall shear stress. Thus, after careful observation of the variations in the distributions of these mesh configurations, it is established that the mesh with 4 × 10^6 cells is the best compromise for the accuracy of the results.

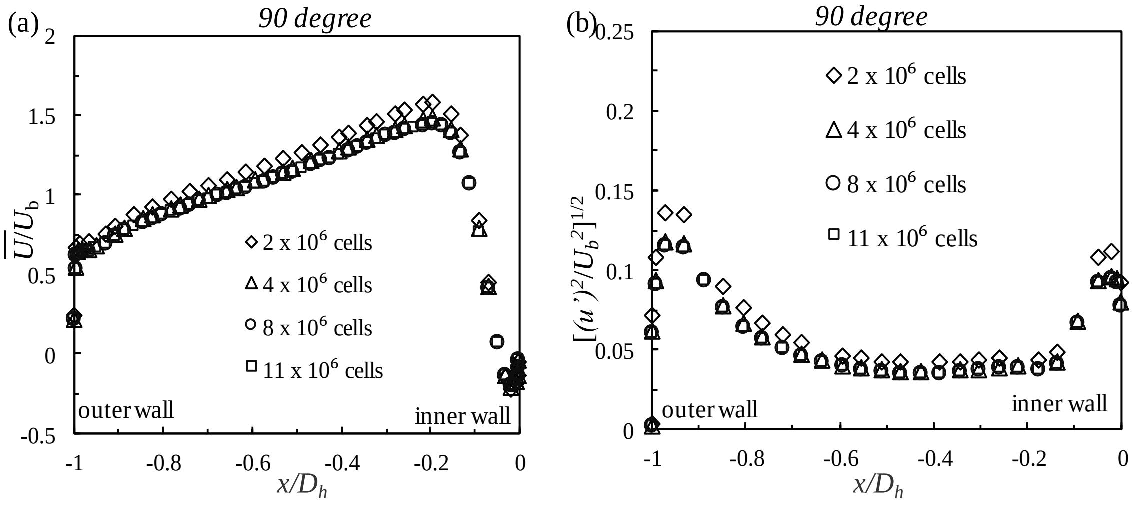

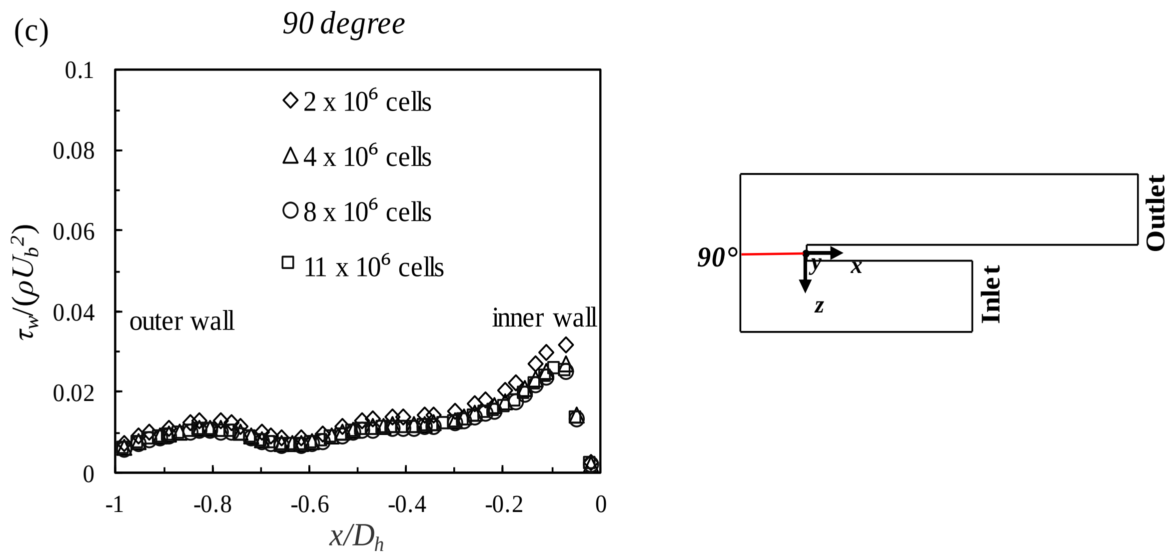

Fig 4-12(a): Comparison of different meshes of two-pass channel for profiles of mean velocity ($\overline{U}$), stream-wise fluctuating velocity (u') and wall shear stress (τ_w) at 90-degree plane in the bend. Schematic represents the position of the respective profiles.

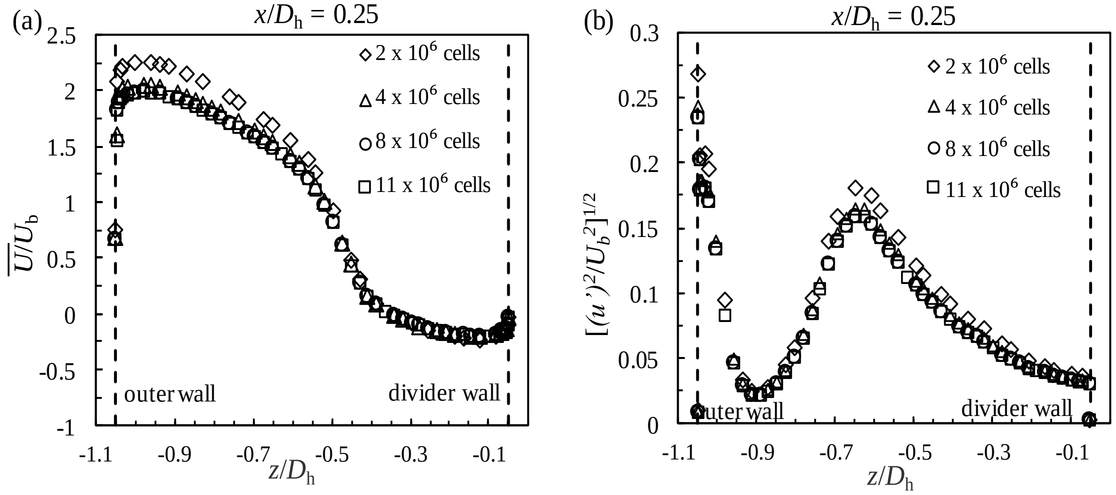

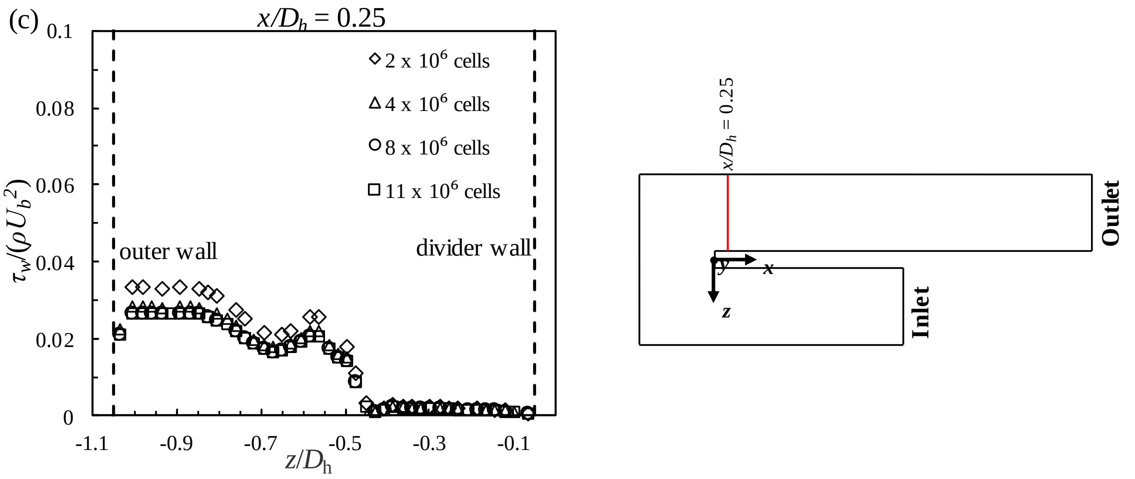

Fig 4-12(b): Comparison of different meshes for profiles of mean velocity ($\overline{U}$), stream-wise fluctuating velocity (u') and wall shear stress (τ_w) at x/D_h = 0.25 after the bend.

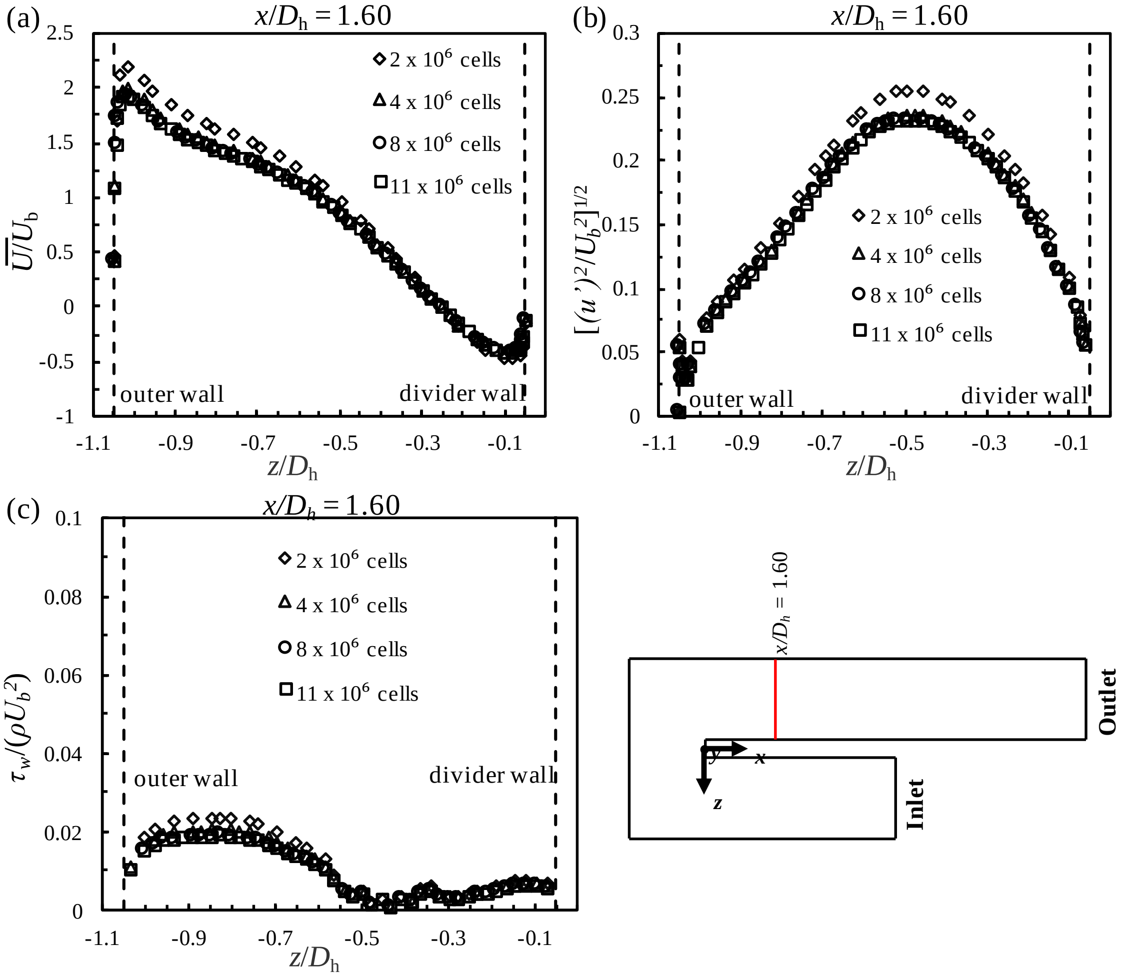

Fig 4-12(c): Comparison of different meshes for profiles of mean velocity ($\overline{U}$), stream-wise fluctuating velocity (u') and wall shear stress (τ_w) at x/D_h = 1.60 after the bend.

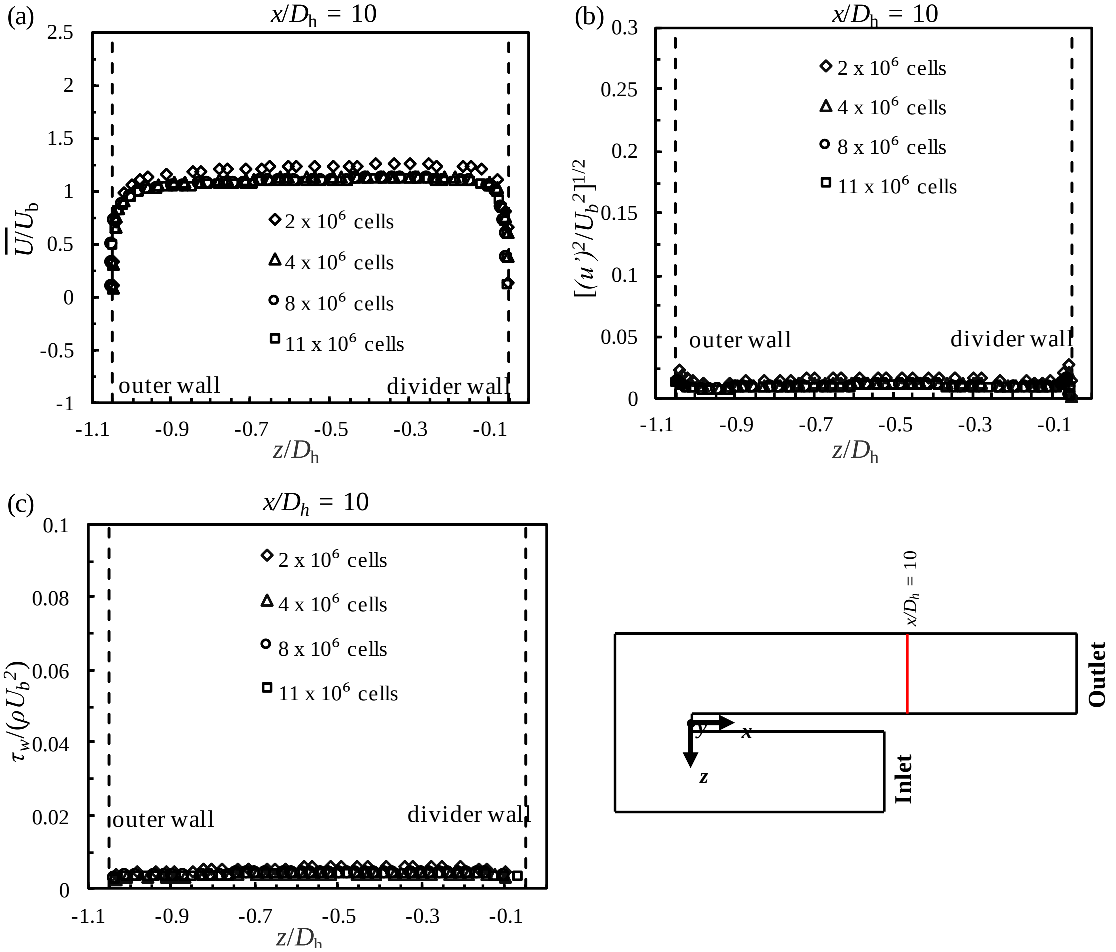

Fig 4-12(d): Comparison of different meshes for profiles of mean velocity ($\overline{U}$), stream-wise fluctuating velocity (u') and wall shear stress (τ_w) at x/D_h = 10 after the bend.

4.2.2 Validation of the flow characteristics in a two-pass channel

The most important part of the study is the validation of the results by comparing it with the previous work available in the literature**.** As mentioned previously, the RSM model has been extensively validated for flows with anisotropic turbulence and streamline curvature (Lardeau & Manceau, 2016), (Manceau & Hanjalić, 2002). The present validation procedure will focus on the validation of the two-pass channel simulation by comparing it with the PIV experiments of the previous study performed by *Schabacker et* al., (1998). Here, the methodology adopted for the validation is systematically divided into three stages based on the flow characteristics as before the bend, in the bend and after the bend.

4.2.2.1 Flow characteristics before the bend.

Figure 4-13 depicts the comparison of mean velocity profiles of the present RSM simulation with the PIV data of *Schabacker et al., (1998)*. The profile of the mean streamwise velocity, $\overline{U}/U_b$ as shown in Figure 4-13(a) agrees well with the data of *Schabacker et al., (1998)*. At this location (x/D_h = 0.5), the flow deviates from the flow in a straight duct. The flow with higher velocity is shifted towards the divider wall and thus the mean velocity shows asymmetric distribution. The profile of the vertical velocity component, $\overline{V}/U_b$, is flat and the present RSM simulations slightly overpredict the magnitude. The mean vertical component is closed to zero and the profile is somewhat more symmetrical. This shows that the influence of the turn on the flow begins to appear well before the turn. The streamline curvature of the velocity profile is shown in the cross stream velocity component, $\overline{W}/U_b$. It reaches the maximum at the centre of the upstream channel. The present RSM profiles are in good agreement with the PIV results of *Schabacker et al. (1998)*.

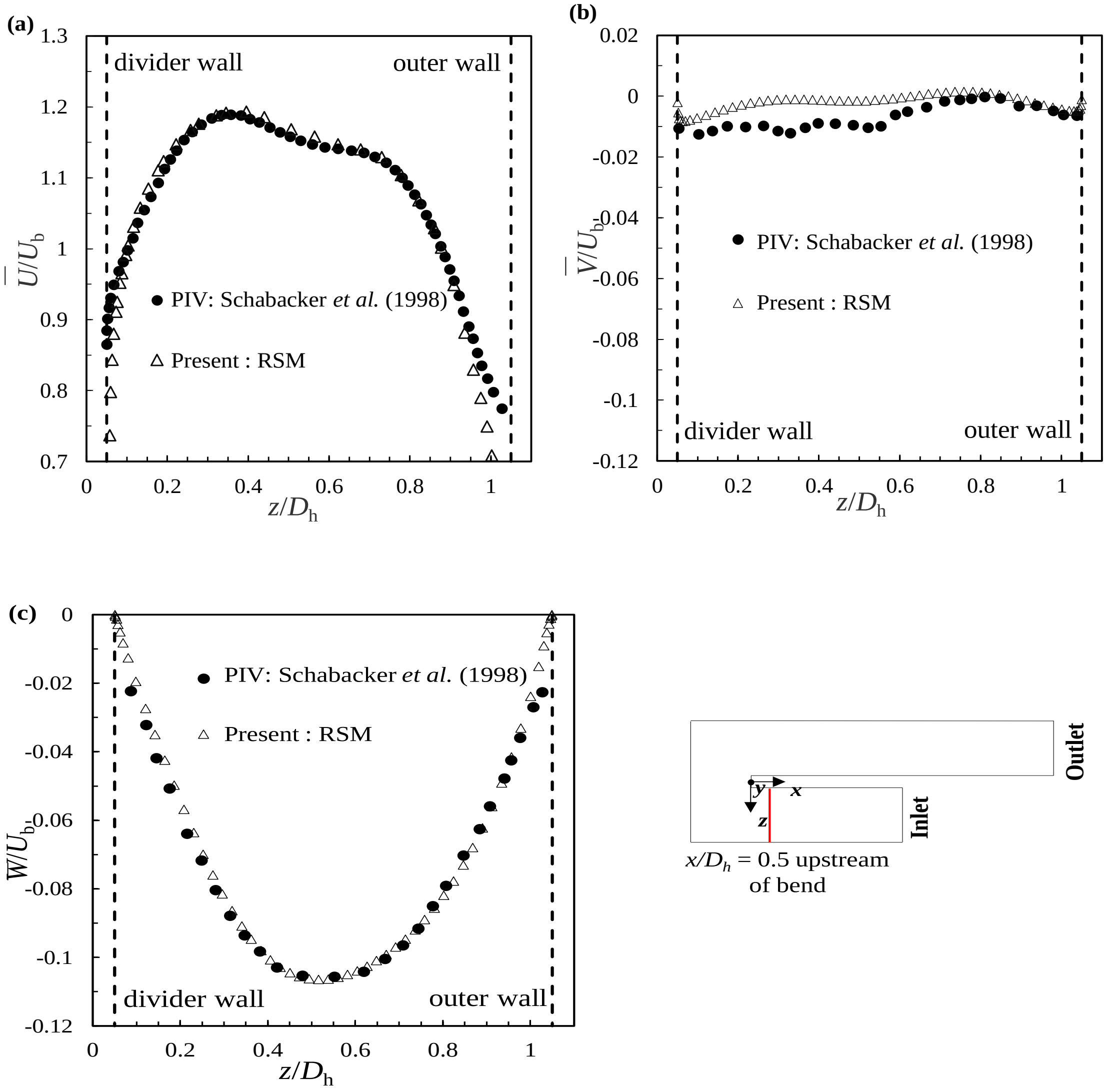

Fig 4-13: Profiles of mean velocity components ($\overline{U}, \overline{V}$ and $\overline{W}$) at bisector along the symmetry plane (at $y/D_h = 0.5$) at $x/D_h = 0.5$ upstream of the bend for PIV: Schabacker *et al*. (circles) and RSM (triangles). Schematic represents the position of the respective profiles.

Figures 4-14(a), (b), (c) and (d) present the profiles of the turbulence parameters $(u', v', w' \; and \; k)$ as a function of z$/D_h$ before the bend entrance. The profiles of the fluctuating velocity components (u', v', w') depict that the turbulence induced in the flow is maximum near the walls and minimum in the center of the channel. The profiles of k/U_b^2 show that turbulent kinetic energy is maximum near the divider wall where a strong flow acceleration takes place due to the effect of the sharp bend. This is caused by the influence of the pressure gradient near the turn that is favorable in the divider wall side. The RSM values for the components, u' and v', obtained from the present simulation and PIV data are in good agreement. However, there is a mismatch for the w' RMS values at the center of the channel. This discrepancy is also observed in the k/U_b^2 profiles of the current RSM simulation. Since the stereoscopic PIV technique is used by the *Schabacker et al., (1998)* it is possible that this deviation might be due to the inaccurate determination of w' due to the increase of the uncertainty in the measurements of the out of plane component of the velocity.

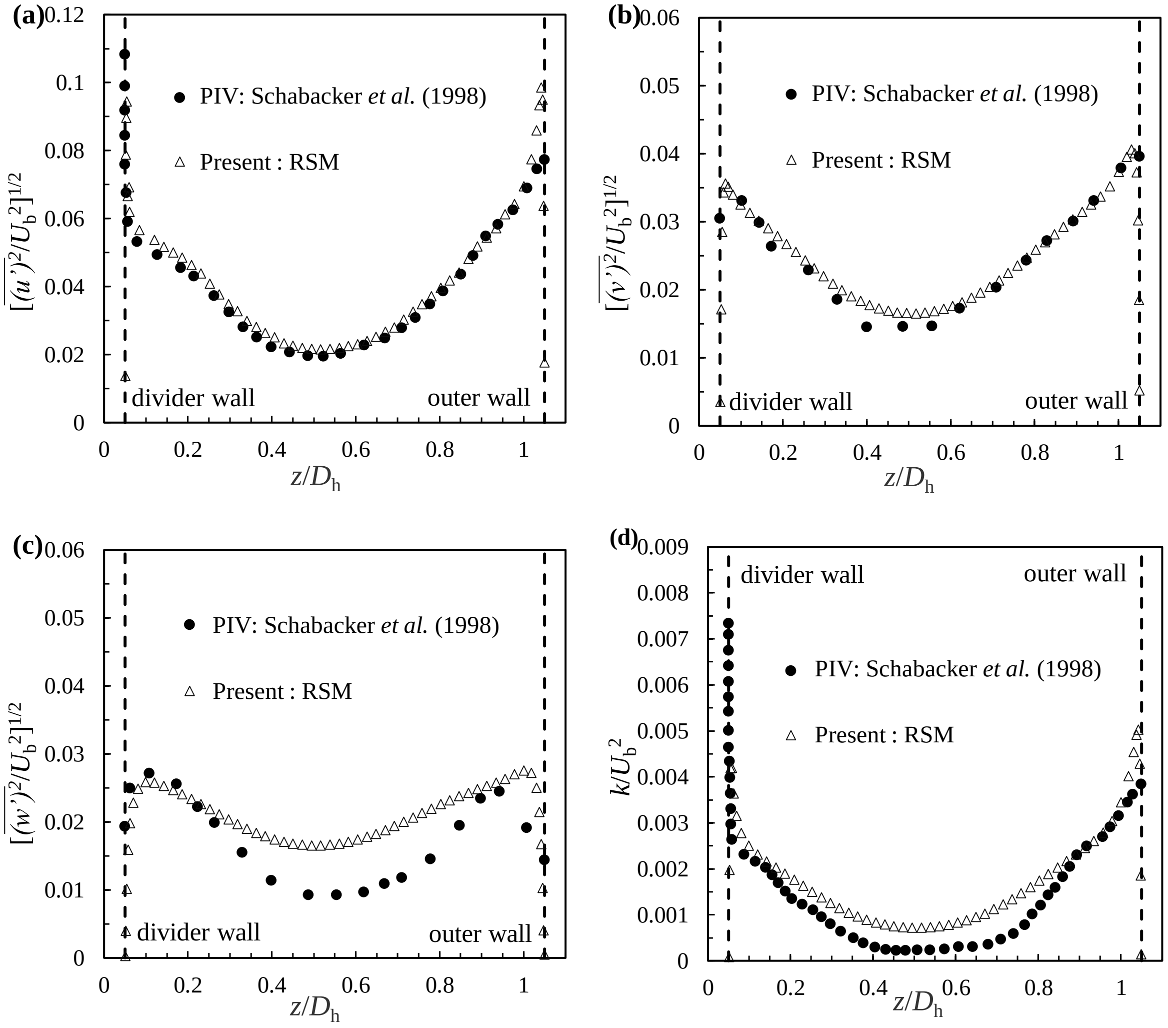

Fig 4-14: Profiles of turbulence parameters (u', v', w' and k) for PIV: Schabacker *et al.* (circles) and RSM (triangles) The profiles are shown at the same position as in Fig 4-13.

4.2.2.2 Flow characteristics in the bend.

(a) Mean stream-wise velocity ($\overline{U}$)

Figures 4-15(a), (b), (c) and (d) show the stream-wise velocity ($\overline{U}$) profiles at different planes in the bend at different angles. The *proj* distance is defined as:

proj projected distance in the bend = $\frac{\sqrt{x^2+z^2}}{S}|\cos\alpha|$ for $\alpha \leq 45°$ and $\alpha > 135°$

$\frac{\sqrt{x^2+z^2}}{S}|\sin\alpha|$ for $45° < \alpha \leq 135°$

where, α - Section angle in the bend

S - Section length in the bend at 90° section, $S/D_h = 1$

As the flow progresses through the bend, the favorable pressure gradient causes the stream-wise velocity to increase near the divider wall in the bend entrance, as it is observed in both 22.5° and 45° planes. The RSM and PIV data collapses well in these planes. Between planes 45° and 90°, the development of the secondary motion takes place that advances the flow towards the outer wall. At the 90° plane section, the profile of $\overline{U}/U_b$ obtained from the RSM simulation matches well with the PIV experiment except that the peak values are different. With the development of the flow in the downstream region, the pressure field changes and the fast-moving fluid flows towards the outer wall whereas the flow with low velocity accumulates near the divider wall. Planes 135° and 157.5° depict this observation. Both the experimental and simulation profiles follow the similar trend in these locations.

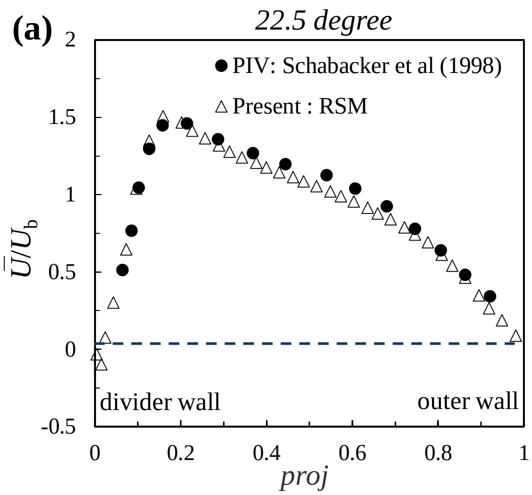
(a)
22.5 degree
● PIV: Schabacker et al (1998)
△ Present : RSM
$\bar{U}/U_b$
2
1.5
1
0.5
0
-0.5
divider wall
outer wall
0
0.2
0.4
0.6
0.8
1
proj

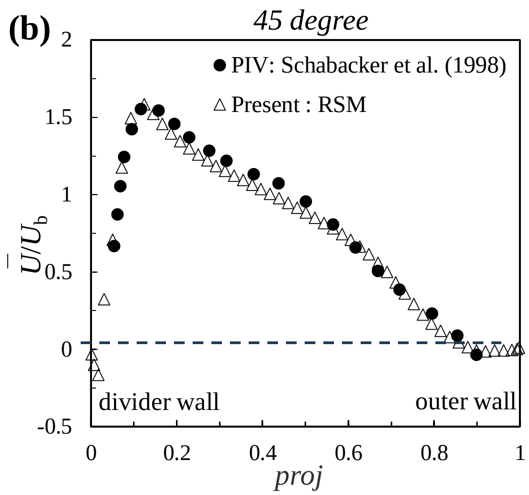
(b)
45 degree
● PIV: Schabacker et al. (1998)
△ Present : RSM
$\bar{U}/U_b$
2
1.5
1
0.5
0
-0.5
divider wall
outer wall
0
0.2
0.4
0.6
0.8
1
proj

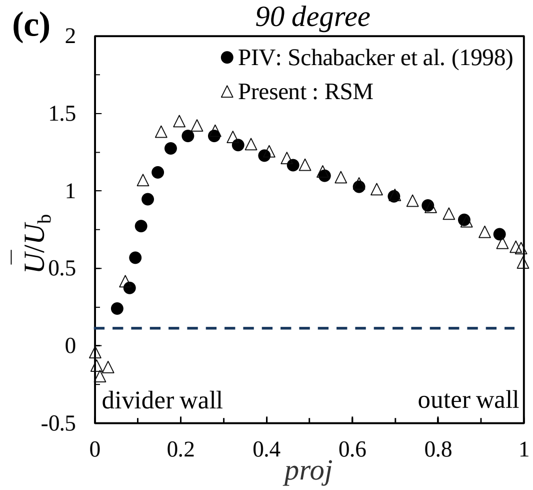
(c)
90 degree
● PIV: Schabacker et al. (1998)
△ Present : RSM
$\bar{U}/U_b$
2
1.5
1
0.5
0
-0.5
divider wall
outer wall
0
0.2
0.4
0.6
0.8
1
proj

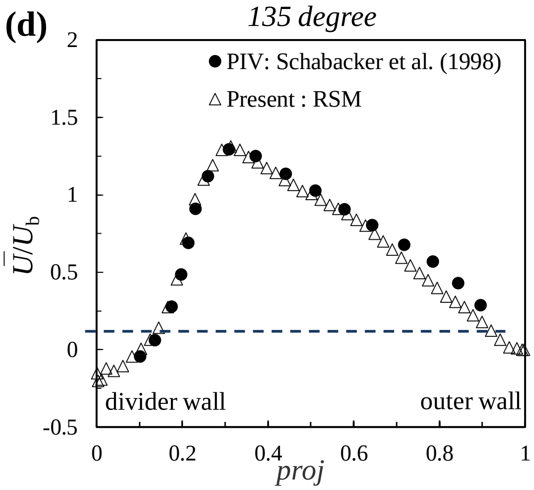
(d)
135 degree
● PIV: Schabacker et al. (1998)
△ Present : RSM
$\bar{U}/U_b$
2
1.5
1
0.5
0
-0.5
divider wall
outer wall
0
0.2
0.4
0.6
0.8
1
proj

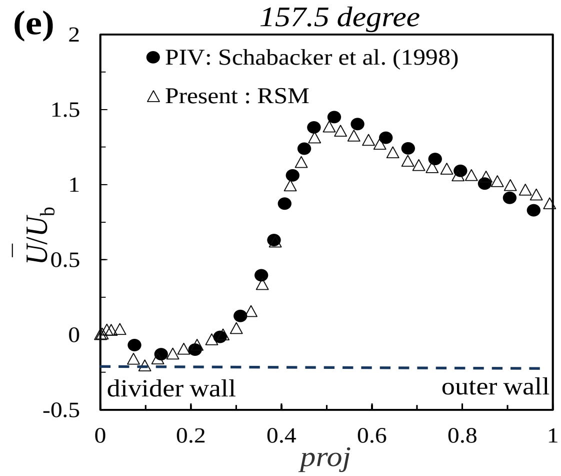
(e)
157.5 degree
● PIV: Schabacker et al. (1998)
△ Present : RSM
$\bar{U}/U_b$
2
1.5
1
0.5
0
-0.5
divider wall
outer wall
0
0.2
0.4
0.6
0.8
1
proj

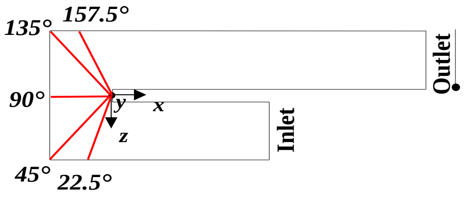
135°
157.5°
90°
45°
22.5°
y
x
z
Outlet
Inlet

Fig 4-15: Profiles of streamwise velocity $(\overline{U})$ along the symmetry plane ($y/D_h = 0.5$) at (a) 22.5 degree, (b) 45 degree, (c) 90 degree, (d) 135 degree and (e) 157.5 degree in the bend for PIV: Schabacker *et al*. (circles) and RSM simulations (triangles). Schematic represents the locations of the respective profiles.

(b) Streamwise turbulence (*u'*)

Figures 4-16 (a), (b), (c) and (d) represent the profiles of the stream-wise fluctuating velocity (u'/U_b) at various angular planes in the bend. With the development of the flow towards the first half of the bend (90° section plane), it takes the shape of a concave type curvature near the outer wall and a recirculation zone also appears in the upstream corner of the channel. These effects contribute to the increase of the flow turbulence towards the outer wall. The RSM profiles match qualitatively with the PIV for the 22.5°, 45° and 90° planes. In the second half of the bend, a strong secondary flow develops, and the flow separation takes place near the divider wall. This further results in the strong stream-wise flow acceleration near the divider wall. Thus, there is an increase in the stream-wise turbulence on the divider wall side and a subsequent decrease towards the outer wall side. The profiles of RSM and PIV data are in qualitative agreement for these planes near the bend exit.

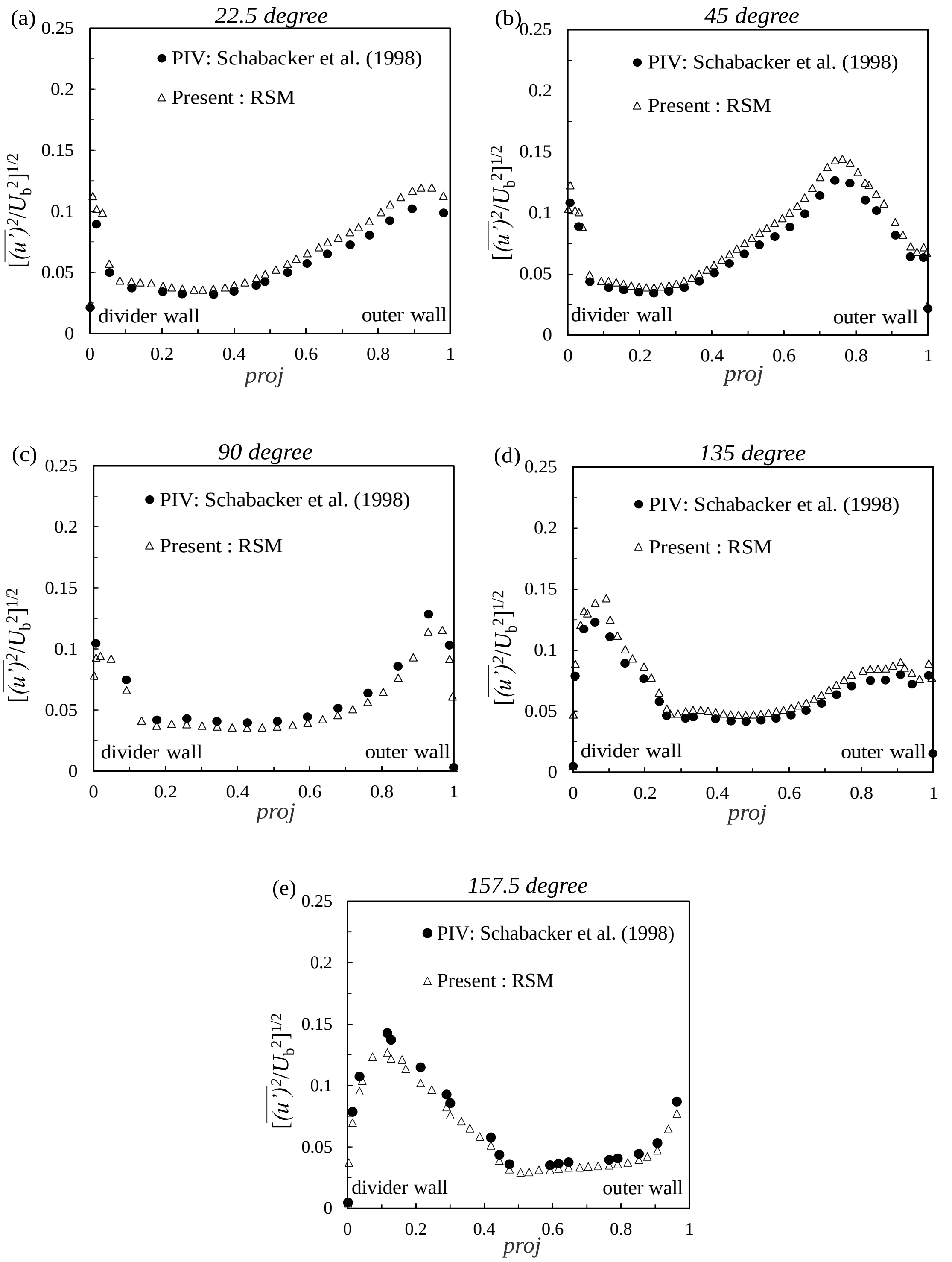

Fig 4-16: Profiles of stream-wise fluctuating velocity *(u')* for PIV: Schabacker *et al.* (circles) and RSM simulations (triangles). The profiles are shown at the same position as in Fig 4-15.

4.2.2.3 Flow characteristics after the bend

(a) Mean stream-wise velocity ($\overline{U}$)

Figure 4-17 depicts the profiles of the mean stream-wise velocity ($\overline{U}/U_b$) at 8 different locations after the bend. At the bend exit (x/D_h = 0), the flow undergoes a strong acceleration at the outer wall because of the secondary flow that transports fluid into this region. Near the divider wall, the stream-wise velocity is in the reversed direction. The extent of the negative velocity in the z-direction indicates the height of the separation bubble formed at the divider wall. At x/D_h = 0.25, the separation bubble in the symmetry plane has grown to approximately 35-40% of the height of the downstream channel. The separation bubble grows further with the development of the flow. The flow reattaches at x/D_h = 2.12 in the PIV experiment by Schabacker et al. (1998) and the present RSM simulation. The profiles of the PIV experiments and the RSM simulation before the reattachment are in agreement. Hereafter, the redevelopment of the boundary layer starts. As the distance from the bend exit increases, the flow starts decelerating very rapidly. At x/D_h = 3 and x/D_h = 4.2, the velocity profiles are asymmetrical and at x/D_h = 10, the flow characteristics are approaching towards the symmetrical structure.

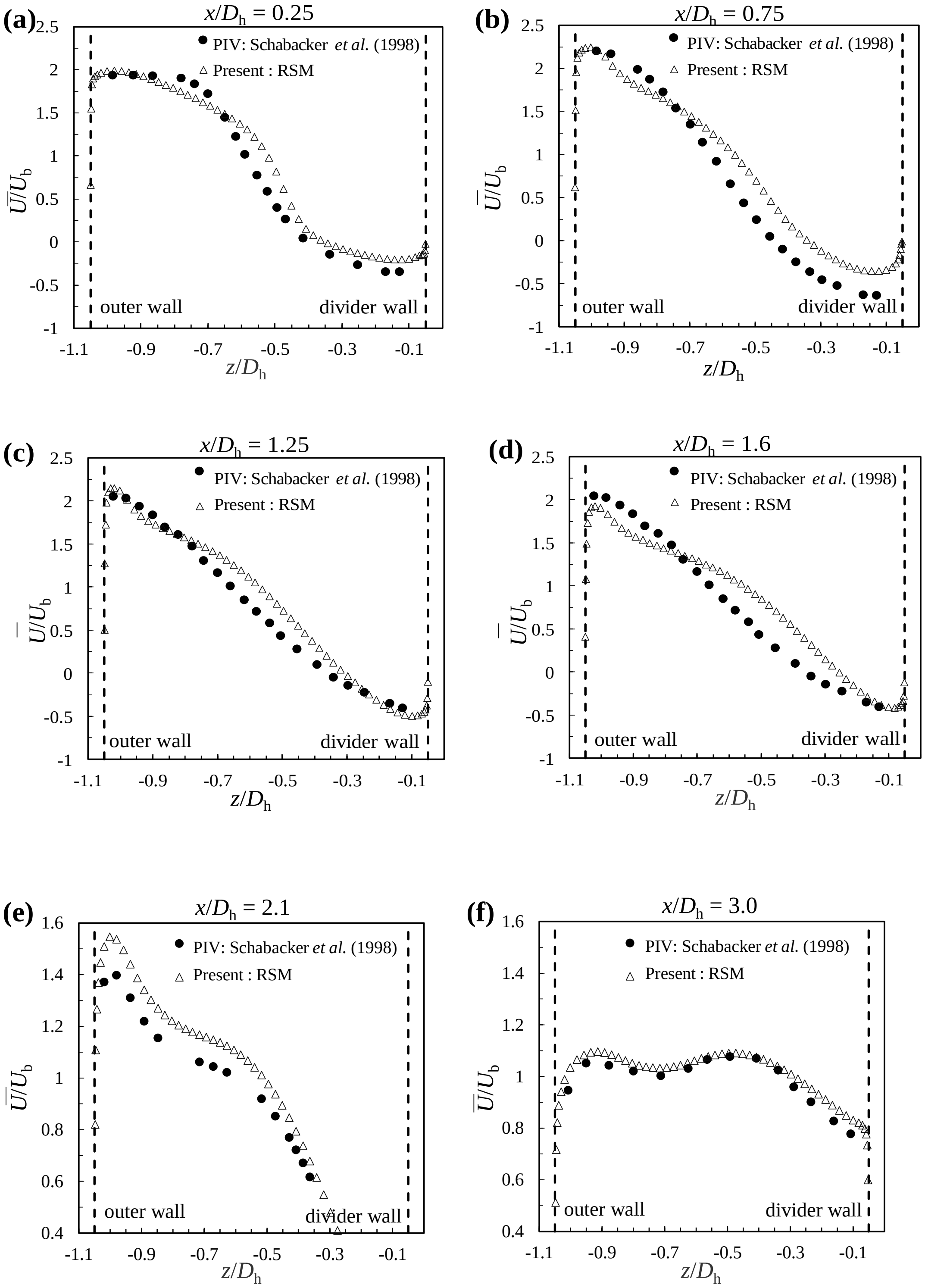
(a)
x/Dh = 0.25
PIV: Schabacker et al. (1998)
Present : RSM
outer wall
divider wall
U/Ub
z/Dh
2.5
2
1.5
1
0.5
0
-0.5
-1
-1.1
-0.9
-0.7
-0.5
-0.3
-0.1
(b)
x/Dh = 0.75
PIV: Schabacker et al. (1998)
Present : RSM
outer wall
divider wall
U/Ub
z/Dh
(c)
x/Dh = 1.25
PIV: Schabacker et al. (1998)
Present : RSM
outer wall
divider wall
U/Ub
z/Dh
(d)
x/Dh = 1.6
PIV: Schabacker et al. (1998)
Present : RSM
outer wall
divider wall
U/Ub
z/Dh
(e)
x/Dh = 2.1
PIV: Schabacker et al. (1998)
Present : RSM
outer wall
divider wall
U/Ub
z/Dh
1.6
1.4
1.2
1
0.8
0.6
0.4
(f)
x/Dh = 3.0
PIV: Schabacker et al. (1998)
Present : RSM
outer wall
divider wall
U/Ub
z/Dh

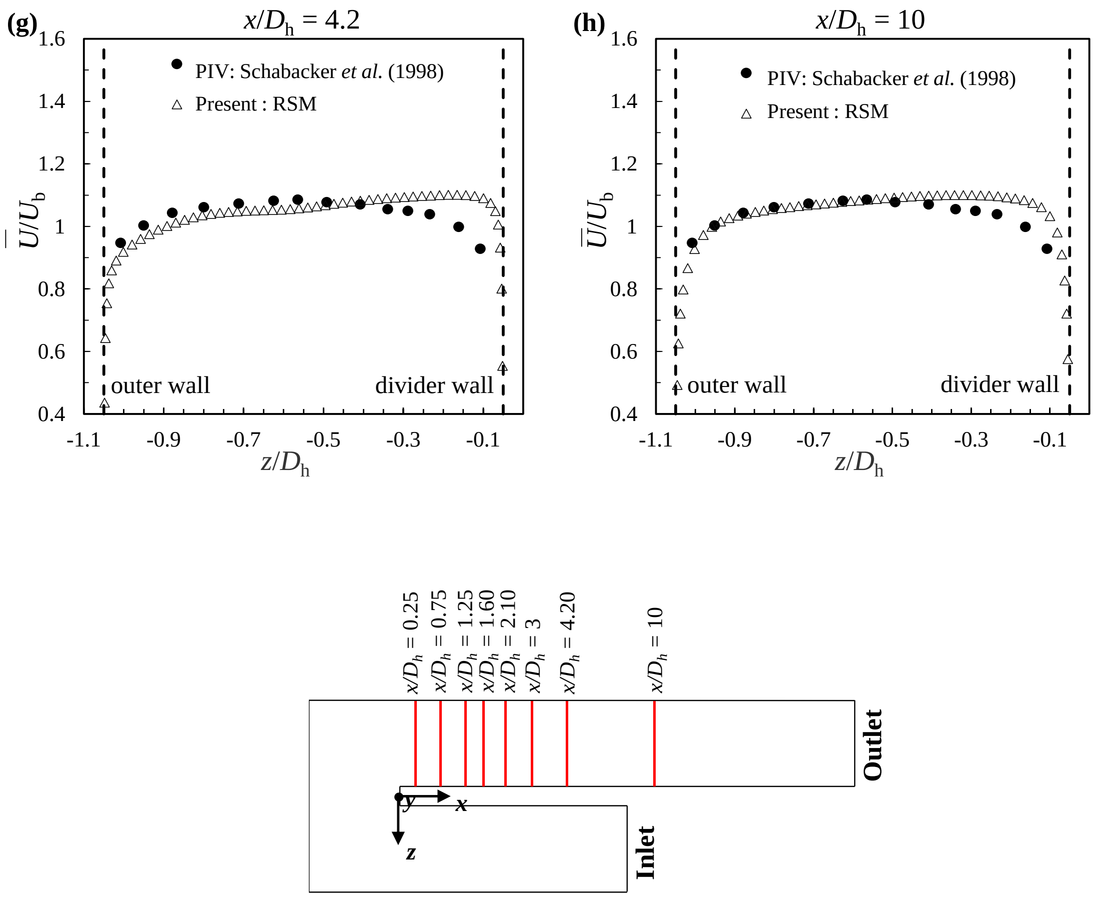

Fig 4-17: Profiles of mean stream-wise velocity $(\overline{U})$ at different locations along the symmetry plane (y/D_h = 0.5) downstream of the bend for PIV: Schabacker *et al*. (circles) and RSM (triangles) Schematic represents the locations of the respective profiles.

(b) Turbulent kinetic energy (*k*)

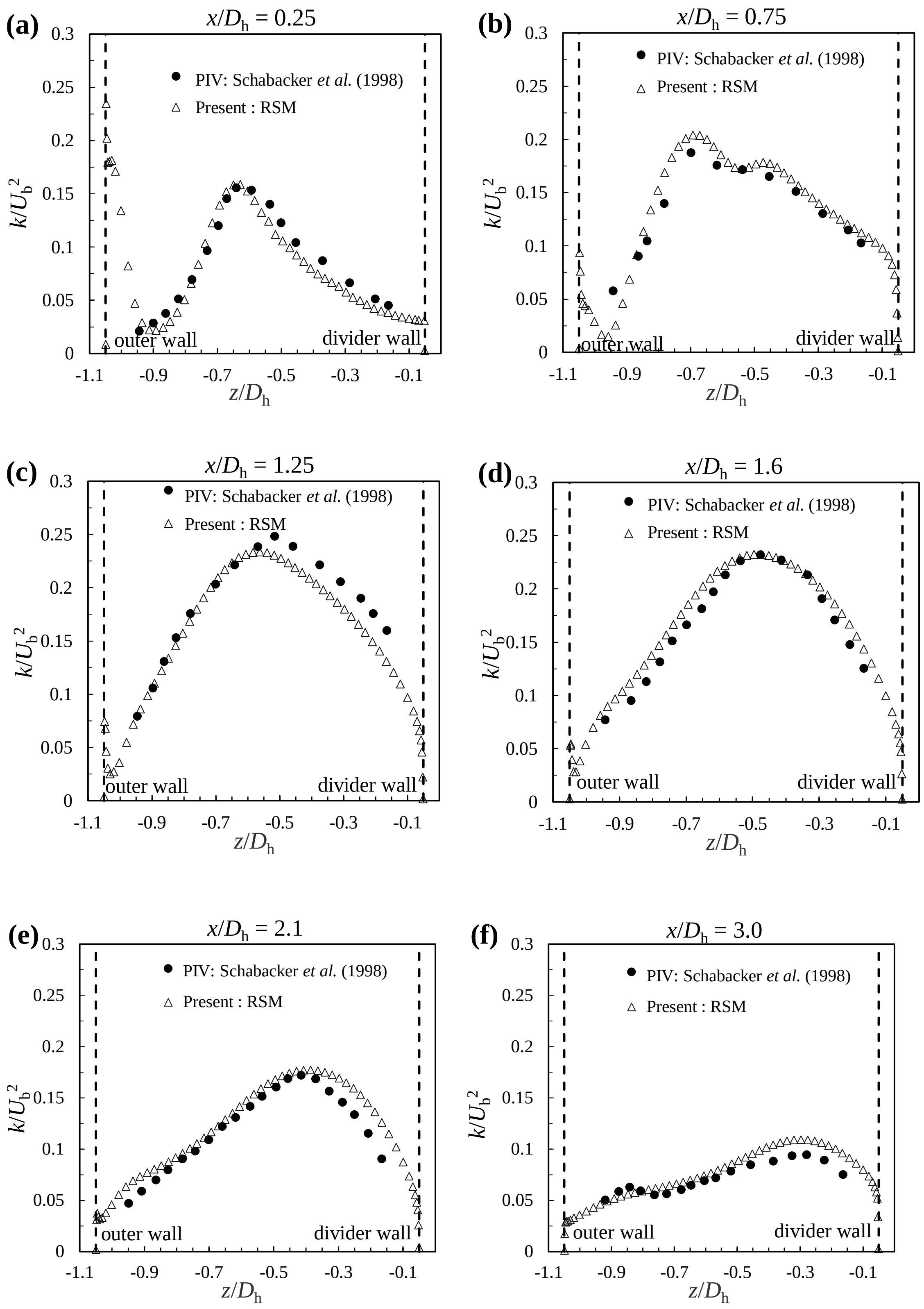
(a)
$x/D_h = 0.25$
(b)
$x/D_h = 0.75$
(c)
$x/D_h = 1.25$
(d)
$x/D_h = 1.6$
(e)
$x/D_h = 2.1$
(f)
$x/D_h = 3.0$
● PIV: Schabacker *et al.* (1998)
△ Present : RSM
k/U_b^2
0
0.05
0.1
0.15
0.2
0.25
0.3
z/D_h
-1.1
-0.9
-0.7
-0.5
-0.3
-0.1
outer wall
divider wall

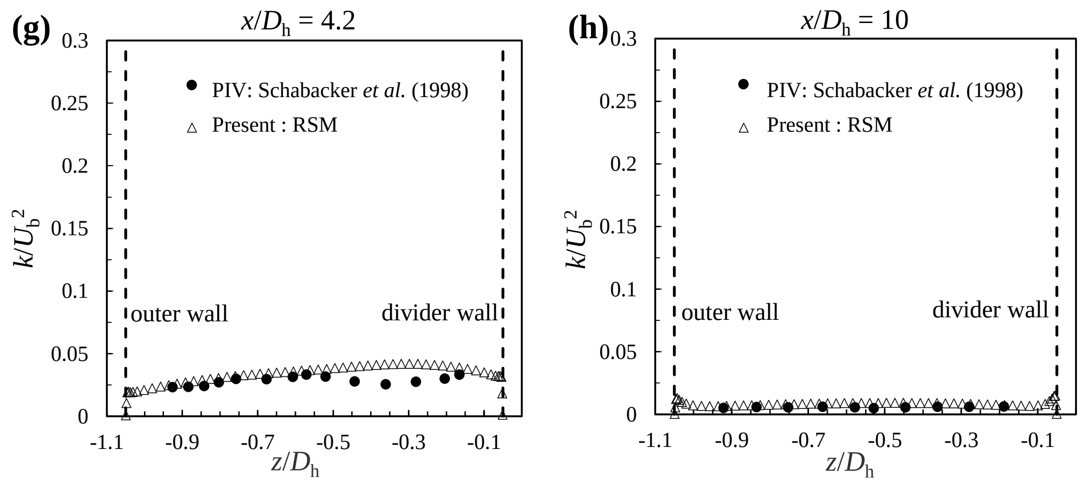

Fig 4-18: Profiles of turbulent kinetic energy *(k)* at different locations along the symmetry plane (y/D_h = 0.5) downstream of the bend for PIV: Schabacker *et al.* (circles) and RSM (triangles). The profiles are shown at the same position as in Fig 4.15.

Figures 4-18(a), (b), (c) and (d) represent the comparison of the profiles of the turbulent kinetic energy (k) of the present RSM simulation and the PIV data of *Schabacker et al., (1998)* at 8 different locations after the bend. The trends of the experimental and simulation profiles vary according to the physics of the flow and are in qualitative agreement with each other at all the 8 locations after the bend. The peak values of the turbulent kinetic energy occur in the shear layer between the recirculation bubble and the main flow in the regions where high velocity gradients and shear stresses result in the high turbulent energy production. The growth of the recirculation bubble leads to an increase in the values of turbulent kinetic energy from x/D_h = 0.25 to x/D_h = 1.6. As the flow progresses further downstream, the turbulent kinetic energy dissipates gradually to a lower turbulence level. At x/D_h = 10, the turbulent kinetic energy becomes negligible and the redevelopment of the flow takes place.

4.3 Effect of the bend clearance on velocity and turbulence parameters

The effect of the bend clearance on the velocity and turbulence parameters of the two-pass channel is studied in this section. Most prior studies relevant to 180° turning flows without duct rotation have considered only the heat transfer with little discussion of the velocity field. Considerable non-uniformity in heat transfer distribution was attributed to the observed flow separation and reattachment. The flow characteristics in such a case are affected by the turning configuration and more specifically by the divider clearance. The present study focuses on examining the effect of the latter, which receives little attention at high Reynolds number.

The two bends are represented as C^* = 0.5 and C^* = 1, where C^* is the dimensionless turn clearance and $C^* = C/D_h$, where C is the turn clearance of the channel i.e. the distance between the tip of the divider wall and the end wall of the channel.

4.4 Overall features of the mean velocity field

The overall flow pattern represented by the mean streamtraces at three different (x - z) planes located at y/D_h = 0.15 (near the bottom wall), 0.5 (center plane) and 0.85 (near the top wall) are examined. In figure 4-19, the effect of the clearances is presented in the selected planes. Before the turn, the flow is not affected by the turn and it is close to the fully developed conditions. As the flow approaches and turns in the bend, a pressure gradient develops across the section with adverse pressure gradient near the outer wall. As there is a favourable pressure gradient near the inner wall side, a strong flow acceleration takes place there. Moreover, the flow decelerates on the outer wall. In other words, the fast-moving fluid is towards the divider wall side and the slow-moving fluid towards the outer wall side. In the upstream and downstream corners of the channel, small recirculation zones are observed. This flow also separates from the sharp edge of the tip of the divider plate. As the flow progresses further downstream, strong secondary flow develops, and the pressure field changes at the bend exit. This causes a strong flow acceleration on the outer wall. Afterwards, the flow reattaches on the symmetry plane at $y/D_h = 0.5$ and the redevelopment of the boundary layer starts.

The three-dimensional character of the flow is revealed from the distribution of the flow field in the y/D_h = 0.5 and y/D_h = 0.15 planes. In the y/D_h = 0.15 plane, a larger vortex is formed in the center of the recirculation bubble downstream of the bend. The shape of the separation bubble is also not distorted as in the case of $y/D_h = 0.5$ plane in both the channels. The reattachment for the C^* = 1 takes place at about x/D_h = 2.12 and the reattachment length for the C^* = 0.5 is x/D_h = 2.43. The careful investigation shows that the reattachment length of the separation bubble is also increased as we move towards the bottom plane or the top plane. The reattachment length in C^* = 0.5 is increased to $x/D_h = 2.58$ for both the $y/D_h = 0.15$ and $y/D_h = 0.85$ planes. Moreover, the reattachment length in C^* = 1 is increased to $x/D_h = 2.36$ for both the $y/D_h = 0.15$ and $y/D_h = 0.85$ planes. This provides a conclusive evidence of the three-dimensional structure of the recirculation bubble and the flow field of the two-pass channels.

The symmetry of the flow is also analyzed by observing the distribution of the flow field at $y/D_h = 0.15$ and $y/D_h = 0.85$ planes in both the channels. Both the planes are at the same distances from the symmetry plane in the upward and downward directions. The flow fields in both the planes are exactly similar to each other. The vortex centers, the shape of the recirculation bubble and even the reattachment length of the flow is the same. Therefore, the flow field in the two-pass channel and the recirculation bubble are three-dimensional and symmetric in the mean.

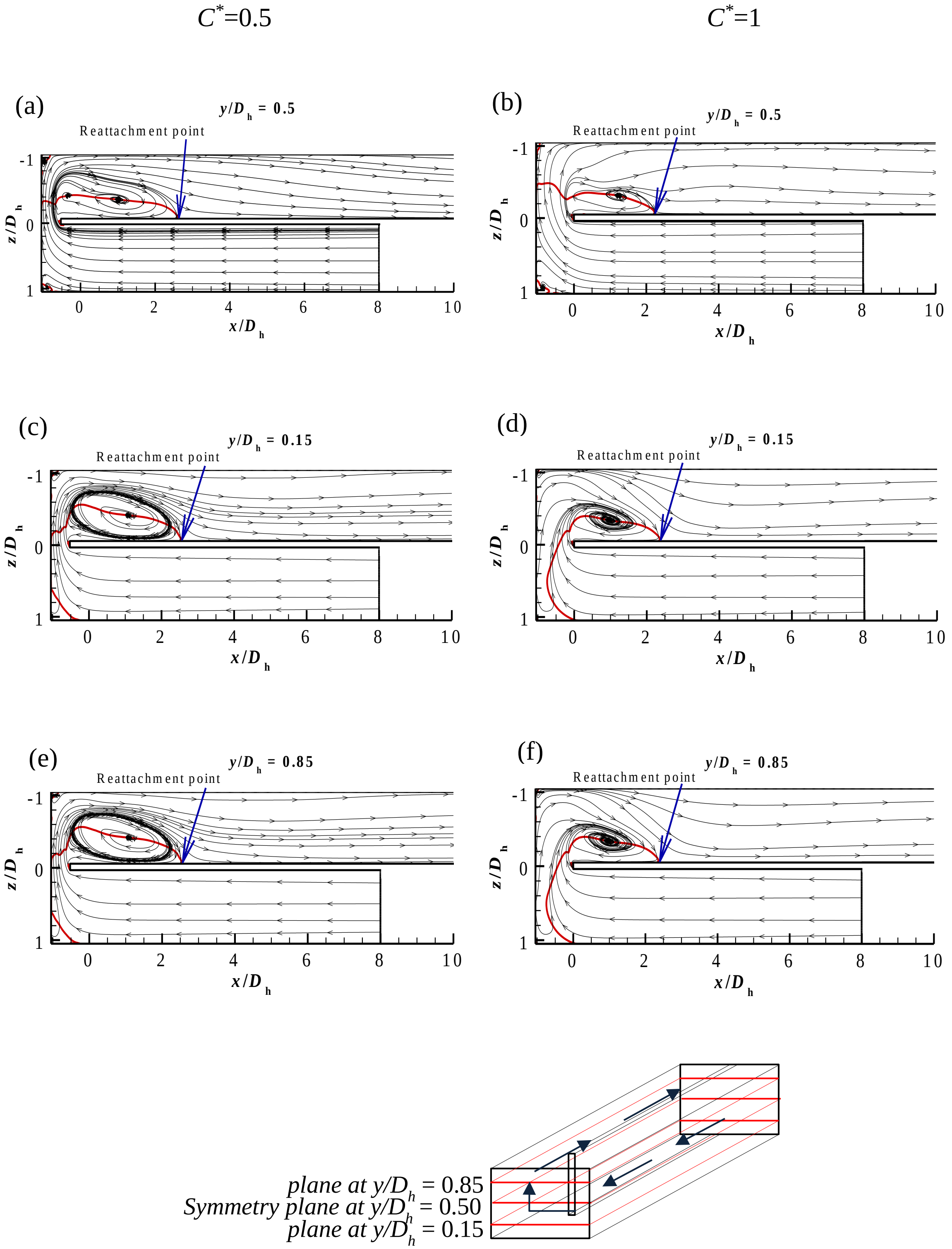

Fig 4-19: Flow field in the streamwise planes (*x*-*z* planes) of the two-pass channel with C^* = 0.5 and C^* = 1 at y/D_h = 0.15, y/D_h = 0.5 (symmetry plane) and y/D_h = 0.85. The red line in the flow field indicates the streamwise zero velocity gradient line. Schematic of the channel represents the locations of the respective profiles.

4.5 Mean and turbulence characteristics in 1D_h and 0.5 D_h bend.

4.5.1 Mean stream-wise velocity ($\overline{U}$)

This section presents the comparison of the mean stream-wise velocity for both C^* = 0.5 and C^* = 1 at locations after the bend exit.

As observed in Figure 4-20(a), the distributions of streamwise flow velocity $\overline{U}/ U_b$ are in good agreement with each other near the start of the divider wall for both the bends. This shows that the recirculation bubble has just started to form. Near the outer wall side, there is an acceleration of the flow in both the bends. However, the channel with the narrower turn will experience higher acceleration as the separation bubble will grow in size with the decrease of the turn clearance. Figure 4-20(b) also depicts the agreement of velocity distributions near the start of the divider wall but the acceleration near the outer wall is intensified for both the clearances. This intense acceleration of the flow in primarily due to the growth of the separation bubble as well as the decrease of the substantial cross sectional area of the flow passage downstream of the channel. Further, downstream of the channel, size of the separation bubble increases, and the cross section area of the main flow passage reduces in both the turns. However, for C^* = 0.5, both the acceleration of the $\overline{U}/ U_b$ near the outer wall and the reverse flow in the recirculation zone of the bubble are higher than the C^* = 1 [as shown in Figure 4-20(c),(d) and (e)].

The proceeding flow towards the divider wall is enhanced by the reattachment of the separated flow. Earlier, observation of the streamtraces represents that the reattachment lengths for the $C^* = 1$ *and* $C^* = 0.5$ are about $x/D_h = 2.12$ and $x/D_h = 2.43$ respectively. This illustrates that size of the separation bubble decreases and the substantial cross-sectional area of the flow passage increases. This further leads to the deceleration of the flow on the outer wall side. It is presented in Figure 4-20(f) and Figure 4-20(g). However, the velocity distributions near the divider and outer walls for the narrower turn clearance are more intensified than the turn with larger turn clearance. This can be caused due to the inertia force acting on the fluid passing through the narrower turn clearance, which prevents the separated flow from reattaching on the divider wall within a short distance. Figure 4-20(h) represents that farther downstream, the stream-wise velocity distributions of both the bends reach in an agreement with each other. The flow is in the developing stage due to the redevelopment of the boundary layer.

This represents that the decrease in turn clearance leads to an increase in the size of the recirculation bubble, decrease in the substantial cross-sectional area of the downstream flow passage which further leads to high acceleration near the outer wall side. The flow through a narrower turn clearance is influenced by an increasing inertia force which dominates and prevents the flow from reattaching within a shorter distance.

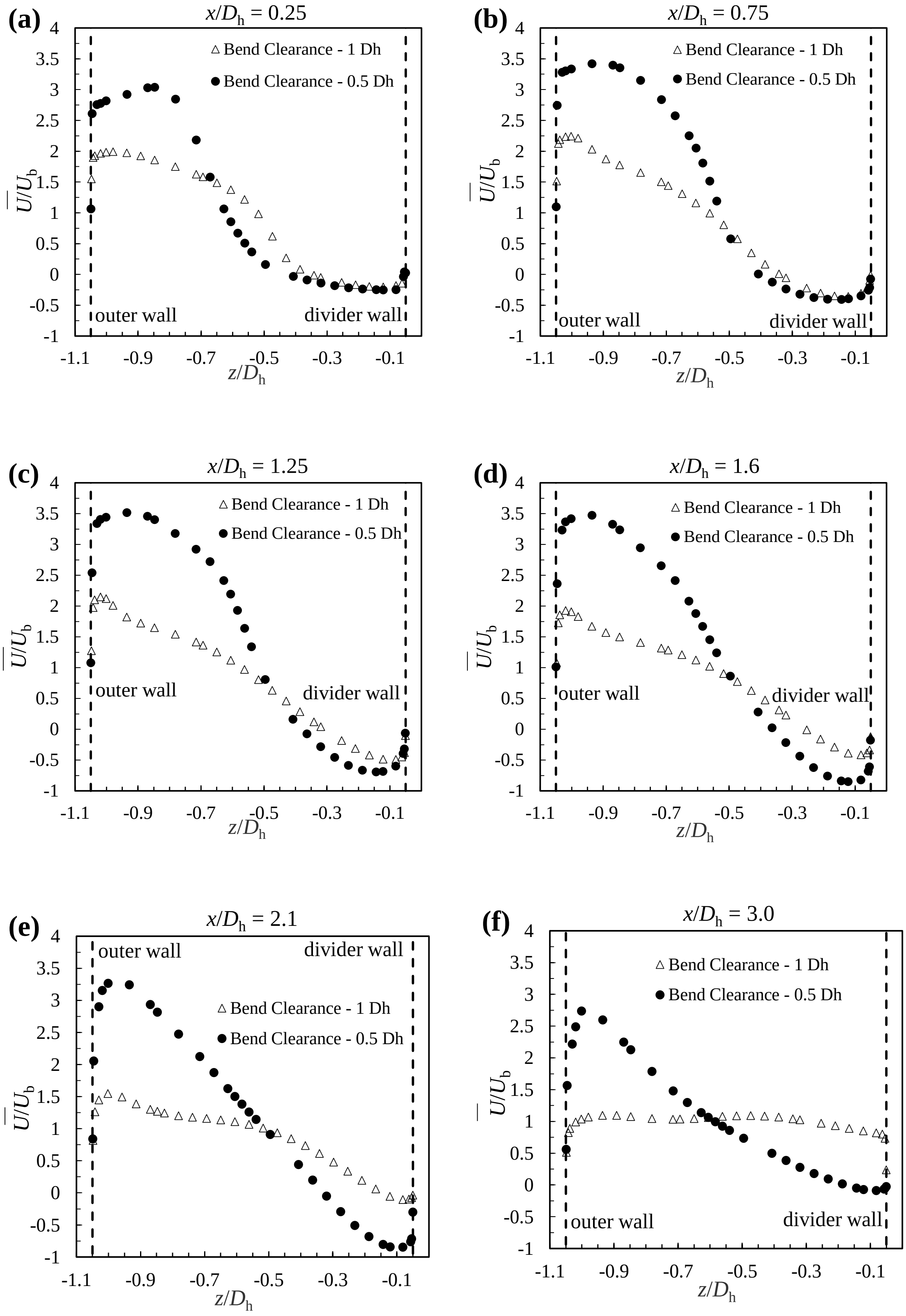
(a)
x/D_h = 0.25
(b)
x/D_h = 0.75
(c)
x/D_h = 1.25
(d)
x/D_h = 1.6
(e)
x/D_h = 2.1
(f)
x/D_h = 3.0
△ Bend Clearance - 1 Dh
● Bend Clearance - 0.5 Dh
outer wall
divider wall
$\overline{U}/U_b$
z/D_h
-1.1
-0.9
-0.7
-0.5
-0.3
-0.1
4
3.5
3
2.5
2
1.5
1
0.5
0
-0.5
-1

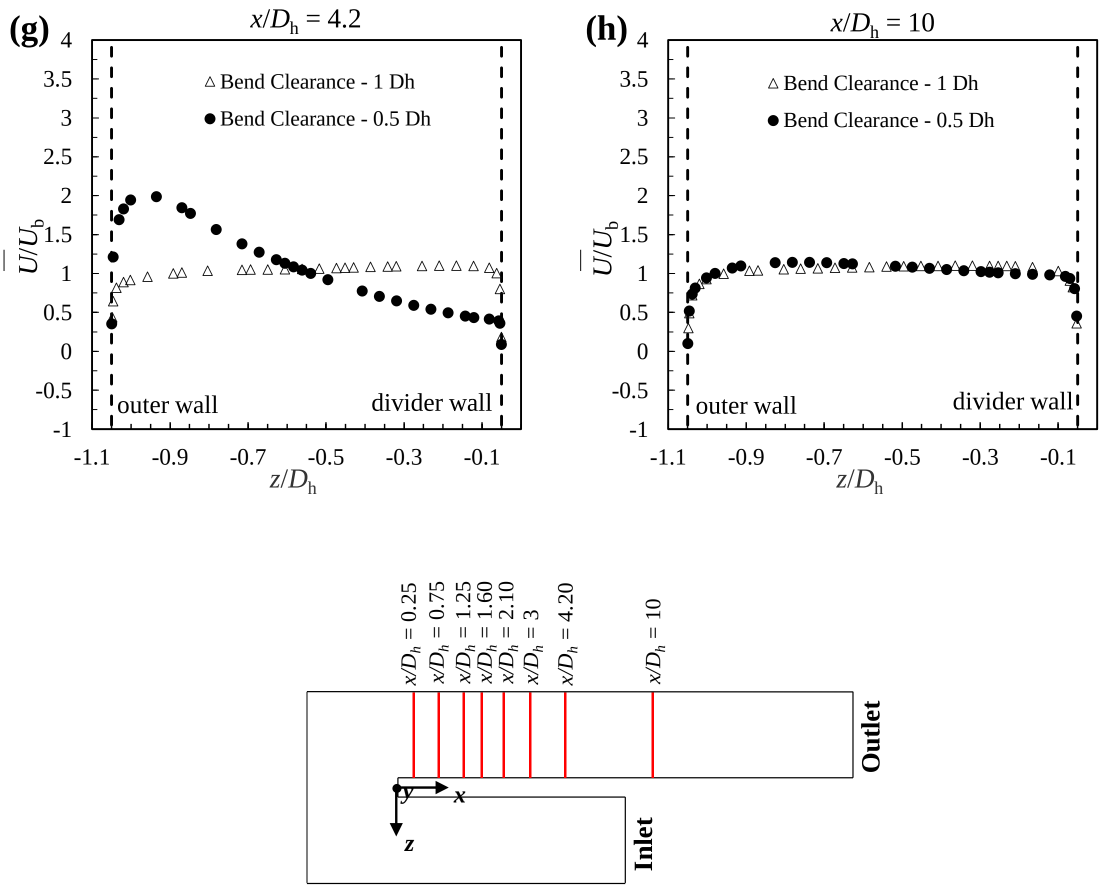

Fig 4-20: Profiles of mean streamwise velocity ($\overline{U}$) along the symmetry plane (y/D_h = 0.5) downstream of the bend for C^* = 0.5 (circles) and C^* = 1 (triangles). Schematic of the two-pass channel represents the locations of the respective profiles.

4.5.2 Streamwise fluctuating velocity (*u'*) and turbulent kinetic energy (*k*)

The effect of the bend clearance on the turbulence parameters of the two-pass channel is observed which is the objective of this study. Figure 4-21 and Figure 4-22 represent the comparisons of the profiles of *u'* and *k* for C^* = 0.5 and C^* = 1 at locations after the exit of the bend. As an overall trend, the distribution of *k* is qualitatively similar to that of the *u'*, because the streamwise velocity fluctuation is the most dominant among the fluctuating velocity components.

The mean stream-wise RMS velocity (*u'*) and turbulent kinetic energy (*k*) show considerably large values in the separation shear layer near the divider wall for both the turns. Figure 4-21(a) [or 4-22(a)] and Figure 4-21(b) [or 4-22(b)] depict an increase in the turbulence quantities near the divider wall and subsequently, the growth of the recirculation bubble on the divider wall side. Since the region near the divider wall is occupied by the separated reverse flow, the velocity gradients in the separation shear layer are considerably large and further contribute to produce strong turbulence. Figure 4-21(b) [or 4-22(b)] shows a bump in the profile of *k* or *u'* for $C^* = 1$. This is due to the decrease of the substantial cross-sectional area and the effect of the centrifugal force against the primary flow near the outer wall side. The comparison of the profiles in Figure 4-21(c) [or 4-22(c)] and Figure 4-21(d) [or 4-22(d)] delineates that both *k* and *u'* will attain the maximum values in the shear layer between the separation bubble and the main flow. This is because the production of $\overline{U^2}$ is most promoted there which results in the higher values of the velocity gradients.

Now, gradually, the flow proceeding towards the divider wall is influenced by the reattachment of the separated flow on the divider wall. The reattachment for $C^* = 1$ takes place at about $x/D_h = 2.12$ and the reattachment length for $C^* = 0.5$ is $x/D_h = 2.43$. After the flow reattachment, the main flow on the outer wall side dominates and both *k* and *u'* near the outer wall indicate an increase in the values, as depicted in Figure 4-21(f) [or 4-22(f)] and Figure 4-21(g) [or 4-22(g)]. This is because the substantial flow passage is increased, and the effect of the centrifugal force is diminished. Due to this, the primary flow in the outer wall side is slightly decelerated. This decrease makes a positive contribution to the production of $\overline{U^2}$. So, the values of both *k* and *u'* near the outer wall side will increase. The development of the flow further downstream indicates the dissipation of the turbulence to lower values. However, the comparison of the two profiles in Figure 4-21(h) [or 4-22(h)] indicates that the turbulence in the narrower ($C^* = 0.5$) bend takes longer distance to get dissipated. Therefore, this investigation presents the smaller the clearance of the bend, the higher the production of turbulence and the longer the distance required for the turbulent dissipation.

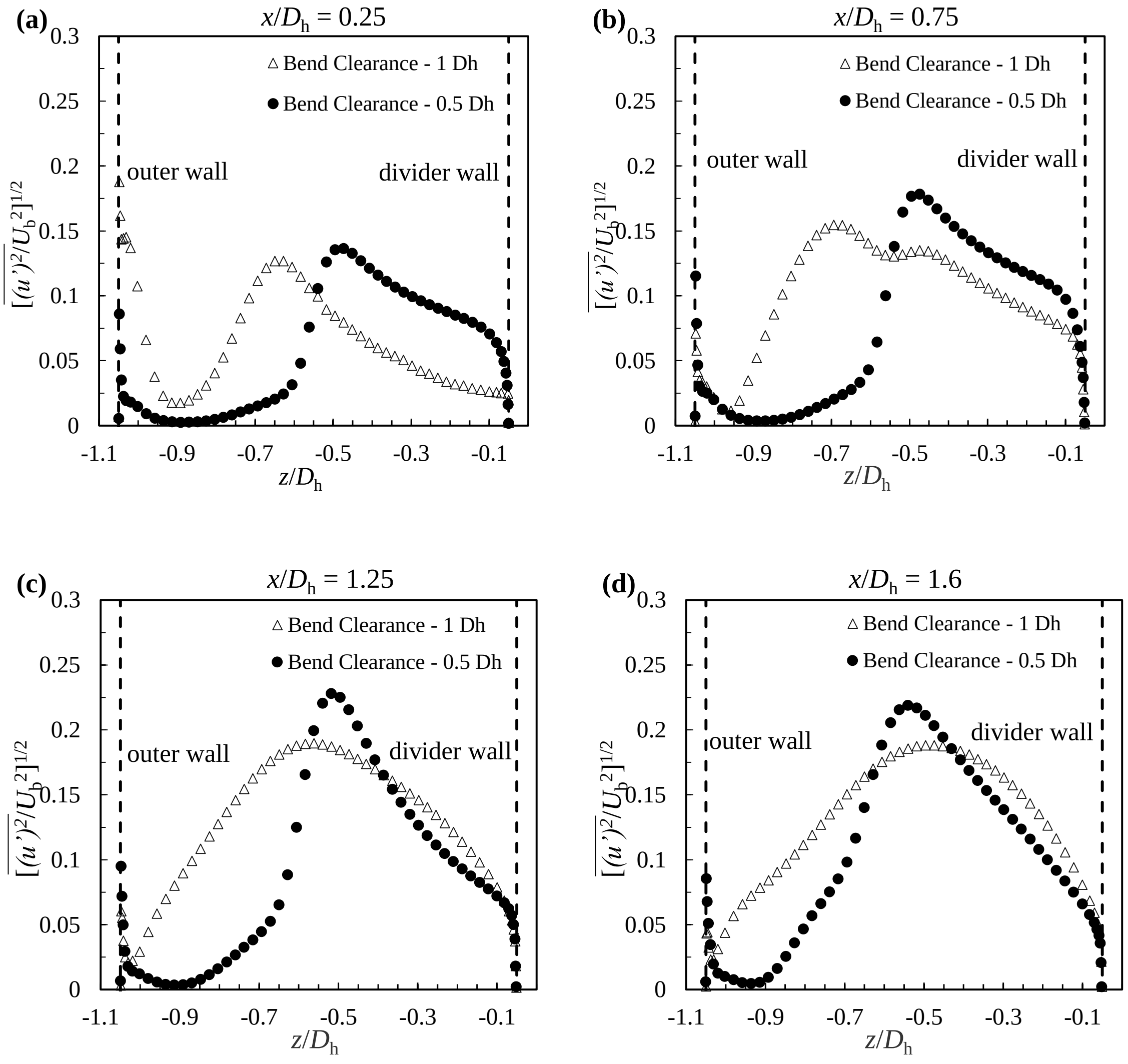

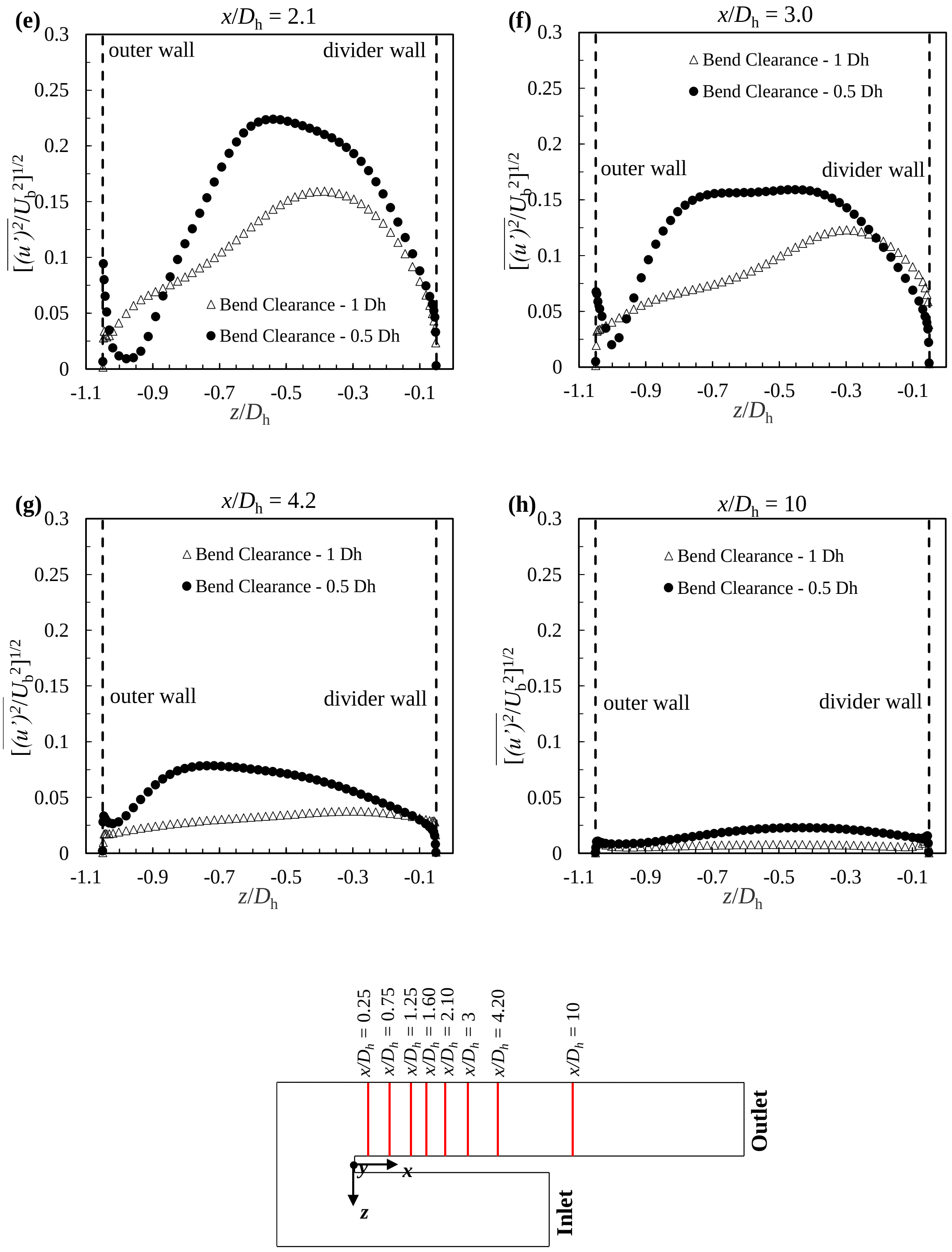

Fig 4-21: Profiles of streamwise fluctuating velocity *(u')* along the symmetry plane (y/D_h = 0.5) downstream of the bend for C^* = 0.5 (circles) and C^* = 1 (triangles). Schematic of the two-pass channel represents the locations of the respective profiles.

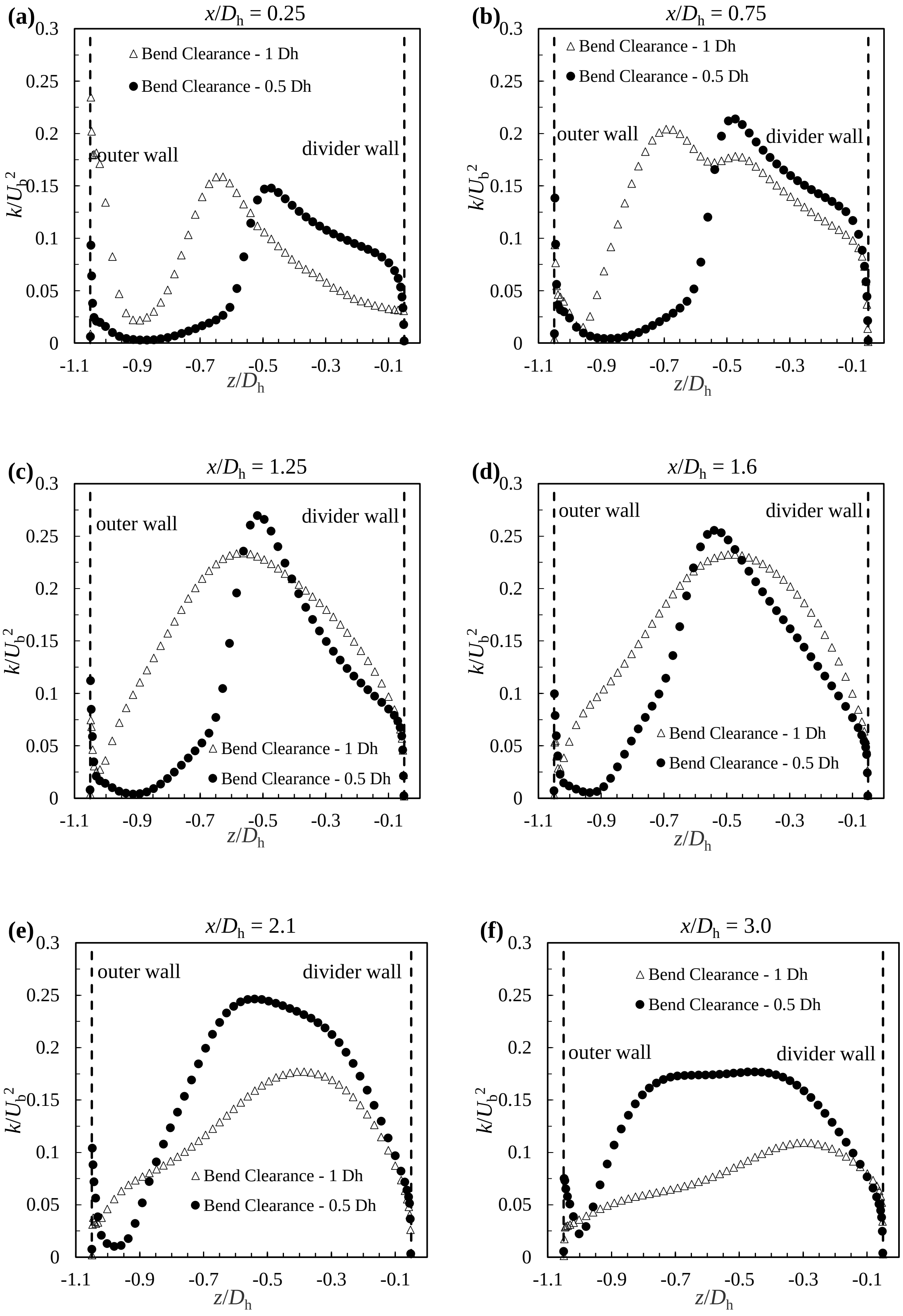

(a)
$x/D_h = 0.25$
(b)
$x/D_h = 0.75$
(c)
$x/D_h = 1.25$
(d)
$x/D_h = 1.6$
(e)
$x/D_h = 2.1$
(f)
$x/D_h = 3.0$
Bend Clearance - 1 Dh
Bend Clearance - 0.5 Dh
outer wall
divider wall
k/U_b^2
z/D_h
0
0.05
0.1
0.15
0.2
0.25
0.3
-1.1
-0.9
-0.7
-0.5
-0.3
-0.1

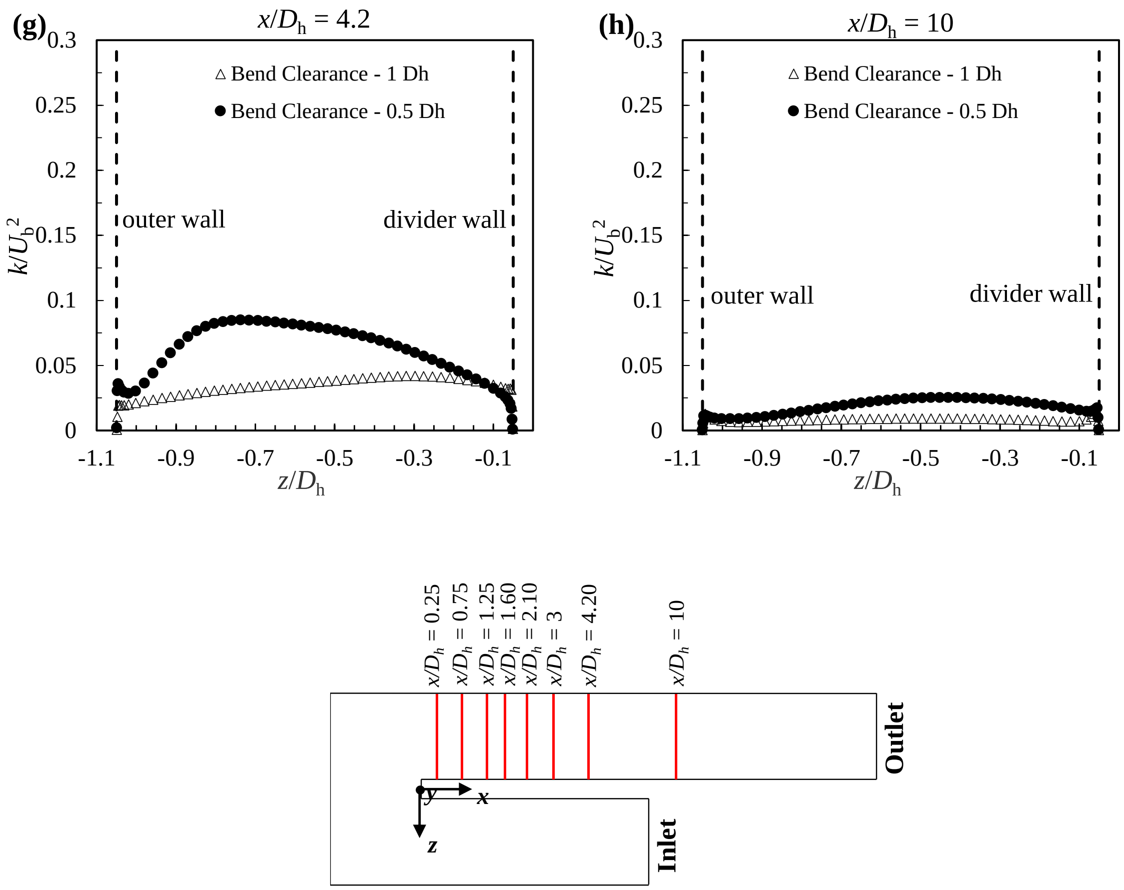

Fig 4-22: Profiles of turbulent kinetic energy *(k)* along the symmetry plane (y/D_h = 0.5) downstream of the bend for C^* = 0.5 (circles) and C^* = 1 (triangles). Schematic of the two-pass channel represents the locations of the respective profiles.

4.6 Analysis of the Dean-type secondary flow

This section represents the comparison of the secondary flow for C^* = 0.5 and C^* = 1.

The starting of the formation of the counter-rotating Dean-type vortices are shown for C^* = 0.5 at x/D_h = -0.25 in Figure 4-23(a). These vortices are formed due to the instabilities in the flow caused by the centrifugal force and the streamline curvature. The streamline curvature is the result of the flow separation at the start of the bend. The onset of the recirculation bubble near the divider wall of the bend also causes disturbances in the flow field.

As the flow progresses downstream, it becomes more and more unstable as represented in Figure 4-23(b). The size of the Dean vortices at the center and the corners increases. The recirculation bubble also grows in size. For C^* = 1 [Figure 4-23(b)], the flow near the outer wall is highly unstable as compared to the flow near the divider wall. There is a strong flow acceleration near the outer wall. The Dean vortices near the outer wall are grown in size and thus, the secondary flow near the outer wall is much intensified. With the development of the flow, at x/D_h = 0.75 [Figure 4-23(c)], the effect of the centrifugal force becomes more dominant in the channel with smaller bend clearance. The Dean vortices are formed towards the outer wall and the size is almost similar. On the other hand, in C^* = 1 [Figure 4-23(d)], the main secondary flow on the outer wall is more dominant and influences the flow on the divider wall. At x/D_h = 1.25, as shown in Figure 4-23(e),(f), the influence of the flow on the outer wall side is becoming less intense and counter-rotating vortices are also formed at the top and bottom of the divider wall. The recirculation bubble is also increasing in size. Further progress of the flow depicts that the flow is more unstable under the action of centrifugal forces and pressure gradient in the case C^* = 1. For C^* = 0.5, the flow is becoming somewhat stable and is in the state of reattachment to the divider wall [Figure 4-23(g), (h), (i), (j)]. After the reattachment of the flow, the secondary flow exists in only one direction from the outer wall towards the divider wall. The effect of the centrifugal force in the flow is diminished. Further downstream, the redevelopment of the boundary layer starts [Figure 4-23(k), (l), (m), (n)]. At x/D_h = 10, far in the downstream, the redevelopment of the vortices from the four corners can be examined. The flow is still in the developing stage and resembles with the flow in a square duct having counter rotating vortices from the four corners [Figure 4-23(o), (p)].

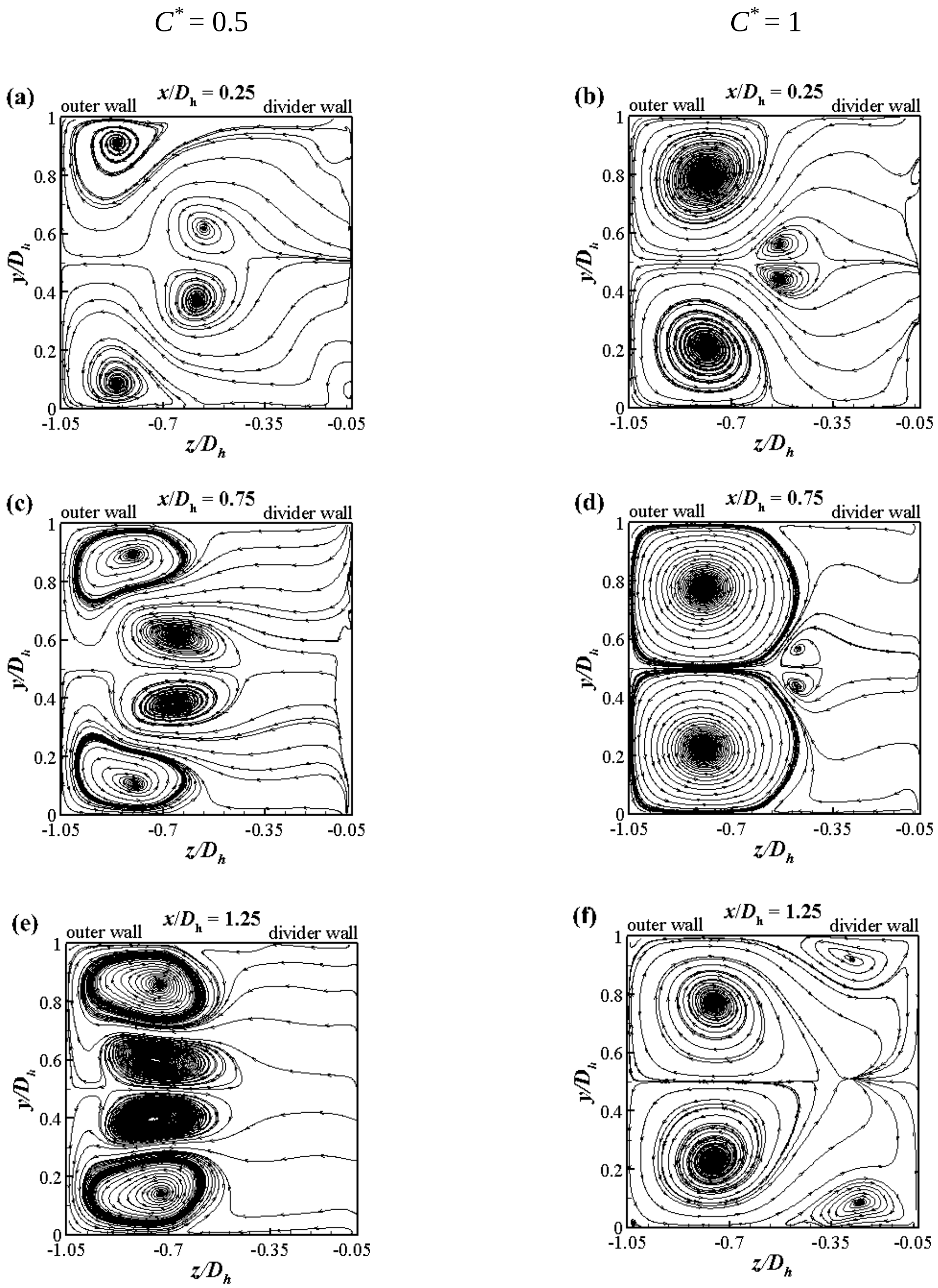

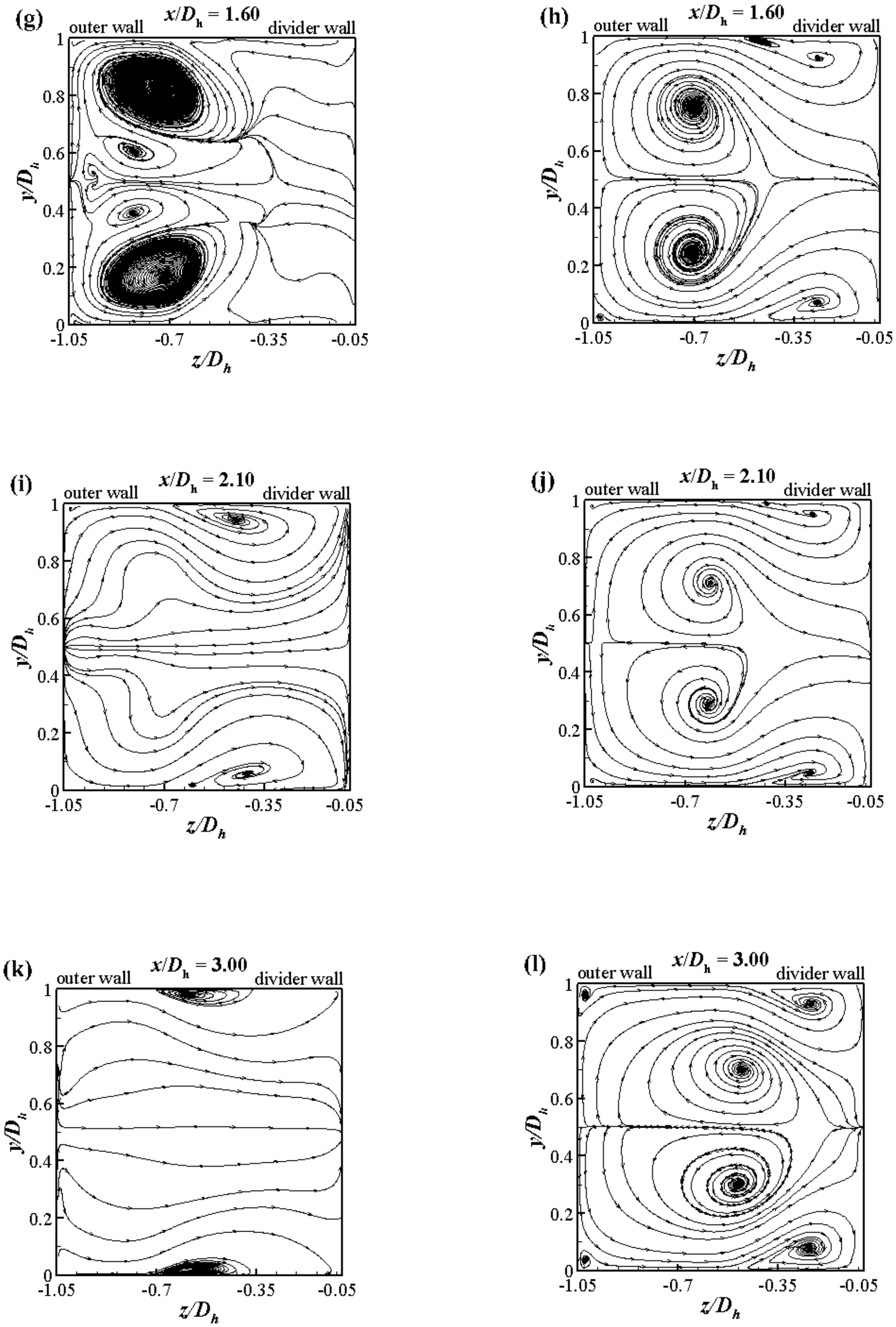
(g)
x/D_h = 1.60
outer wall
divider wall
(h)
x/D_h = 1.60
outer wall
divider wall
(i)
x/D_h = 2.10
outer wall
divider wall
(j)
x/D_h = 2.10
outer wall
divider wall
(k)
x/D_h = 3.00
outer wall
divider wall
(l)
x/D_h = 3.00
outer wall
divider wall
y/D_h
z/D_h
0
0.2
0.4
0.6
0.8
1
-1.05
-0.7
-0.35
-0.05

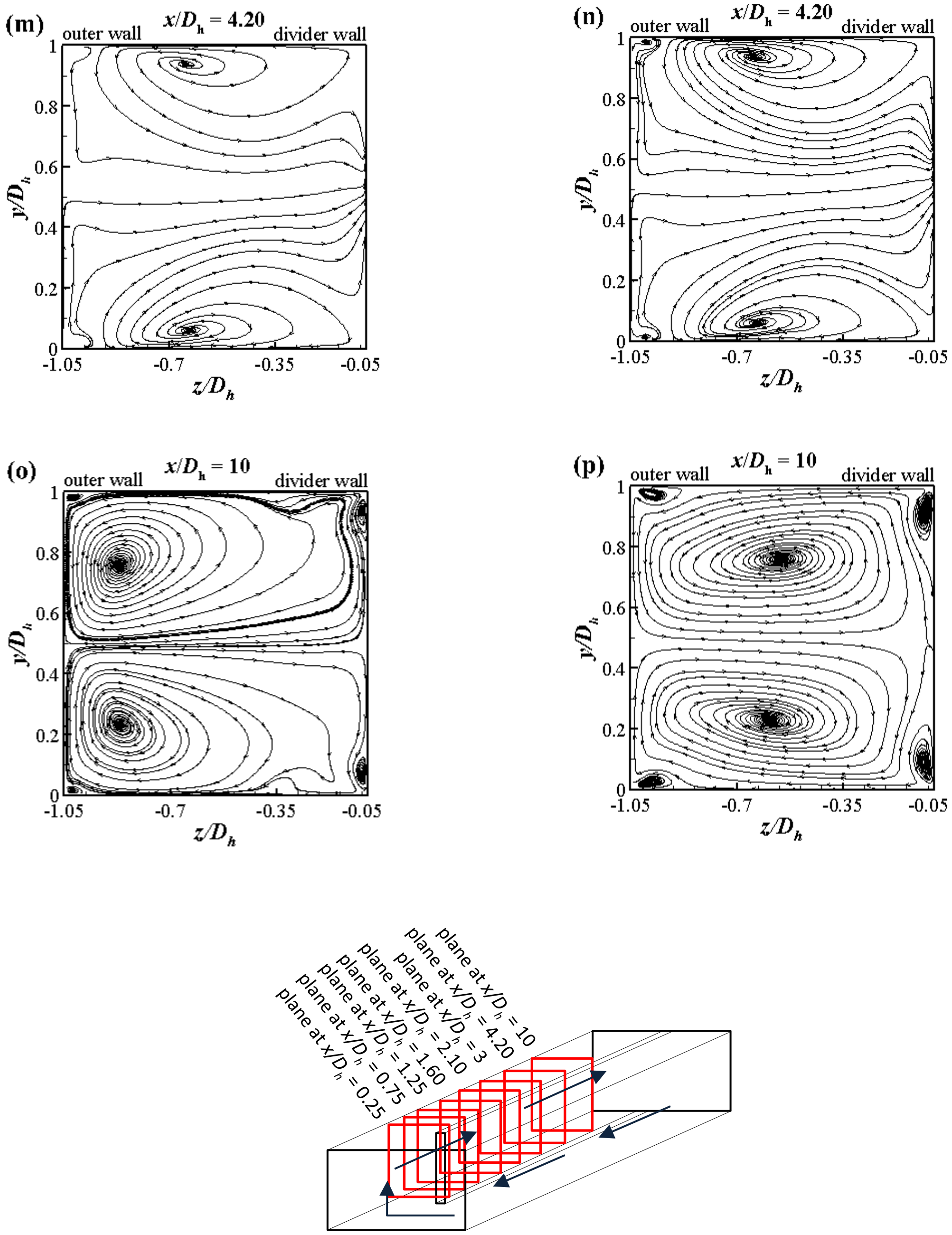

Fig 4-23: Comparison of the secondary flow field in channels with two different bend clearances (left column $C^* = 0.5D_h$ and right column $C^* = 1D_h$). Schematic of the channel represents the locations of the respective plane.

4.7 Evaluation of the flow field using Q-criterion.

It is well established that coherent/organized structures are responsible for the transport of mass, momentum and heat transfer in turbulent flows. As both the bends present a 3-D flow field, the ‘vortex identification techniques’ can be used to educe the coherent structures in the flow.

The velocity gradient tensor $\overline{D}$ can be written as $D_{ij} = \frac{\partial u_i}{\partial x_j}$. As this is a second order tensor, it can be decomposed into a symmetric and a skew-symmetric part

$$D_{ij} = S_{ij} + \Omega_{ij} \text{ where } S_{ij} = \frac{1}{2}\left(\frac{\partial u_i}{\partial x_j} + \frac{\partial u_j}{\partial x_i}\right) \text{ and } \Omega_{ij} = \frac{1}{2}\left(\frac{\partial u_i}{\partial x_j} + \frac{\partial u_j}{\partial x_i}\right)$$

where S_{ij} is known as the rate-of-strain tensor, and Ω_{ij} is the vorticity tensor.

The characteristic equation for the ∇u is given by:

$$\lambda^3 + \mathrm{P}\lambda^2 + \mathrm{Q}\lambda + \mathrm{R} = 0$$

where P, Q and R are the three invariants of the velocity gradient tensor. Using the decomposition into the symmetric and anti-symmetric parts, these invariants can be expressed as follows:

$$\mathrm{P} = -\mathrm{tr}(\overline{D}), \quad \mathrm{Q} = \frac{1}{2}(\mathrm{tr}(\overline{D})^2 - \mathrm{tr}(\overline{D}^2)) = \frac{1}{2}\ ||\bar{\Omega}||^2 - ||\bar{S}||^2, \quad \mathrm{R} = -\mathrm{det}(\overline{D})$$

The Q-criterion is used to identify the coherent structures in the flow. The Q-criterion defines a vortex as a connected fluid region with a positive second invariant of ∇u, i.e. Q > 0. Conventionally, the definition of the second invariant clarifies that Q represents the local balance between the shear strain rate and the vorticity magnitude, defining vortices as the areas where the vorticity magnitude is greater than the magnitude of rate-of-strain.

Figures 4-24 and 4-25 show the coherent structures in the two-pass channel flow field captured using threshold of Q = -20. The iso-surface of Q is colored by the contours of normalized pressure and normalized velocity magnitude respectively. With the development of the flow, the large-scale vortical (tube-like) structures are created from the upstream corner to the downstream of the bend due to the interaction between the main flow and the secondary flow. As the flow turns it separates and forms the recirculation bubble, these structures are transported into the recirculation region. During this process and within the recirculation region, the structures interact, and break into the small-scale vortical (worm like) structures. As it can be seen in both the bend clearances, the pressure field completely changes after the turn. The pressure becomes very low near the outer wall side. This is due to the strong flow acceleration after the turn and the shear layer formed between the main flow interacting with the flow in the recirculation bubble region. The pressure becomes negligible after the reattachment of the flow. These three-dimensional pressure and velocity distributions provide a clear description of the vortical structures in the mean flow.

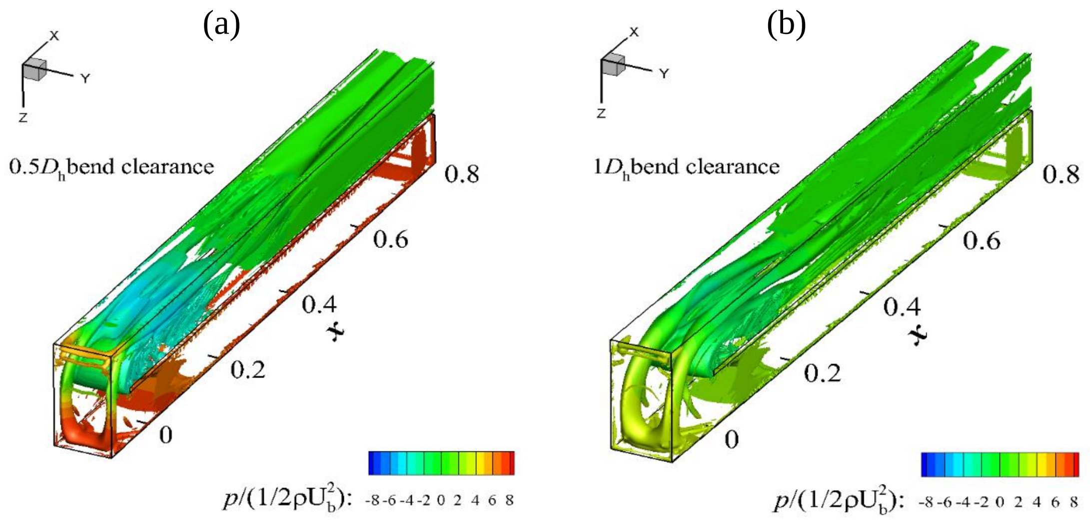

Fig 4-24: Structures using Q-criterion colored by normalized pressure. The structures are presented in the region of interest (-0.105<x<0.8) near the bend.

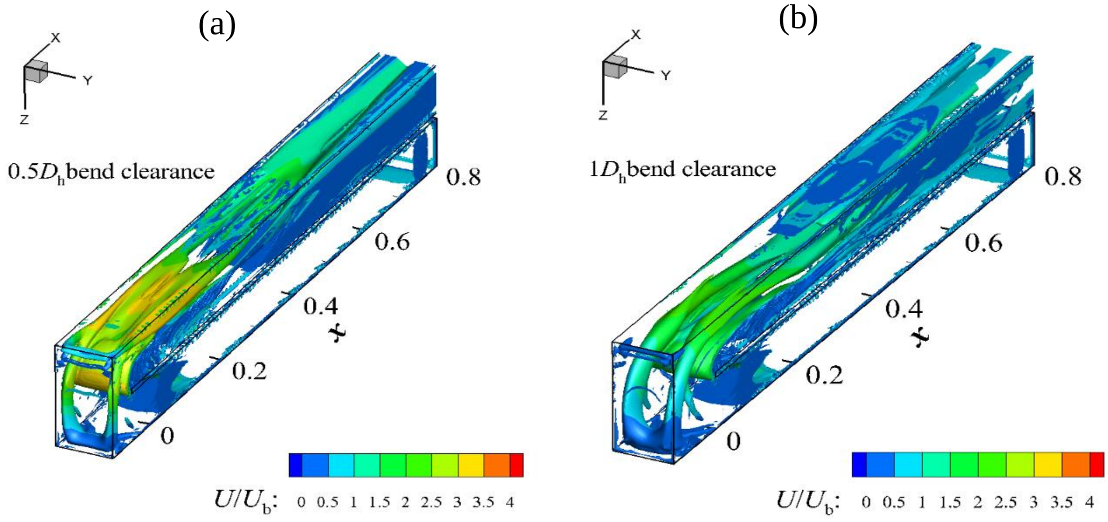

Fig 4-25: Structures using Q-criterion colored by normalized velocity magnitude. The structures are presented in the region of interest (-0.105<x<0.8) near the bend.

Figures 4-26(a) and (b) show the structures in the two-pass channel flow captured using threshold of Q = -20. In this case, the iso-surface is colored by the magnitude of the normalized turbulent kinetic energy. The production of the turbulent kinetic energy is maximum in the shear layer between the recirculation bubble and the main flow in the regions where the velocity gradients are high. The large-scale structures are also formed in the form of vortex streets due to the streamline curvature of the bend. These structures are responsible for the high turbulent kinetic energy in this region. However, these structures are convected into the recirculation zone, in this process they are immediately broken down into smaller scales. These small-scale structures are predominantly responsible for the reattachment and turbulent dissipation in the flow field.

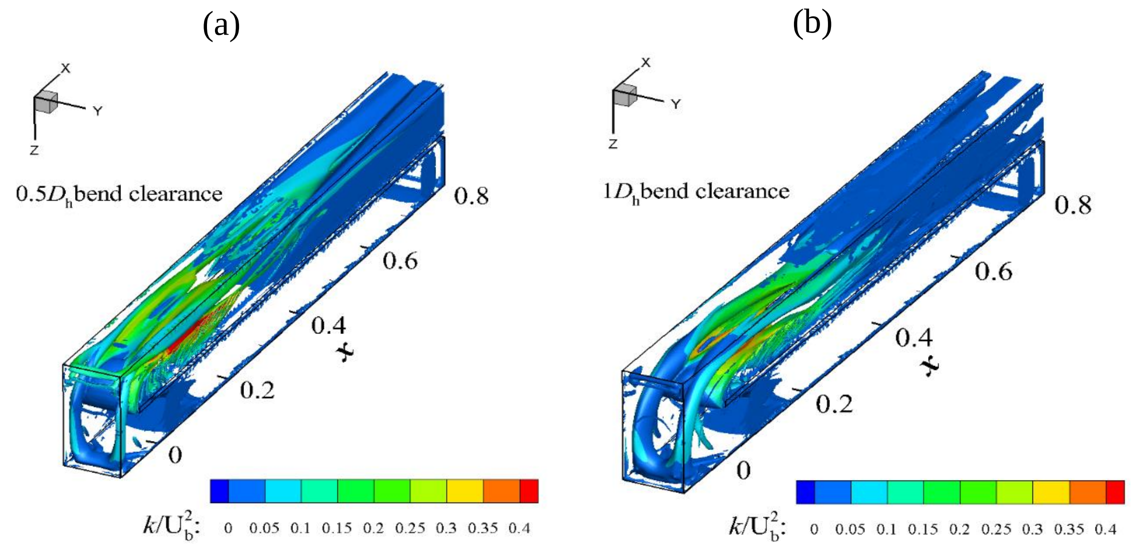

Fig 4-26: Structures using Q-criterion colored by normalized turbulent kinetic energy. The structures are presented in the region of interest (-0.105<*x*<0.8) near the bend.

CHAPTER 5: SUMMARY & CONCLUSIONS

5.1 Summary

The flow field of the two-pass channel is three-dimensional. The recirculation bubble is formed after the flow takes a sharp turn. The influence of the bend clearance on the turbulence parameters is analyzed in this study. A computational investigation of the two-pass channel with two different bend clearances is carried out using 3-D, unsteady, RSM simulation.

The approach for this study is carried out to first investigate the turbulent flows in a pressure-driven straight duct with square cross-section at high Reynolds number (Re = 40,000) to reach flow conditions which are representative of fully developed turbulence. For this approach, a 3-D, steady, RSM simulation of the square duct is carried out. The results of the simulation are quantitatively validated with the available DNS data of Pirozzoli *et al.*, (2018). The secondary flow caused by the redistribution of the momentum in the square duct is analyzed. The similarity of the velocity and vorticity contours at different locations in the square duct provides an indication of the fully developed turbulent flow.

This is used as the approach flow condition at the inlet of the two-pass channel. The flow characteristics before the bend, in the bend and after the bend are quantitatively and qualitatively validated with the PIV data of Schabacker *et al.*, (1998). The bend clearance of the two-pass channel was changed to half of its size i.e. from $1D_h$ to $0.5D_h$. The comparison of the turbulent kinetic energy of the two-pass channels with different bend clearances concludes that the smaller the clearance of the bend, the larger and longer the recirculation bubble, the higher the production of turbulence and the longer the distance required for the dissipation of turbulence. The three-dimensional structure of the flow-field and the recirculation bubble is also analyzed. The comparison of Dean-type secondary motion with two different bend clearances reveal that the smaller the clearance of the bend, the higher the influence of the centrifugal force and the larger the instabilities in the flow. The structures that are responsible for the enhanced turbulence generation in the two-pass channel flow field are identified using Q-criterion. The results show that the recirculation bubble is composed of largely small-scale structures. However, the large-scale structures are also formed in the form of vortex streets due to the streamline curvature of the bend. These structures are responsible for the high turbulent kinetic energy in this region. However, these structures are convected into the recirculation zone, in this process they are immediately broken down into smaller scales. These small-scale structures are predominantly responsible for the reattachment and turbulent dissipation in the flow field.

5.2 Future work

The present computational study sheds light on the mean flow properties and the turbulence parameters in the two-pass channel. Some of the future recommendations are as follows:

- The present simulation is carried out for only two different bend clearances. The future work may be extended to include different values of the bend clearance to check its influence on the flow properties.

- The two-pass channel flow field can be analyzed with the heat transfer on the walls. Rather than a smooth channel, the ribs can be introduced at the channel walls.
- The present study is carried out at only one Reynolds number. The future investigation of the flow properties can be done at varying the Reynolds number to check the Reynolds number dependency of the flow field.

REFERENCES

Astarita, T., & Cardone, G. (2000). Thermofluidynamic analysis of the flow in a sharp 180° turn channel. Experimental Thermal and Fluid Science, 20, 188-200.

Besserman, D. L., & Tanrikut, S. (1991). Comparison of Heat Transfer Measurements with Computations for Turbulent Flow Around a 180 Degree Bend. Pratt & Whitney Group Engineering and Technology, East Hartford, CT 06040, Volume 4: Heat Transfer; Electric Power; Industrial and Cogeneration, V004T09A001. https://doi.org/10.1115/91-GT-002

Bradshaw, P. (1987). Turbulent Secondary Flows. Ann. Rev. Fluid Mech. 1987. 19: 53-74.

Brundrett, E., & Baines, W. D. (1964). The production and diffusion of vorticity in duct flow. Journal of Fluid Mechanics, 19(3), 375–394. https://doi.org/10.1017/S0022112064000799

CD-adapco, STAR-CCM+ User Guide, 2012

Cheah, S.C., Iacovides, H., Jackson, D.C., Li, H., Launder, B.E., (1994) LDA investigation of the flow development through rotating U-ducts, J. Turbomach., Jul 1996, 118(3): 590-596. https://doi.org/10.1115/1.2836706.

Chyu, M. K. (1991). Regional heat transfer in two-pass and three-pass passages with 180-deg sharp turns. Journal of Heat Transfer, 113(1), 63–70. https://doi.org/10.1115/1.2910553

Dean, W. R. (1927). "Note on the motion of fluid in a curved pipe". Phil. Mag. 4 (20): 208–223. doi:10.1080/14786440708564324

Demuren, A. O., & Rodi, W. (1984). Calculation of turbulence-driven secondary motion in non-circular ducts. Journal of Fluid Mechanics, 140, 189–222. https://doi.org/10.1017/S0022112084000574

Eggels, J. G. M., Unger, F., Weiss, M. H., Westerweel, J., Adrian, R. J., Friedrich, R., & Nieuwstadt, F. T. M. (1994). Fully developed turbulent pipe flow: A comparison between direct numerical simulation and experiment. Journal of Fluid Mechanics, 268, 175–210. https://doi.org/10.1017/S002211209400131X

Ekkad, S. V., & Han, J.-C. (1997). Detailed heat transfer distributions in two-pass square channels with rib turbulators. International Journal of Heat and Mass Transfer, 40(11), 2525–2537. https://doi.org/10.1016/S0017-9310(96)00318-3

Ekkad, S. V., Pamula, G., & Shantiniketanam, M. (2000). Detailed heat transfer measurements inside straight and tapered two-pass channels with rib turbulators. Experimental Thermal and Fluid Science, 22(3–4), 155–163. https://doi.org/10.1016/S0894-1777(00)00022-4

Gallo, M., & Astarita, T. (2010). 3D reconstruction of the flow and vortical field in a rotating sharp “U” turn channel. Experiments in Fluids, 48(6), 967–982. https://doi.org/10.1007/s00348-009-0776-5

Gavrilakis, S. (1992). Numerical simulation of low-Reynolds-number turbulent flow through a straight square duct. Journal of Fluid Mechanics, 244(1), 101. https://doi.org/10.1017/S0022112092002982

Gessner, F. B., & Jones, J. B. (1965). On some aspects of fully developed turbulent flow in rectangular channels. Journal of Fluid Mechanics, 23(4), 689–713. https://doi.org/10.1017/S0022112065001635

Han, J.C., Chandra, P. R., & Lau, S. C. (1988). Local heat/mass transfer distributions around sharp 180 deg turns in two-pass smooth and rib-roughened channels. Journal of Heat Transfer, 110(1), 91–98. https://doi.org/10.1115/1.3250478

Han, J.C., Dutta, S., & Ekkad, S. (2012). Gas Turbine Heat Transfer and Cooling Technology, Journal of Thermal Science and Engineering Applications, 158.

Hirota, M., Fujita, H., Cai, L., Nakayama, H., Yanagida, M., & Syafa'at, A. (2002). Heat (mass) transfer in rectangular cross-sectioned two-pass channels with an inclined divider wall. International Journal of Heat and Mass Transfer, 45(5), 1093–1107. https://doi.org/10.1016/S0017-9310(01)00212-5

Hirota, M., Fujita, H., Syuhada, A., Araki, S., Yoshida, T., & Tanaka, T. (1999). Heat/mass transfer characteristics in two-pass smooth channels with a sharp 180-deg turn. International Journal of Heat and Mass Transfer, 42(20), 3757–3770. https://doi.org/10.1016/S0017-9310(99)00057-5

Hirota, M., Fujita, H., Tanaka, A., Araki, S., & Tanaka, T. (1997). Local heat (mass) transfer characteristics in rectangular ducts with a sharp 180-degree turn. Energy Conversion and Management, 38(10–13), 1155–1168. https://doi.org/10.1016/S0196-8904(96)00145-8

Hoagland, L. C. (1960). Fully developed turbulent flow in straight rectangular ducts – secondary flow, its cause and effect on the primary flow. PhD thesis, Department of Mechanical Engineering, MIT, Cambridge, MA, United States.

Iacovides, H., Jackson, D. C., Si, H., Kelemenis, G., Launder, B. E., & Nikas, K. (1998). LDA study of the flow development through an orthogonally rotating U-bend of strong curvature and rib roughened walls, Journal of Turbomachinery, 120.

Jang, Y.J., Chen, H.C., Han, J.C., (2001). Computation of flow and heat transfer in two-pass channels with 60 deg. ribs, J. Heat Transfer, 123, 563–575.

J-C. Han, P. Zhang, (1991). Effect of Rib-Angle Orientation on Local Mass Transfer Distribution in a Three-Pass Rib-Roughened Channel, Journal of Turbomachinery, 113, pp. 123-130.

Jesudhas, V., Balachandar, R., Roussinova, V., & Barron, R. (2018). Turbulence Characteristics of Classical Hydraulic Jump Using DES. Journal of Hydraulic Engineering, 144(6), 04018022. https://doi.org/10.1061/(ASCE)HY.1943-7900.0001427

Kalpakli, A., (2014) Vortices in turbulent curved pipe flow - rocking, rolling and pulsating motions. CCGEx & Linné Flow Centre, KTH Mechanics, Royal Institute of Technology, SE–100 44 Stockholm, Sweden.

Lardeau, S., & Manceau, R. (2002). Computations of complex flow configurations using a modified elliptic-blending Reynolds-Stress model.

Launder, B. E., Reece, G. J., & Rodi, W. (1975). Progress in the development of a Reynolds-stress turbulence closure. Journal of Fluid Mechanics, 68(3), 537–566. https://doi.org/10.1017/S0022112075001814

Launder, B. E., & Ying, W. M. (1972). Secondary flows in ducts of square cross-section. Journal of Fluid Mechanics, 54(2), 289–295. https://doi.org/10.1017/S0022112072000680

Liou, T.-M. (1999). Fluid Flow in a 180 deg sharp turning duct with different divider thicknesses, Journal of Turbomachinery, 121(3): 569-576.

Liou, T.-M., & Chen, C.-C. (1999). LDV study of developing flows through a smooth duct with a 180 deg straight-corner turn, Journal of Turbomachinery, 121(1): 167-174.

Liou, T.-M., Chen, C.-C., Tzeng, Y.-Y., and Tsai, T.-W., (2000) Non-intrusive measurements of near-wall fluid flow and surface heat transfer in a serpentine passage, Int. J. Heat and Mass Transfer, 43, 17, 3233-3244.

Manceau, R., & Hanjalić, K. (2002). Elliptic blending model: A new near-wall Reynolds-stress turbulence closure. Physics of Fluids, 14(2), 744–754. https://doi.org/10.1063/1.1432693

Mani, M., Babcock, D., Winkler, C., & Spalart, P. (2013). Predictions of a supersonic turbulent flow in a square duct. 51st AIAA Aerospace Sciences Meeting Including the New Horizons Forum and Aerospace Exposition. 51st AIAA Aerospace Sciences Meeting including the New Horizons Forum and Aerospace Exposition, 07-10 January 2013, Grapevine (Dallas/Ft. Worth Region), Texas. https://doi.org/10.2514/6.2013-860

Metzger, D. E., & Sahm, M. K. (1986). Heat transfer around sharp 180-deg turns in smooth rectangular channels. Journal of Heat Transfer, 108(3), 500. https://doi.org/10.1115/1.3246961

Murata, A., & Mochizuki, S. (2004). Large eddy simulation of turbulent heat transfer in a rotating two-pass smooth square channel with sharp 180° turns. International Journal of Heat and Mass Transfer, 47(4), 683–698. https://doi.org/10.1016/j.ijheatmasstransfer.2003.07.022

Nakayama, H., Hirota, M., Fujita, H., Yamada, T., & Koide, Y. (2006). Fluid flow and heat transfer in two-pass smooth rectangular channels with different turn clearances. Journal of Turbomachinery, 128(4), 772–785. https://doi.org/10.1115/1.2101854

Nasif, G., Barron, R. M., & Balachandar, R. (2014). DES evaluation of near-wake characteristics in a shallow flow. Journal of Fluids and Structures, 45, 153–163. https://doi.org/10.1016/j.jfluidstructs.2013.12.004

Nikuradse, J. (1930). Turbulente strömung in nicht-kreisförmigen rohren. Ing.-Arch. 1, 306–332.

Park, C. W., & Lau, S. C. (1998). Effect of channel orientation of local heat (mass) transfer distributions in a rotating two-pass square channel with smooth walls. Journal of Heat Transfer, 120(3), 624–632. https://doi.org/10.1115/1.2824323

Pirozzoli, S., Modesti, D., Orlandi, P., & Grasso, F. (2018). Turbulence and secondary motions in square duct flow. Journal of Fluid Mechanics, 840, 631–655. https://doi.org/10.1017/jfm.2018.66

Prandtl, L. (1927). Turbulent flow. NACA TM-435.

Rau, G. (1998). The effect of periodic ribs on the local aerodynamic and heat transfer performance of a straight cooling channel, Journal of Turbomachinery, Apr 1998, 120(2): 368-375.

Rhie, C. M., & Chow, W. L. (1983). Numerical study of the turbulent flow past an airfoil with trailing edge separation. AIAA Journal, 21(11), 1525–1532. https://doi.org/10.2514/3.8284

Saha, K., & Acharya, S. (2013). Effect of bend geometry on heat transfer and pressure drop in a two-pass coolant square channel for a turbine. Journal of Turbomachinery, 135(2), 021035. https://doi.org/10.1115/1.4006665

Schabacker, J., Bolcs, A., & Johnson, B. V. (1998a). PIV investigation of the flow characteristics in an internal coolant passage with 45deg rib arrangement, ASME 1999 International Gas Turbine and Aeroengine Congress and Exhibition**,** 99-GT-120, V003T01A024. https://doi.org/10.1115/99-GT-120

Schabacker, J., Bölcs, A., & Johnson, B. V. (1998b). PIV investigation of the flow characteristics in an internal coolant passage with two ducts connected by a sharp 180° bend. Volume 4: Heat Transfer; Electric Power; Industrial and Cogeneration, V004T09A094. https://doi.org/10.1115/98-GT-544

Son, S. Y., Kihm, K. D., & Han, J.-C. (2002). PIV flow measurements for heat transfer characterization in two-pass square channels with smooth and 90° ribbed walls. International Journal of Heat and Mass Transfer, 45(24), 4809–4822. https://doi.org/10.1016/S0017-9310(02)00192-8

Syuhada, A., Hirota, M., Fujita, H., Araki, S., Yanagida, M., & Tanaka, T. (2001). Heat (mass) transfer in serpentine flow passage with rectangular cross-section. Energy Conversion and Management, 42 (2001) 1867 1885.

Versteeg, H.K., & Malalasekera, W, (1995). An Introduction to CFD Finite volume method, 1st Edition, Longman scientific & technical, 1995.

Vinuesa, R., Noorani, A., Lozano-Durán, A., Khoury, G. K. E., Schlatter, P., Fischer, P. F., & Nagib, H. M. (2014). Aspect ratio effects in turbulent duct flows studied through direct numerical simulation. Journal of Turbulence, 15(10), 677–706. https://doi.org/10.1080/14685248.2014.925623

Wang, T.-S., & Chyu, M. K. (1994) Heat convection in a 180-deg turning duct with different turn configurations. Journal of Thermophysics and Heat Transfer, 8(3), 595–601. https://doi.org/10.2514/3.583

Zhang, H., Trias, F. X., Gorobets, A., Tan, Y., & Oliva, A. (2015). Direct numerical simulation of a fully developed turbulent square duct flow up to Re_τ=1200. International Journal of Heat and Fluid Flow, 54, 258–267. https://doi.org/10.1016/j.ijheatfluidflow.2015.06.003

VITA AUCTORIS

NAME: Damanpreet Singh

PLACE OF BIRTH: Ludhiana, Punjab, INDIA

YEAR OF BIRTH: 1994

EDUCATION: Bachelor of Technology
(Mechanical Engineering),
Punjabi University, Patiala, Punjab, INDIA,
2016

Master of Applied Science
(Mechanical Engineering),
University of Windsor, Windsor, ON, CANADA,
2020